POLITECNICO DI TORINO

Master's Degree Course in Aerospace Engineering

Master's Degree Thesis

Navigation and Guidance Algorithms for In-Orbit servicing Rendezvous Mission

Supervisor
Dr. Elisa Capello

Student
Davide Celestini
ID number: 263188

Internship tutor
Tales Alenia SPACE
Dott. Massimiliano Saponara

April 2021

Abstract

The purpose of the thesis is to evaluate and validate Navigation and Guidance algorithms to perform autonomous *In-Orbit Servicing* (IOS) Space missions, a wide range of challenging new solutions for satellite operators. These missions address a large variety of useful applications based on Rendezvous and Proximity Operations (RPOs) technique, such as refuelling, life-extension, inspection, in-orbit assembly and active space debris removal. Particularly, the focus of this work is on position control and path planning during *rendezvous and berthing* operations, in which a Chaser satellite actively follows another satellite, the Target, and then joints with it using a robotic arm.

In order to perform such manoeuvres, these algorithms must be robust and “flyable”, which means that they should be able to effectively operate even with a system slightly different from the one expected and should have a low computational cost. The Navigation algorithms considered are based on the Sliding-Mode Observer (SMO) technique: the ability of observer-based algorithms to reconstruct the system dynamics despite receiving just the measurable states as input and the robustness of the Sliding-Mode technique have been the driving motors for this choice. The thesis also proposes an approach to perform data fusion using multiple position sensors, an optical camera and an accelerometer. Sensor simulation models have been developed in order to recreate realistic inputs for the Navigation algorithm, with different *noise* and *sample rate*.

As for Guidance and Control, different approaches have been chosen depending on the distance of the Chaser from the Target. In the closing phase, two different strategies have been adopted and compared. In the first manoeuvre is designed *a priori* using Hill’s equations and then executed in orbit exploiting a Sliding-Mode Controller (SMC). In the second strategy, the desired path is followed through the combined action of the Artificial Potential Fields (APF) method with moving goal and the Sliding-Mode Control (SMC). The latter strategy has been also adopted for the final approach, even though in this case the APF goal point is fixed and the path is entirely calculated *online*. The classic APF algorithm is able to attract the Chaser towards the Target performing *obstacle avoidance* considering both the Chaser satellite and the fixed obstacles as points. In this thesis the algorithm has been revised to contemplate the possibility of moving obstacles with their own geometrical shapes and take into account physical dimensions of the Chaser satellite. The major problem of APF, the presence of *local minima*, has been faced with the selection of harmonic 3D potential fields, characterised by the presence of global minima and maxima only, both located in the singular points at the end of these functions domain.

Finally, the effectiveness of the selected Navigation and Guidance algorithms has been shown through several simulations conducted in MATLAB&Simulink environment, highlighting how the obstacle avoidance strategy impacts on the rendezvous trajectory and the propellant consumption and showing the performance of the combination of SMO and SMC in maintaining the desired final position during the motion of the robotic arm.

Sommario

Lo scopo del lavoro di tesi è di valutare e validare algoritmi di Guida e Navigazione per missioni spaziali autonome di *In-Orbit Servicing* (IOS), un'ampia gamma di nuove soluzioni per gli operatori e gestori di satelliti. Tali missioni sono pensate per numerose applicazioni che si basano sulla tencica di Rendezvous e Proximity Operations (RPOs), come operazioni di refuel, estensione del ciclo di vita, ispezione, assemblaggio in orbita e rimoziona attiva di detriti spaziali. In particolar modo, l'attenzione di questo lavoro di tesi è posta sul controllo della posizione e la pianificazione di traiettorie durante un'operazione di *rendezvous and berthing* in cui un satellite Chaser insegue attivamente un secondo satellite, chiamato Target, con lo scopo di agganciarlo tramite l'utilizzo di un braccio robotico.

Affinché si possano eseguire le manovre necessarie ad una missione di questo tipo, gli algoritmi di GNC devono essere robusti e "flyable", dunque devono essere in grado di operare in maniera efficace anche con un sistema che presenta lievi differenze rispetto al caso nominale e devono avere un costo computazionale contenuto. Per quanto riguarda la Navigazione, gli algoritmi valutati sono *osservatori* che implementano la tecnica Sliding-Mode (SMO): le ragioni che hanno guidato verso tale scelta sono state la capacità degli algoritmi di osservazione di ricostruire la dinamica di un sistema nonostante una conoscenza limitata ai soli stati misurabili e la robustezza che contraddistingue la tecnica dello Sliding-Mode. La tesi propone anche una metodologia di data fusion per sfruttare le informazioni fornite da camera ottica ed accelerometro, due sensori di posizione installati a bordo del Chaser. Per ognuno di essi è stato realizzato un modello di simulazione che ha permesso di ricreare input realistici per l'algoritmo di Navigazione, ciascuno con il proprio *rumore* e *sample rate*.

Gli approcci adottati per la Guida e Controllo, invece, sono differenti a seconda della distanze del Chaser dal Target. Nella "closing phase", due strategie sono state scelte e poste a confront. Nella prima, la manovra di avvicinamento è stata progettata *a priori* utilizzando le equazioni di Hill ed eseguita in orbita sfruttando un controllore Sliding-Mode (SMC). Nella seconda strategia, la traiettoria desiderata è ricreata con la combinazione del metodo dei Campi Potenziali Artificiali (APF) aventi punto di goal mobile e della tecnica dello Sliding-Mode Control. Questa strategia è stata adottata anche per la fase di "final approach", con la differenza che in essa il punto di goal dell'algoritmo APF è fisso e la pianificazione della traiettoria avviene completamente *online*. L'algoritmo classico APF, che permette di attrarre il Chaser verso il Target evitando eventuali ostacoli ma considera sia il satellite che gli ostacoli fissi come dei punti senza un volume proprio, è stato rivisitato per prevedere la possibilità di ostacoli mobili e con forma propria e considerare anche le dimensioni fisiche del Chaser. Una delle criticità più importanti dell'APF, la

presenza di *minimi locali*, è stata risolta tramite la scelta di campi potenziali armonici 3D, i quali presentano unicamente punti di minimo e masssimo globali localizzati nei punti di singolarità agli estremi del dominio.

Infine, l'efficacia degli algoritmi di Guida e Navigazione selezionati è stata mostrata con l'aiuto di simulazioni effettuate in ambiente MATLAB&Simulink, evidenziando come la strategia di "obstacle avoidance" impatti sulla geometria della traiettoria di approccio e sul consumo di propellente e mostrando come l'azione combinata di SMO e SMC sia in grado di mantenere la posizione desiderata anche durante la movimentazione del braccio robotico.

Contents

List of Tables

List of Figures

Chapter 1

Introduction

This work aims to the identification and demonstration of the effectiveness of robust Guidance, Navigation and Control (GNC) algorithms with low computational cost for In-Orbit Servicing (IOS) missions, a wide range of new solutions for satellite operators based on Rendezvous and Proximity Operations (RPOs) techniques. Initially intended for military purposes, today IOS aims to address a large variety of useful applications, such as refuelling, life-extension, inspection, active debris removal, and represents one of the main challenges for the future of space missions. IOS developments made a big step forward recently with the launch of the Mission Extension Vehicle (MEV-1) which marked a concrete progress in both technological and business areas of servicing operations, offering new interesting prospects for the space sector.

However IOS also raises a variety of issues of different nature: legal and regulatory issues related to the ownership of objects in orbit, security and defence problems concerning the use of IOS solution such as system of destruction and espionage, and last but not least safety issues related to RPOs safe conduct and the use of IOS solutions to achieve space sustainability goals.

The thesis is therefore strongly driven by these new and promising applications and faces their safety challenge proposing robust Sliding-Mode Observers (SMO) as Navigation algorithm, due to their ability to evaluate all the states of a dynamic system even in case of partial knowledge of the system itself. A modified version of the Artificial Potential Field (APF) method combined with a Sliding-Mode Controller (SMC) is chosen as the Guidance algorithm, due to the capability to elaborate *online* a collision-free path to guide the Chaser satellite towards the Target.

1.1 History of In-Orbit Servicing missions

Although servicing of satellites has been theoretically considered since the dawn of spaceflight, little of it was done in the earliest decades. The first servicing provided in the 1990s and the 2000s were actually executed by human astronauts, such as the five Hubble Space Telescope (HST) servicing missions to extend the lifespan of the HST through subsystem-replacement, [1], and the repeated and regular servicing of the International Space Station (ISS) from 1998 to the present day. Nowadays, instead, IOS commercial missions are intended to be autonomous and performed by robotic spacecraft (s/c).

Figure 1.1: HST attached to the Space Shuttle during STS-61, the first Hubble Space Telescope servicing mission, [1].

The first collaboration was initiated in 2012 by the Defense Advances Research Projects Agency (DARPA), with the aim to recycle retired satellite parts into new in-orbit space assets, principally focusing on geosynchronous satellites, [2]. Although system launches were programmed for 2016 and a number of system elements were designed and tested, the US government-funded development program was terminated in 2015.
In 2016, however, the commercial company Intelsat signed a contract with Orbital ATK for the first commercial IOS mission: the MEV-1 (Mission Extender Vehicle) contract, intended to provide for a 5-year life-extension service of Intelsat 901 (I-901), in operation in GEO since 2001, [3]. Developed by SpaceLogistics LLC, a subsidiary of Northrop Grumman since the acquisition of Orbital ATK in 2018, the spacecraft was launched in October 2019 from Baikonur and started the RPO phase in I-901 in February 2020 in a graveyard 300 km above GEO, in order to prevent any possibility of accidents with other GEO satellites. On February 25, MEV-1 completed the RPO phase autonomously approaching, capturing and docking to I-901 and in April 2020 Intelsat announced that, according to the mission plans and in compliance with orbital regulations, MEV-1 successfully relocated I-901 to its new orbit slot. Since the vehicle has been designed to provide life-extension services for up to 15 years, at the end of the current mission MEV-1 could either extend the service or proceed with the disposal of I-901 to a graveyard orbit and become available for new clients. In the meantime, Intelsat already signed a contract for MEV-2 to provide similar servicing to its I-10-02 satcom, in operation since 2004 and SpaceLogistics LLc is reported to be developing the MEV-2 spacecraft with additional capacity to carry payloads and deploy small satellites.

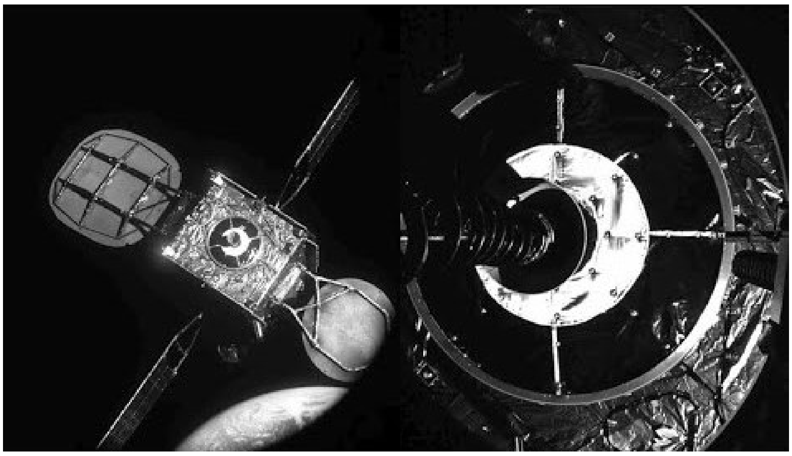

Figure 1.2: Intelsat I-901 seen from MEV-1 on the left, the docking mechanism in action on the right, [3].

In the United States, institutional actors, in particular NASA, DARPA and the Department of Defense, played a decisive role in promoting the development of IOS capabilities. DARPA itself initiated another collaboration in 2017 between researchers and U.S. government, with the aim to develop rules for future commercial use of in-orbit satellite repair, since satellite servicing protocols have not been developed yet.

As for Europe, European companies have been actively preparing for the emergence of IOS and ESA decided to identify the Active Debris Removal (ADR) as a strategic goal. The first space debris removal service will be the ClearSpace-1 mission, [4], which will capture and deorbit the 100 kg VEga Secondary Payload Adapter (VESPA) upper stage, in LEO since 2013 (ConOps in Fig. 1.3). The launch is programmed to be in 2025.

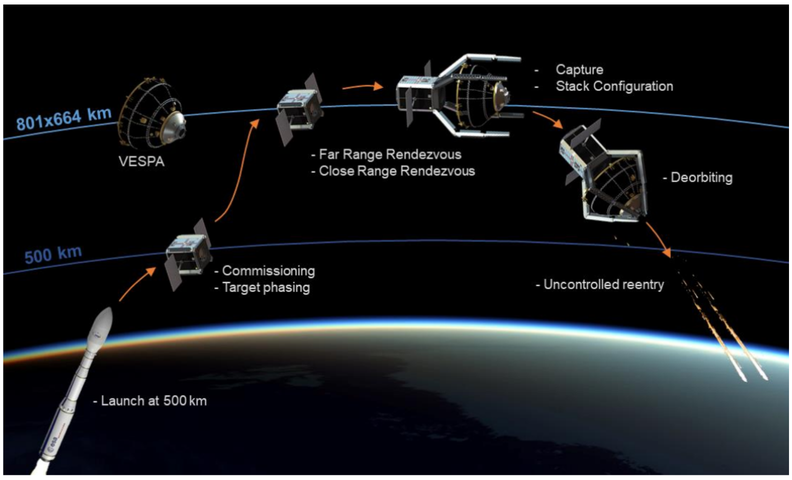

Figure 1.3: ClearSpace-1 mission Concept of Operations, [4].

1.2 Space debris and space sustainability

The term “space debris” refers to human-made objects in space which no longer serve a useful function. These include non-functional spacecraft and abandoned launch vehicle stages, mission-related debris, fragmentation debris originated from spacecraft explosions or collisions and fragments derived by the satellites erosion and disintegration, like paint flecks and solidified liquids expelled from spacecraft.

These objects began to accumulate in Earth orbit since the dawn of space exploration, in the late 1950s, and gradually increased in the decades. The increase of space activities characterising the last decade, however, caused a sudden rise of this phenomenon and in October 2019 more than 20 000 artificial objects were reported in orbit around the Earth by the US Space Surveillance Network , just 2218 of them being operational satellites. Furthermore, these numbers refer only to objects large enough to be tracked. At the beginning of 2021, the estimated number of space debris by dimension is much greater [5]:

- 128 million objects from greater than 1 mm to 1 cm;
- 90 0000 objects from greater than 1 cm to 10 cm;
- 34 000 objects greater than 10 cm.

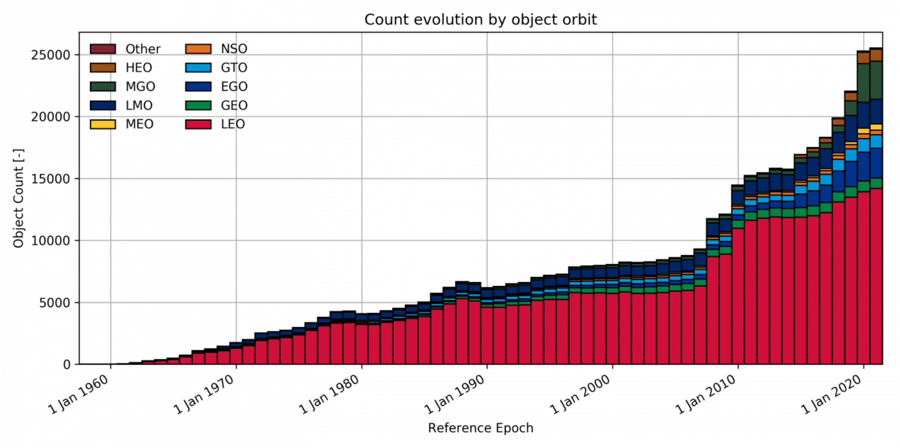

Figure 1.4: Space debris count evolution by object orbit, [5].

As it can be seen from Fig. 1.4, these debris are mostly concentrated in Low-Earth Orbits (LEO), which are the most common ones, and the amount of space debris steadily increased during the past decades, with the exception of two sudden rises in the late 2000s. These rises were the results of the Chinese Anti-Satellite (ASAT) test in 2007, in which a 865 km-height satellite was intentionally destroyed, and the unintentional collision occurred in 2009 between the 950 kg derelict satellite Kosmos 2251 and the 560 kg operational Iridium 33, once again in the higher portion of the LEO band. These 800-1000 km height orbits still remain the ones characterised by the greatest debris density, also due to the fact that the extremely low density of the atmosphere characterising these heights makes the objects decay caused by aerodynamic drag an extremely slow process. Another particular orbit which is characterised by a high concentration of space debris is the Geostationary Orbit (GEO) shared by many communication satellites. The natural decay process for this orbit could require millennia, therefore satellites are usually moved away from thier orbital slots and relocated into graveyard orbits at the end of their lifespan. Despite these efforts, collisions have occurred even in these bands of orbits, such as the Russian Express-AM11 communications satellite which was struck by an unknown object in 2007.

Space debris represent a major hazard especially for the upcoming projects of "mega-constellations" of internet satellites, which of course could be involved in collisions and generate even more debris. In a 'business-as-usual' scenario the number of debris objects in space and the probability of catastrophic collisions will grow simultaneously: each collision will generate more debris objects and increase the collision probability itself in a cascade effect which will cause collision to prevail over the now-dominating explosions within few decades. Eventually collisions fragments will start colliding with other collision fragments, causing an autonomous rise of space debris. This self-sustained process, known as "Kessler syndrome", is particularly critical for LEO band and must be avoided in order not to lose the capability to safely send satellites in orbit.

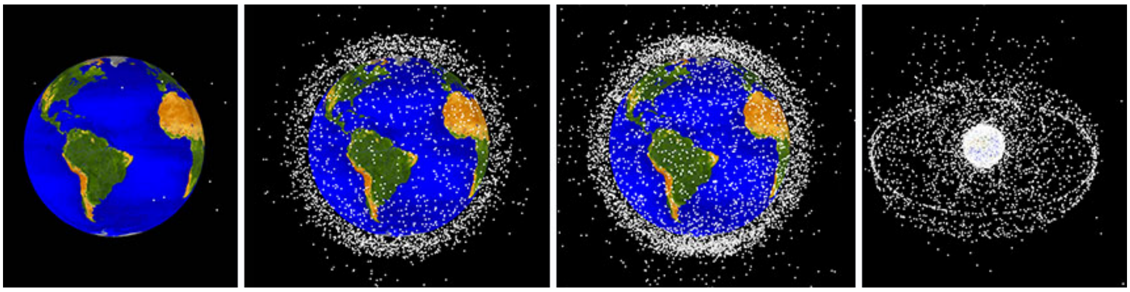

Figure 1.5: Representation of the Kessler syndrome evolution, [6].

As explained at the end of Sec. 1.1, ADR is one of the main tools to decrease the density of space debris, particularly in the critical high-LEO band. However, removal missions are not the only tools that can be used: mitigation techniques represent a fundamental mean to reduce the formation of debris object itself. Each space mission nowadays implements these mitigation techniques to elaborate safe disposal plans according to international regulations, but prevention methods must be adopted in each phase of the mission itself. An autonomous In-Orbit Servicing mission, therefore, must perform safely rendezvous and proximity operations (RPOs), not only considering safety corridors, passively safe manoeuvres and Collision Avoidance Manoeuvres (CAM) during the design of the Chaser path toward the Target, but also adopting "obstacle avoidance" techniques to take into account the possibility of encountering other obstacles, such as other satellites or space debris objects, during the approach. Algorithms able to perform obstacle avoidance are therefore mandatory to achieve the full automation of IOS mission in compliance with current regulations and sustainability goals.

1.3 Rendezvous & berthing operations

A space rendezvous is a set of orbital manoeuvres in which two vehicles arrive at the same orbit and approach to a short distance. Usually, the *Chaser* satellite is the one actively manoeuvring and moving towards a passive *Target*, which instead is the one "waiting" to be reached. The Target could be both collaborative, such as another functioning spacecraft, or not collaborative, for example a non-functioning spacecraft or a object like space debris.

This process may be followed by a physical joint of the two spacecraft, operation called *docking* when the spacecraft joining together are free-flying, or *berthing* in case a passive module is dragged into the mating interface with the aid of a robotic arm. While docking tends to be preferred for manned missions due to its capability of performing rapid operations, critical requirement for an emergency evacuation from International Space Station (ISS) for example, berthing is more suitable for IOS missions, in particular when the spacecraft receiving the service is not collaborative (even though in case of not collaborative Target the term *capture* should be used instead of berthing).

The first successful rendezvous was accomplished by US during the Gemini campaign: after a series of failed attempts, in 1965 Gemini 6 was manually manoeuvred within 30 cm of Gemini 7 and the position was hold for 20 minutes. The year after, US performed also the first manual docking when Gemini 8, under the command of Neil Armstrong, rendezvoused and docked with the uncrewed Agena Target Vehicle, [7]. The Soviets, instead, performed the first automatic uncrewed rendezvous and docking between Cosmos 186 and Cosmos 188 in 1967, while in 1969 achieved their first manned docking with Soyuz 4 and 5 docking and exchanging two crew members.

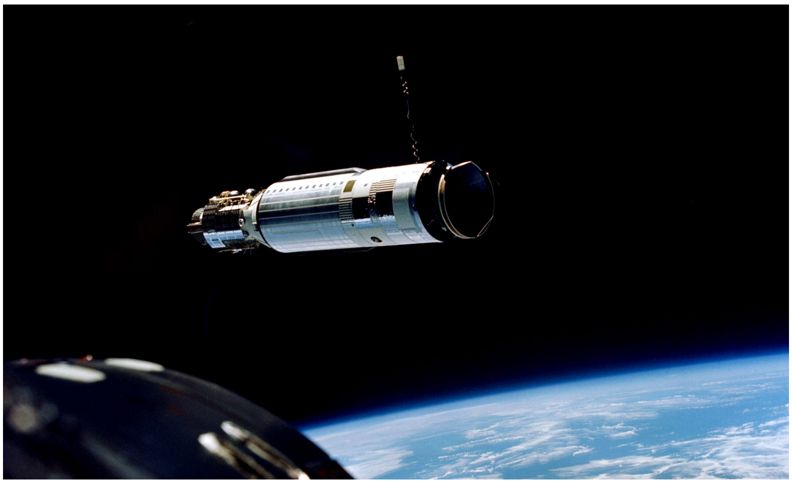

Figure 1.6: Agena Target Vehicle in orbit view from Gemini 8, [7].

Due to the vicinity of the objects involved, these operations must be performed in compliance with strict regulations and requirements establishing boundaries on relative position and velocity, on the accuracy of sensors and algorithms and even on the geometrical shape of the approaching trajectory itself. For the sake of simplicity, the whole process is commonly divided into different phases, each of them having its own design method, reference frame and requirements [8, 9]:

- **Launch and orbit injection**: the aim of the launch is to put the Chaser on a lower orbit in the same orbital plane of the Target. Consequently, the launch site and window should be chosen accordingly.

- **Phasing**: the objective is to correct eventual inclination or RAAN errors, reduce the phase angle between the Chaser and the Target (Fig. 1.7) and bring the Chaser to an orbit and a position near the Target so that the relative navigation can begin. During this phase the Chaser is still controlled by ground stations.

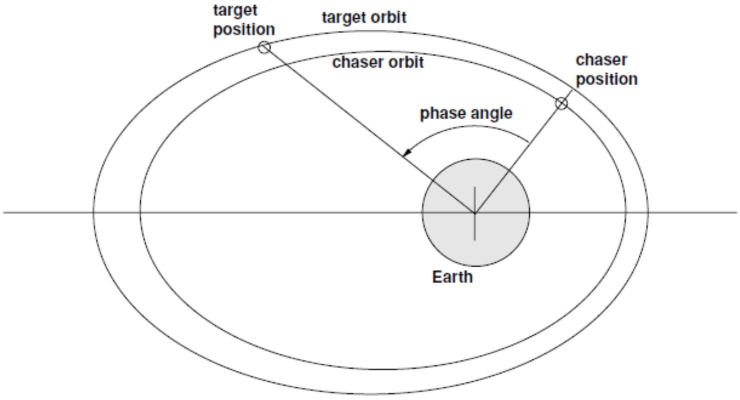

Figure 1.7: Definition of phase angle, [9].

- **Far range rendezvous manoeuvres**: the purpose of this phase, also called *homing*, is to reduce the relative velocity of the Chaser bringing it in the proximity of the Target orbit. From this point forward the navigation is based on relative measures and the control could be automated.

- **Close range rendezvous manoeuvres**: this phase could be furtherly divided into *closing*, having the aim of acquiring the position, velocity and attitude requirements to begin the final approach to the Target, and *final approach* itself, in which the Chaser follows a predefined path towards the Target to acquire the state required for mating operations.

- **Mating**: obviously, the last phase has the purpose of joining the Chaser with the Target. Strict requirements concerning residual linear and angular velocity and position and angular alignment must be observed, even during the movimentation of the robotic arm in case of berthing.

Several strategies could be elaborated and adopted but a typical mission in reported in Fig. 1.8.

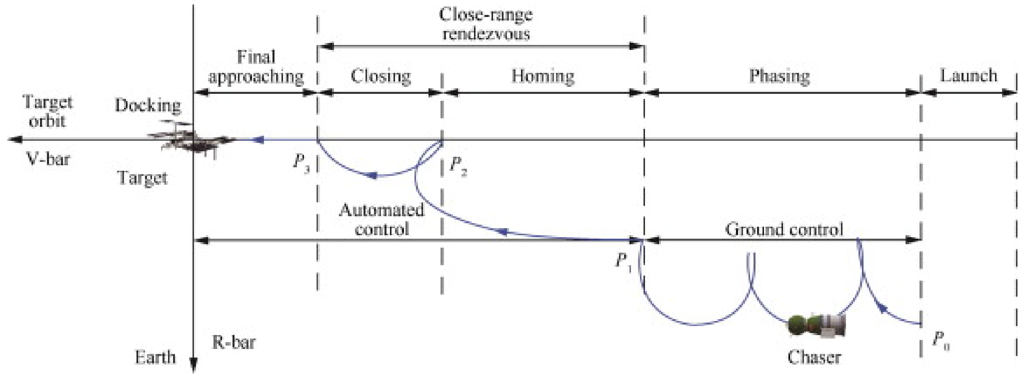

Figure 1.8: Schematic representation of a Rendezvous and Docking/Berthing mission, [10].

1.4 Navigation and Guidance algorithms in literature

The choice of the algorithm composing the GNC system of the Chaser s/c is fundamental for the success of Rendezvous and Proximity Operations, and several examples of Navigation and Guidance algorithms can be found in literature, both in aerospace and non-aerospace applications.

As for Navigation, uncertainties, disturbances or measurement signals corrupted by noise have often been faced exploiting *Kalman filters*. These filters are very effective and computationally efficient, but their robustness is determined by the knowledge of statistics parameters characterising the sensors noise, which is assumed to have a Gaussian distribution. For this reason, in the latest years, new Navigation techniques have been investigated and proposed. *Observers* represent a promising alternative to the problem of perturbed system observation, due to their capability to withstand noisy measurement signals without requiring any statistics knowledge. Particularly, the use of the Sliding-Mode technique in observation approach seems to greatly increase the algorithm robustness. Several applications and comparisons can be found in literature, [11, 12, 13] and the results obtained are characterised by robustness, stability and convergence in finite time. In [13], in particular, the SMO is further combined with Proportional Navigation (PN) in the homing missile guidance system. The performance achieved show robustness against noise and are comparable to the Kalman filter, demonstrating the effectiveness of SMO algorithms even in closed loop GNC systems.
In order to take into account safety factors and obstacle avoidance, however, *Artificial Potential Field* methods are usually preferred for Guidance purposes. Many other works in robotics and aerospace fields, [14, 15, 16], showed the effectiveness of the algorithm, which is able to execute *online* computation of collision-free paths in both 2D and 3D environments. The APF method is also characterised by an high level of design flexibility, allowing the user to overcome typical problems, such as the presence of *local minima*, modifying the classical form of the algorithm and choose the Control algorithm which best suits the application. In [14, 15], for example, APF law is paired with different Sliding-Mode Control techniques, achieving high level of robustness and accuracy.

1.5 Overview of the thesis work

The present work focuses on the choice and the design of Navigation and Guidance algorithms for the management of relative position during the final phases of a rendezvous and berthing operation during an IOS mission, beginning with the closing phase and ending with the movimentation of the robotic arm attached to the Chaser service module. Due to the vicinity of the two satellites the whole analysis is implemented using Clohessy-Wiltshire or Hill's equations and relative measurements provided by onboard sensors, which are modelled in order to create realistic inputs for the Navigation algorithm. GNC algorithms suitable for the execution of an automated In-Orbit Servicing mission are designed and evaluated considering different factors such as their accuracy, their computational cost and their robustness to unknown inputs and parametric uncertainties. Furthermore, the work proposes some modification to standard GNC algorithms to perform data fusion and avoid local minima problems performing obstacle avoidance.

The remaining part of the present document is organised in six chapters.

- Chapter 2 discusses the reference frame used for the analysis and the orbital dynamics characterising the problem, emphasizing the guidelines for the choice of both the general approach and the particular manoeuvres of a rendezvous closing phase.
- Chapter 3 illustrates different Navigation algorithms and compare them through literature and simulation results, explaining why Sliding-Mode observer-based algorithms (SMO) have been chosen for this project. Different SMOs are presented, each with an overview of its inputs, outputs, strengths and weaknesses.
- In chapter 4 a deep discussion relative to the Artificial Potential Field (APF) Guidance algorithm is presented, proposing methods to avoid common problems correlated to the conventional form of the algorithms and explaining the reasons behind the choice of the Sliding-Mode Control algorithm (SMC) to be paired with APF. The chapter proposes adaptations of the algorithm to take into account moving obstacles and targets, too.
- Chapter 5 provides a presentation of the Chaser spacecraft configuration, first of all describing its geometrical shape. Afterwards, the onboard thrusters configuration and position sensors set are discussed, as well as the simulation models used to implement these sensors and actuators.
- Lastly, in chapter 6, all the solutions presented in the previous chapters are applied to this particular mission starting with the choice of the approach strategy for rendezvous, explaining how data fusion has been paired with the SMO selected as Navigation algorithm and ending with the choice of Guidance and Control algorithms for both the closing phase and the final approach. Different scenarios simulated in MATLAB&Simulink environment with different configurations of obstacles are considered in order to show the effects of the obstacle avoidance strategy both on the trajectory geometry and on the propellant consumption. Chaser capability to perform station-keeping during the robotic arm movimentation at the end of the final approach is used as a validation tool to demonstrate SMO&SMC pairing effectiveness in berthing operations.

Chapter 2

Reference frames and orbital dynamics

As previously discussed in Section 1.3, different phases of *rendezvous and docking/berthing* (RVD/B) operations are usually dealt with using different reference frames and types of navigation. The present chapter, therefore, aims to provide a deep explanation about orbital relative motion dynamics, starting with an overview of the general coordinate frames used for each RVD/B phase and then focusing just on closing and final approach, the ones studied in this thesis work. The chapter ends with an illustration of safety considerations that must be taken into account in the RVD/B manoeuvre design.

2.1 Reference frames overview

The coordinate frames used for the description of orbital motion could be both *absolute* reference frames, used for absolute motion, or *relative* reference frames, more suitable for the analysis of relative trajectories. Each frame F_i is defined by its origin O_i and a set of three orthogonal vectors a_1, a_2, a_3 representing the frame axes. Three main types of coordinate frames are required in the design of a RVD/B operation:

- **Orbit reference frames** to describe the orientation of the satellite orbit relative to inertial space, e.g. relative to the centre of the Earth.

- **Spacecraft local orbital reference frames** to describe the motion relative to a particular point in orbit, which could be both a “virtual” point or another satellite.

- **Spacecraft attitude and geometric frames** to describe dynamic and kinematic processes of the spacecraft relative to its own centre of mass, such as attitude manoeuvres, identify meaningful points of the spacecraft, for example the location of a particular sensor, or analyse the relative motion w.r.t. a particular point of the satellite, such as the docking or berthing port.

2.1.1 Earth-centred equatorial frame F_{eq}

The F_{eq} coordinates are normally used to describe a satellite absolute motion around the centre of mass (CoM) of the Earth w.r.t. inertially fixed directions and is characterised by:

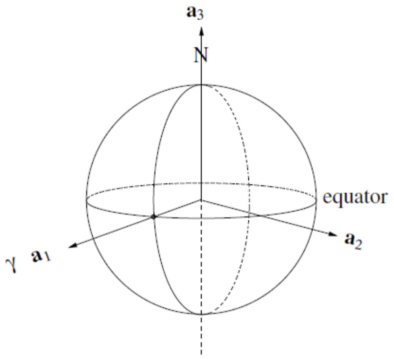

Figure 2.1: The F_{eq} reference frame, [9].

- origin O_{eq} located in the CoM of the Earth, which is assumed to be truly spherical.
- axis x_{eq} laying in the equatorial plane and pointing towards the vernal equinox direction.
- axis z_{eq} normal to the equatorial plane and pointing north.
- axis y_{eq} such to complete the right-handed tern.

2.1.2 Orbital plane frame F_{op}

Another frame used for absolute navigation purposes is F_{op} which is more likely to be exploited in case only the motion of the satellite within its orbit should be of interest, for example in the analysis of orbital manoeuvres. It is identified by:

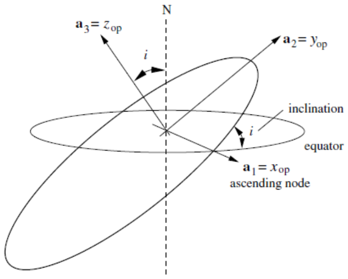

Figure 2.2: The F_{op} reference frame, [9].

- origin O_{op} located in the centre of the Earth, which is assumed to be truly spherical.

- axis x_{op} laying in the orbital plane and pointing toward the ascending node.
- axis z_{op} normal to the orbital plane and inclined to the north by an angle i.
- axis y_{op} such to complete the right-handed tern.

The rotation matrix allowing the transformation from the Earth-centred equatorial frame to the orbital plane frame is obtained by a first rotation about z_{eq} by the value of the RAAN angle Ω followed by a second one about the new x axis, corresponding to the node line x_{op}, by the inclination angle i.

$$\begin{bmatrix} x_{op} \\ y_{op} \\ z_{op} \end{bmatrix} = \overbrace{\begin{bmatrix} 1 & 0 & 0 \\ 0 & \cos i & \sin i \\ 0 & -\sin i & \cos i \end{bmatrix}}^{[L_1(i)]^{-1}} \overbrace{\begin{bmatrix} \cos\Omega & \sin\Omega & 0 \\ -\sin\Omega & \cos\Omega & 0 \\ 0 & 0 & 1 \end{bmatrix}}^{[L_3(\Omega)]^{-1}} \begin{bmatrix} x_{eq} \\ y_{eq} \\ z_{eq} \end{bmatrix} \tag{2.1}$$

2.1.3 Spacecraft local orbital frame F_{lo}

The F_{lo} frame, often referred as the local-vertical/local-horizontal frame (LVLH), is the main one used for the description of relative motions w.r.t. the moving position and direction towards the centre of the Earth. This frame can be defined both for the Chaser and the Target satellite, but in rendezvous manoeuvres the Target satellite LVLH frame is usually used to describe the relative motion of the Chaser w.r.t. the Target itself. In general, F_{lo} is defined as follows:

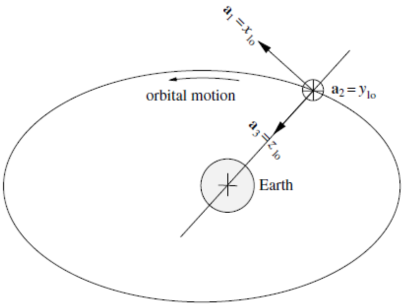

Figure 2.3: The F_{lo} reference frame, [9].

- origin O_{lo} located in the satellite centre of mass.
- axis z_{lo}, called also R_{bar}, pointing towards the centre of Earth.
- axis y_{lo}, called also H_{bar}, normal to the orbital plane and directed towards the opposite direction of the orbit angular momentum vector.
- axis x_{lo}, called also V_{bar}, such to complete the right-handed tern (in case of circular orbits the V_{bar} axis is aligned with the orbit trajectory and the velocity vector itself).

The coordinate transformation from the orbital plane frame to the spacecraft local orbital frame is a function of time, since is obtained by a rotation around the z_{op} by the orbital phase angle $\Phi = \omega_{\odot} t$ (with $\omega_{\odot}$ being the orbital angular rate) and two 90deg-rotations, the first one around the positive direction of z_{op} and the second one around the negative direction of the new x axis corresponding to x_{lo}.

$$\begin{bmatrix} x_{lo} \\ y_{lo} \\ z_{lo} \end{bmatrix} = \overbrace{\begin{bmatrix} 1 & 0 & 0 \\ 0 & 0 & -1 \\ 0 & 1 & 0 \end{bmatrix}}^{\left[L_1(-\frac{pi}{2})\right]^{-1}} \overbrace{\begin{bmatrix} 0 & 1 & 0 \\ -1 & 0 & 0 \\ 0 & 0 & 1 \end{bmatrix}}^{\left[L_3(\frac{pi}{2})\right]^{-1}} \overbrace{\begin{bmatrix} \cos\Phi & \sin\Phi & 0 \\ -\sin\Phi & \cos\Phi & 0 \\ 0 & 0 & 1 \end{bmatrix}}^{[L_3(\Phi)]^{-1}} \begin{bmatrix} x_{op} \\ y_{op} \\ z_{op} \end{bmatrix} \tag{2.2}$$

2.1.4 Spacecraft attitude and geometric frames

The spacecraft attitude frame F_a, often referred to as *body frame*, is generally used to describe rotations of the spacecraft body w.r.t. the LVLH frame. As the LVLH system it is centred on the spacecraft CoM, while the direction of its axes is either linked to geometrical features of the satellite itself or aligned with directions of interest characterising the phase of the manoeuvre. The coordinate transformation allowing to transform a vector from the LVLH frame to the attitude frame is obtained rotating the former one by the attitude angles ψ (yaw), θ (pitch) and ϕ (roll).

$$\begin{bmatrix} x_a \\ y_a \\ z_a \end{bmatrix} = \overbrace{\begin{bmatrix} 1 & 0 & 0 \\ 0 & \cos\phi & \sin\phi \\ 0 & -\sin\phi & \cos\phi \end{bmatrix}}^{[L_1(\phi)]^{-1}} \overbrace{\begin{bmatrix} -\sin\theta & 0 & \cos\theta \\ 0 & 1 & 0 \\ \cos\theta & 0 & \sin\theta \end{bmatrix}}^{[L_2(\theta)]^{-1}} \overbrace{\begin{bmatrix} \cos\psi & \sin\psi & 0 \\ -\sin\psi & \cos\psi & 0 \\ 0 & 0 & 1 \end{bmatrix}}^{[L_3(\psi)]^{-1}} \begin{bmatrix} x_{lo} \\ y_{lo} \\ z_{lo} \end{bmatrix} \tag{2.3}$$

Spacecraft geometric frames F_{ge}, instead, are usually exploited to describe relative motions w.r.t. particular points or directions characterising the satellite itself, e.g. sensors or docking/berthing mechanisms. Fig. 2.4 compares the two systems:

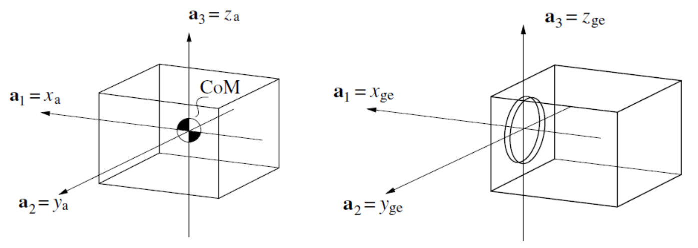

Figure 2.4: F_a reference frames on the left, F_{ge} on the right, [9].

As it can be seen, the origin O_{ge} is located in the satellite point of interest, while the axes could be either aligned with or under a fixed angle to the ones of the attitude frame. Lastly, it must be pointed out that the coordinate transformation between F_a and F_{ge} has to take into account not only a triple rotation, but also the translation between the spacecraft CoM and the point of interest.

2.1.5 Reference frames used in RVD/B phases

During rendezvous and docking/berthing missions, the common procedure, [8], is to use absolute frames and navigation until the end of the phasing phase: prior to this point, Chaser and Target are far from each other and their motion is studied as the orbital motion of a satellite around a central body, i.e. the Earth. As an example, F_{eq} is generally preferred to study and decide launch sites and windows, while the use of F_{op} is more effective when the Chaser satellite has already reached the orbit, which means it is likely to be used for the orbital manoeuvres executed during the phasing.

With the beginning of the homing phase, instead, Chaser and Target get closer and the main interested is shifted to relative motions and navigation. In particular, the frame used for homing, closing and final approach phases is the Target LVLH frame: in this way, the Target position is always known and fixed in O_{LVLH}, while the position of the Chaser is expressed exactly as the relative position w.r.t. the Target CoM. Lastly, during the mating, Target geometric frames could be used as an alternative to the LVLH one in case it is desired to describe relative motions directly w.r.t. the docking/berthing mechanisms. Tab. 2.1 summarises the discuss of the present section.

Table 2.1: List of reference frames usually adopted during RVD/B manoeuvres.

Phase	**Navigation type**	**Reference frame**
Launch and orbit injection	Absolute	F_{eq}/F_{op}
Phasing	Absolute	F_{op}
Far range manoeuvres	Relative	Target F_{LVLH}
Close range manoeuvres	Relative	Target F_{LVLH}
Final approach	Relative	Target F_{LVLH}
Mating	Relative	Target F_{LVLH}/F_{ge}

2.2 Relative motion dynamics - Hill's equations

As previously discussed, from the homing phase on, rendezvous operations are analysed using the Target LVLH frame and the motion of the Chaser s/c is described w.r.t. the Target CoM. Under the assumption of circular orbit with constant orbital angular rate, the relative motion dynamics can be described by Hill's equations, often referred to also as Clohessy-Wiltshire equations:

$$\begin{aligned} \ddot{x} - 2\omega_{\odot}\dot{z} &= \frac{1}{m_c}F_x \\ \ddot{y} + 2\omega_{\odot}^2 y &= \frac{1}{m_c}F_y \\ \ddot{z} - 3\omega_{\odot}^2 z + 2\omega_{\odot}\dot{x} &= \frac{1}{m_c}F_z \end{aligned} \tag{2.4}$$

Where:

- x, y, z represent the Chaser relative position w.r.t. the Target respectively along $V_{bar}, H_{bar}, R_{bar}$.
- $\omega_{\odot} = \frac{2\pi}{T_t}$ is the constant angular rate characterising the circular orbit of the Target.
- m_c is the Chaser s/c mass which could also be time-varying, e.g. following the rocket equation $\dot{m}_c = \frac{F_{thr}}{g\ I_{sp}}$ with F_{thr} being the thrust modulus, g the gravitational acceleration of Earth and I_{sp} the specific impulse of the selected thrusters.
- F_x, F_y, F_z represent the forces acting on the Chaser respectively along $V_{bar}, H_{bar}, R_{bar}$, so expressed in the Target LVLH frame - no forces are considered to be acting on the Target.

It must be highlighted that F_x, F_y, F_z are the components of the forces vector $\mathbf{F}$ which is the sum of both thruster forces $\mathbf{F}_{thr}$ and environmental forces $\mathbf{F}_{ex}$, e.g. residual atmospheric drag, solar pressure, gravitational forces due to the Earth non-perfect sphericity and magnetic forces. If these forces are not directly obtainable in the LVLH frame, they must be multiplied by the appropriate rotation matrix to be transformed into the right reference system before their use inside Hill's equations. For example, $\mathbf{F}_{thr}$ is usually known in the Chaser body or attitude frame and it must be transformed as it follows:

$$\mathbf{F}_{thr}^{(LVLH)} = L_{LVLH\_a}\ \mathbf{F}_{thr}^{(a)} \tag{2.5}$$

where L_{LVLH_a} is obtainable as the inverse of the matrix presented in Eq. 2.3 and transforms a vector from the attitude to the LVLH frame.

The Eq. 2.4 represent a system of linear differential equations the solution of which can be easily calculated computationally, while obtaining analytical solutions results not to be trivial. In 1960, Clohessy and Wiltshire obtained an analytical linear solution considering constant forces acting on the Chaser and distances between Chaser and Target much smaller than the distance of Target from the Earth. The formulation is reported in the Eq. 2.6 and usually used for the study of impulsive/continuous thrust rendezvous manoeuvres.

$$\begin{aligned}
x(t) &= \left(\frac{4\dot{x}_0}{\omega_{\odot}} - 6z_0\right)\sin(\omega_{\odot}t) - \frac{2\dot{z}_0}{\omega_{\odot}}\cos(\omega_{\odot}t) + (6\omega_{\odot}z_0 - 3\dot{x}_0)\,t + \left(x_0 + \frac{2\dot{z}_0}{\omega_{\odot}}\right) + \\
&\quad + \frac{2F_z}{\omega_{\odot}^2 m_c}(\omega_{\odot}t - \sin(\omega_{\odot}t)) + \frac{F_x}{m_c}\left(\frac{4}{\omega_{\odot}^2}(1 - \cos(\omega_{\odot}t)) - \frac{3}{2}t^2\right) \\
y(t) &= y_0\cos(\omega_{\odot}t) + \frac{\dot{y}_0}{\omega_{\odot}}\sin(\omega_{\odot}t) + \frac{F_y}{m_c}(1 - \cos(\omega_{\odot}t)) \\
z(t) &= \left(\frac{2\dot{x}_0}{\omega_{\odot}} - 3z_0\right)\cos(\omega_{\odot}t) + \frac{\dot{z}_0}{\omega_{\odot}}\sin(\omega_{\odot}t) + \left(4z_0 - \frac{2\dot{x}_0}{\omega_{\odot}}\right) + \\
&\quad + \frac{2F_x}{\omega_{\odot}^2 m_c}(\sin(\omega_{\odot}t) - \omega_{\odot}t) + \frac{F_z}{m_c}(1 - \cos(\omega_{\odot}t))
\end{aligned} \tag{2.6}$$

The linearisation allowing to obtain these readable equations, however, causes the accuracy of Clohessy Wiltshire equations to decrease with the distance from the origin, the Target CoM: due to the curvature of the orbit the error in the z-direction rapidly increases when the distance between Chaser and Target is larger than tens of kilometres, changing for few metres at 10 km to several tens of metres at 30 km. A curved definition of the x-coordinate could eventually increase the application range of these equations, but this discussion would be outside the scope of this thesis work, which focuses on the closing and final approach phases.

2.3 RVB global approach strategy

The global strategy for a rendezvous and berthing operation strongly depends on the strategy that has to be adopted for the final approach which, in turn, depends mainly on the location of the Target berthing mechanism, the capabilities of the robotic arm and safety factors.
As it can be seen from both the formulations reported in Eq. 2.4 and 2.6, Hill's equations are characterised by a coupled motion in V_{bar} and R_{bar} and an independent motion along H_{bar}. This feature results in a eventual sinusoidal de-coupled motion along the H_{bar} direction in presence of any y_0, $\dot{y}$ or $F_y \neq 0$. For this reason, approach in the H_{bar} direction must be immediately excluded since the Chaser motion will always tend dangerously towards the Target.

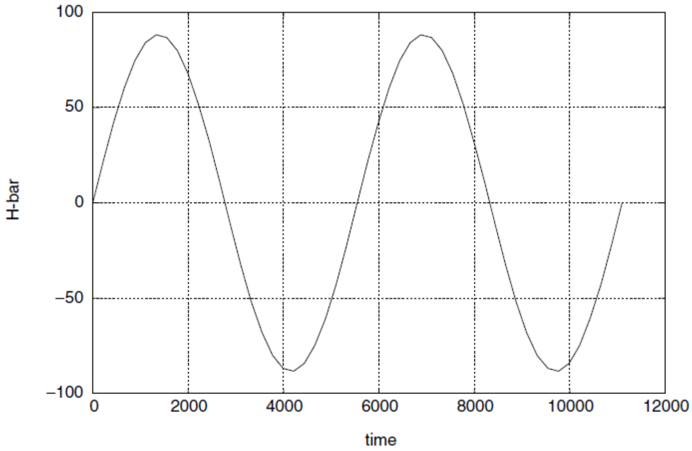

Figure 2.5: Example of sinusoidal motion along H_{bar} during two orbital periods caused by an initial impulse in the $+y$-direction, [9].

Possible paths to reach the Target are consequently approaches in the $\pm V_{bar}$ and $\pm R_{bar}$ direction and the choice will greatly influence the execution of the previous *closing phase* since the aiming point of this phase will lay on $\pm V_{bar}$ or $\pm R_{bar}$ accordingly. In case of docking, this choice would be strictly dictated by the location of the docking port and docking axis. In case of berthing operations, instead, the strategy selection is less dependent on the location or the axis of the berthing port. Depending on the reach and articulation capabilities of the robotic arm, in fact, a convenient "berthing box" can be selected, taking into further account only the geometry shape of the satellites and the location of the grapple fixture, the part of the captured satellite which will be grabbed by the robotic arm. Flexibility in the choice of approaching paths is indeed the major advantage of berthing, allowing to adopt V_{bar} approaches which are usually preferable to R_{bar} ones since a hold point on V_{bar} is often required for safety or operational reasons. It must be highlighted also that performing hold points on V_{bar} is much less propellant-consuming than performing station-keeping on R_{bar} because relative orbital dynamics naturally allow to remain on a fixed position along V_{bar} with zero relative velocity without the application of any force.

In the following sections, however, closing phase manoeuvres suitable for both types of approach as well as straight line final approaches along both V_{bar} and R_{bar} will be presented for the sake of generality. No homing phase manoeuvres will be discussed since the present work only focuses on the rendezvous last few hundreds of metres.

2.4 Closing phase

Since the aim of the homing phase is to bring the Chaser near the Target and acquire its orbit, we will consider the starting point of the closing phase as laying on the V_{bar} axis. Objective of the closing phase, instead, is the reduction of the range between Chaser and Target and the acquisition of proper position and velocity to begin the final approach. If the approach axis for mating is not in the $\pm V_{bar}$ direction, the closing phase may include a fly-around manoeuvre to acquire the approach axis, otherwise the phase end point will lay again on the V_{bar} axis. This kind of task can be executed with two different types of manoeuvres, the features of which are discussed below.

- **Impulsive manoeuvres**: trajectories evolving from a set of initial conditions plus an instant change of velocity that represents a boost manoeuvre.
- **Continuous thrust manoeuvres**: trajectories evolving from a set of initial conditions plus the continuous application of a constant force (calculated in open-loop) along the trajectory.

Impulsive manoeuvres are usually less propellant-consuming and requires less time to reach the endpoint, so they should be preferred when possible. However, instant velocity changes are not obtainable in reality due to the limited level of thrust so impulsive manoeuvres will inevitably be *quasi-impulsive* in real applications, the accuracy of which will lowers with the firing time increase. If the firing time required to acquire the desired velocity is much smaller than the orbital period the manoeuvre can be considered as quasi-impulsive with good approximation, otherwise the selection of continuous thrust manoeuvres will be mandatory. The firing time necessary to execute the velocity change required ΔV can be calculated as showed in Eq. 2.7.

$$\Delta t_{on} = \frac{\Delta V \ m_c}{F_{thr}} \tag{2.7}$$

where F_{thr} is the available thrust level. This formula represents a good approximation if the mass of the Chaser is quasi-constant during the boost itself, the variation of which is calculated in Eq. 2.8:

$$\Delta m_c = \dot{m}_c \ \Delta t_{on} = \frac{F_{thr}}{g \ I_{sp}} \frac{\Delta V \ m_c}{F_{thr}} = \frac{\Delta V \ m_c}{g \ I_{sp}} \tag{2.8}$$

Consequently, for a selected manoeuvre with a certain ΔV requirement, the values of Δt_{on}, Δm_c and the choice between quasi-impulsive and continuous thrust manoeuvres are dictated by the thrust level F_{thr} and the specific impulse I_{sp} characterising the onboard thrusters. These features are linked to the nature of the thruster itself:

- *thermochemical thrusters*, usually characterised by high levels of thrust, allow to have low Δt_{on} and are suitable for quasi-impulsive manoeuvre, even though the propellant consumption could rapidly increase with the ΔV effort due to their low specific impulses.
- *electric/electromagnetic thrusters*, despite having low propellant consumption thanks to their high specific impulses, are characterised by extremely low thrust levels and therefore demand continuous thrust manoeuvres.

In the following sections, only manoeuvres characterised by forces in the $V_{bar} - R_{bar}$ plane (in plane manoeuvres) will be discussed since, as previously discussed, the effect of out of plane impulses will always be a sinusoidal motion around the orbital plane with a period corresponding to the orbital one.

2.4.1 Tangential thrust manoeuvres

During the closing phase, thrust manoeuvres with a ΔV in a $\pm x$-direction are used for transfers along the Target orbit and fly-arounds, e.g. from V-bar to a point where an R-bar approach can commence. The effect of a ΔV impulse in the positive x direction over a single orbital period can be seen in Fig. 2.6, where the initial conditions are:

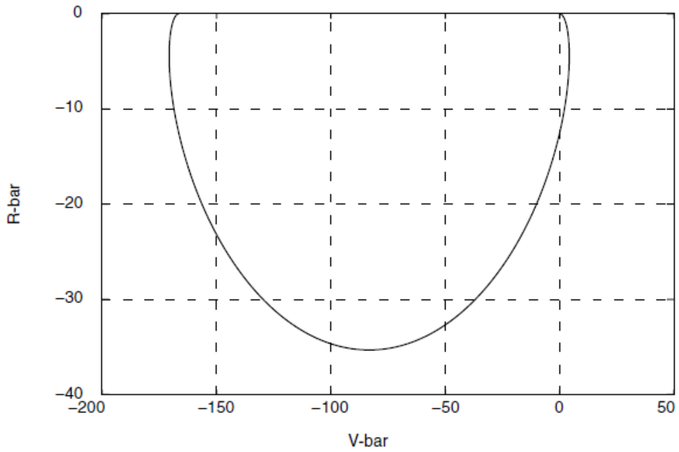

Figure 2.6: Example of relative motion over a period after a $\Delta V_x = 0.01\ m/s$, [9].

$$\begin{cases} x_0,\ y_0,\ z_0 = 0 \\ \dot{x}_0 = \Delta V_x = 0.01\ m/s \\ \dot{y}_0,\ \dot{z}_0 = 0 \end{cases}$$

The resulting trajectory is the sum of a looping motion and a drift motion towards to direction opposite to the initial impulse which causes a remarkable change in the Chaser relative position w.r.t. the Target. Analytically, it is described by Eq. 2.9.

$$\begin{aligned} x(t) &= \frac{1}{\omega_\odot}\Delta V_x \left(4\sin\left(\omega_\odot t\right) - 3\omega_\odot t\right) \\ y(t) &= 0 \\ z(t) &= \frac{2}{\omega_\odot}\Delta V_x \left(\cos\left(\omega_\odot t\right) - 1\right) \end{aligned} \tag{2.9}$$

Tangential boost transfer along V_{bar}

The manoeuvre consists of two V_{bar} impulses given in opposite directions. The first ΔV_{x1} is applied in point x_1 pointing in the opposite direction of the desired transfer, while the second impulse ΔV_{x2} to stop the relative motion is provided after an orbital period T when $x_2(T) = x_1 - \frac{6\pi}{\omega_\odot}\Delta V_{x1}$ and $z_2(T) = z_1 = 0$. Both the impulses have the same magnitude:

$$\begin{aligned} |\Delta V_{x1}| = |\Delta V_{x2}| &= \frac{\omega_\odot}{6\pi}\Delta x_{desired} \\ |\Delta V_{total}| &= \frac{\omega_\odot}{3\pi}\Delta x_{desired} \end{aligned} \tag{2.10}$$

The manoeuvre, a schematic representation of which is reported in Fig. 2.7, is usually adopted in case a V_{bar} final approach has been selected since it allows to acquire another position laying on the $x-$axis itself after an orbital period. In the ideal case, the end point of such a transfer could be exploited as a hold point since orbital dynamics naturally allow to remain on the V_{bar} axis without requiring any control force and, even taking into account small position/velocity errors which could be present in reality, the hold point along V_{bar} will always remain characterised by low propellant consumption.

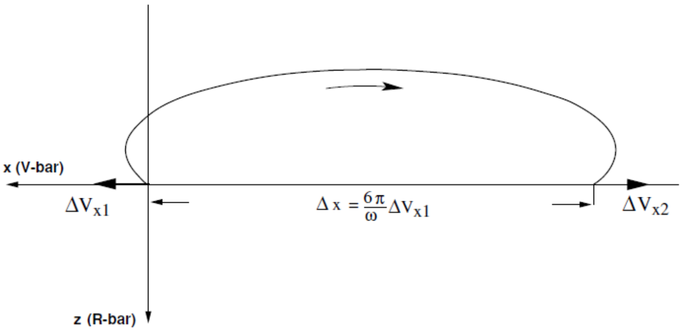

Figure 2.7: Example of tangential boost transfer towards $-V_{bar}$ direction, [9].

Eventually, the manoeuvre could be stopped at $t = kT$ with $k > 1$ to exploit the drift motion that characterise the manoeuvre and continue with the transfer without further propellant consumption.

Tangential boost fly-around

The manoeuvre consists of two V_{bar} impulses, but in this case the objective of the manoeuvre is to acquire an R_{bar} position to begin an R_{bar} final approach. To achieve this goal, the second impulse is provided at $t = \frac{T}{2}$, when the x and z position of the Chaser are $x_2(\frac{T}{2}) = x_1 - \frac{3\pi}{\omega_\odot}\Delta V_{x1}$ and $z_2(\frac{T}{2}) = z_1 - \frac{4}{\omega_\odot}\Delta V_{x1}$. Since the final point of the manoeuvre must lay on R_{bar} it is desired that $x_2 = 0$, which means that x_1 must be $\pm\frac{3\pi}{\omega_\odot}\Delta V_{x1}$, depending on the sign of ΔV_{x1}. The impulses required to execute the manoeuvre are:

$$\begin{aligned}
|\Delta V_{x1}| &= \frac{\omega_\odot}{4}\Delta z_{desired} \\
|\Delta V_{x2}| &= \frac{\omega_\odot}{4}\Delta z_{desired} + \frac{3\omega_\odot}{2}\Delta z_{desired} = \frac{7\omega_\odot}{4}\Delta z_{desired} \\
|\Delta V_{total}| &= 2\omega_\odot\Delta z_{desired}
\end{aligned} \tag{2.11}$$

It must be pointed out that the second impulse is different from the first one because it must not only stop the tangential boost transfer in its midpoint ($\frac{\omega_\odot}{4}\Delta z_{desired}$ as ΔV_{x1}) but also cancel the relative velocity along V_{bar} which naturally characterise a position with $R_{bar} \neq 0$ ($\frac{3\omega_\odot}{2}\Delta z_{desired}$). This causes the total propellant consumption to increase considerably. A schematic representation of the manoeuvre is reported in Fig. 2.8.

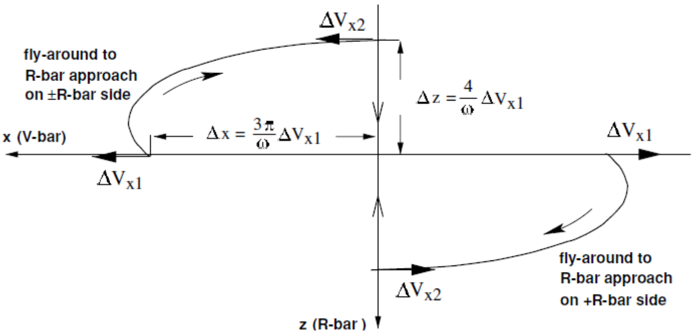

Figure 2.8: Example of tangential boost fly around to acquire both $\pm R_{bar}$ positions, [9].

Manoeuvres for an eventual station keeping or the R_{bar} approach itself must begin immediately after the end of the fly around, otherwise orbital dynamics will cause the Chaser to move away from the Target (further explanations on free drift trajectories can be found in [9]).

2.4.2 Radial thrust manoeuvres

Thrust manoeuvres which features a ΔV in $\pm z$-direction can be used, similarly to tangential manoeuvres, for transfer along the Target orbit and for fly-around to an R_{bar} approach. The main difference between tangential and radial manoeuvres consists of the latter one not changing the orbital period of the Chaser orbit, but just its eccentricity. This means that no global drift motion along V_{bar} occurs in radial manoeuvres. The effect of a ΔV impulse in the positive z direction over a single orbital period can be seen in Fig. 2.9, where the initial conditions are:

$$\begin{cases} x_0,\ y_0,\ z_0 = 0 \\ \dot{z}_0 = \Delta V_z = 0.01\ m/s \\ \dot{x}_0,\ \dot{y}_0 = 0 \end{cases}$$

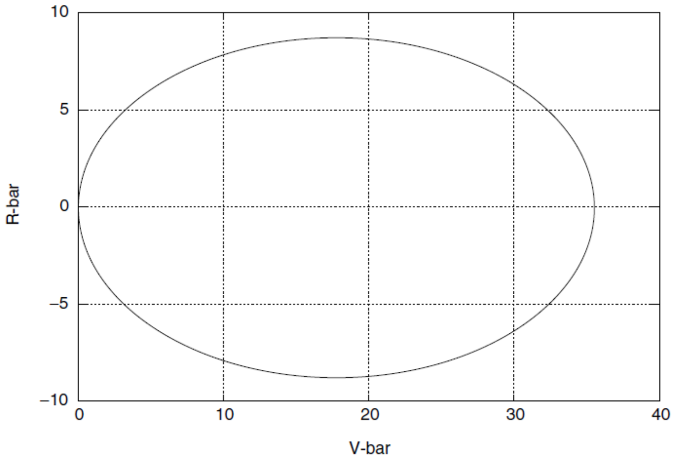

Figure 2.9: Example of relative motion over a period after a $\Delta V_z = 0.01\ m/s$, [9].

The resulting trajectory consists of a looping motion around the Target orbit which causes smaller displacements of the Chaser along both V_{bar} and R_{bar} when compared with the tangential manoeuvre reported in Fig. 2.6. Analytically, this trajectory is described by Eq. 2.12.

$$\begin{aligned} x(t) &= \frac{2}{\omega_\odot}\Delta V_z \left(1 - \cos\left(\omega_\odot t\right)\right) \\ y(t) &= 0 \\ z(t) &= \frac{1}{\omega_\odot}\Delta V_z \sin\left(\omega_\odot t\right) \end{aligned} \tag{2.12}$$

Radial boost transfer along V_{bar}

The manoeuvre consists of two R_{bar} impulses given in same direction. The first ΔV_{z1} is applied in point x_1 pointing towards $+R_{bar}$ if the desired transfer motion is towards $+V_{bar}$ and vice versa, while the second impulse ΔV_{z2} to stop the relative motion is provided after half an orbital period, when $x_2(\frac{T}{2}) = x_1 + \frac{4}{\omega_\odot}\Delta V_{z1}$ and $z_2(\frac{T}{2}) = z_1 = 0$. Both the impulses have the same magnitude:

$$\begin{aligned} |\Delta V_{z1}| = |\Delta V_{z2}| &= \frac{\omega_\odot}{4}\Delta x_{desired} \\ |\Delta V_{total}| &= \frac{\omega_\odot}{2}\Delta x_{desired} \end{aligned} \tag{2.13}$$

A schematic representation of the manoeuvre is reported in Fig. 2.10. Similarly to tangential boosts, radial boosts are usually adopted in case of V_{bar} final approaches but are often even preferred to them, although requiring higher ΔV_{total} thus an higher quantity of propellant. The absence of drifting motion, in fact, may usually be a safety or an operational requirement of the manoeuvre.

In case of no ΔV_{z2} execution, the Chaser would return to the starting point of the manoeuvre at $t = T$, hence no advantages could be obtained by postponing the second impulse;

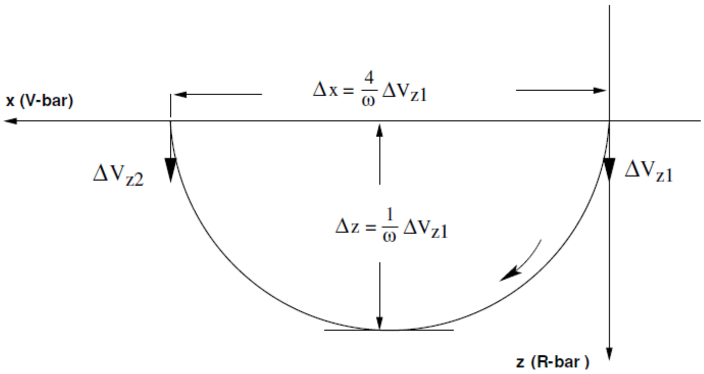

Figure 2.10: Example of radial boost transfer towards $+V_{bar}$ direction, [9].

at the same time, this feature would permit to reattempt the manoeuvre without further fuel consumption in case of GNC system or thrusters failures in x_2.

Radial boost fly-around

The manoeuvre consists of two impulses, the first one, ΔV_{z1}, directed towards $+R_{bar}$ if the starting point is located behind the Target and vice versa, while the second one, ΔV_{x2}, respectively along $\mp V_{bar}$ in order to stop the motion in the V_{bar} direction and acquire an R_{bar} position to begin an R_{bar} final approach. The second impulse is provided at $t = \frac{T}{4}$, when the x and z position of the Chaser are $x_2(\frac{T}{4}) = x_1 + \frac{2}{\omega_\odot} \Delta V_{z1}$ and $z_2(\frac{T}{4}) = z_1 + \frac{1}{\omega_\odot} \Delta V_{z1}$. Since the end point of the manoeuvre must lay on R_{bar} it is desired that $x_2 = 0$, which means that x_1 must be $\mp \frac{2}{\omega_\odot} \Delta V_{z1}$, depending on the sign of ΔV_{z1}. The impulses required to execute the manoeuvre are:

$$\begin{aligned} |\Delta V_{z1}| &= \omega_\odot \Delta z_{desired} \\ |\Delta V_{x2}| &= 2\, |\Delta V_{z1}| = 2\omega_\odot \Delta z_{desired} \\ |\Delta V_{total}| &= 3\omega_\odot \Delta z_{desired} \end{aligned} \tag{2.14}$$

Similarly to tangential boost fly-around, manoeuvres for an eventual station keeping or the R_{bar} approach itself must begin immediately after the acquisition of the end point, otherwise the Chaser will move away from the desired position due to orbital dynamics. A schematic representation of the manoeuvre in case of $+R_{bar}$ endpoint is reported in Fig. 2.11.

Once again, the ΔV cost of the radial manoeuvre results to be higher than the tangential alternative, even though radial boost fly-arounds are often used in inspection missions since the absence of drifting motions allows to continuously loop around the Target following an elliptical trajectory when the second impulse is not executed.

2.4.3 Continous thrust manoeuvres

Previously presented manoeuvres were all impulsive ones, suitable for high thrust level thrusters, such as thermochemicals. In case of low thrust level thrusters, instead, the

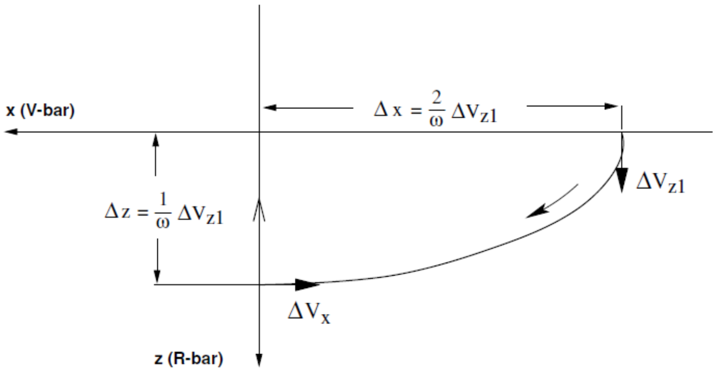

Figure 2.11: Example of radial boost fly around to acquire a $+R_{bar}$ positions, [9].

adoption of continuous thrust manoeuvres is mandatory. Two different types of such manoeuvres can be identified:

- *Continuous thrust manoeuvres having their impulsive counterpart*: these manoeuvres are similar to the ones previously discussed but are suitable for low thrust level thrusters. They demand the application of a constant acceleration in a particular direction throughout the whole trajectory and usually requires double the time than their impulsive counterparts. Since the trajectory executed are similar to those of the corresponding impulsive manoeuvres, thus exploit orbital dynamics, the ΔV required is contained and usually similar to the one of their counterparts.

- *Forced motion continuous thrust manoeuvres*: these manoeuvres forces the Chaser to follow particular trajectories which would not naturally occur, such as straight lines or circular fly-around, or to remain in particular points from which orbital dynamics would cause the s/c to move away (station keeping). Since these manoeuvres are constantly "hampered" by the dynamics characterising free relative motion, ΔV requirements tend to increase considerably.

In Fig. 2.12 an example of a continuous radial thrust transfer along V_{bar} is displayed: the manoeuvre requires the constant radial acceleration $\gamma_z = \frac{\omega_\odot^2}{4*\pi}\Delta x_{desired}$, is characterised by a doubled manoeuvring time, $\Delta t = T$ and a smaller z-displacement, $z_{max} = \frac{1}{2\pi}\Delta x_{desired}$. The total ΔV required is

$$\Delta V_{total} = \gamma_z \Delta t = \frac{\omega_\odot^2}{4*\pi}\Delta x_{desired}\frac{2\pi}{\omega_\odot} = \frac{\omega_\odot}{2}\Delta x_{desired} \tag{2.15}$$

which is the same ΔV of an impulsive radial boost. If the same $\Delta x_{desired}$ had to be covered adopting, for example, a forced straight line along V_{bar}, the amount of ΔV required would have greatly increased.

Further information relative to the first type of continuous thrust manoeuvres and to forced hold points can be found in [9]. Forced straight line manoeuvres, instead, will be discussed in Sec. 2.5, since they are more frequently adopted during the final approach.

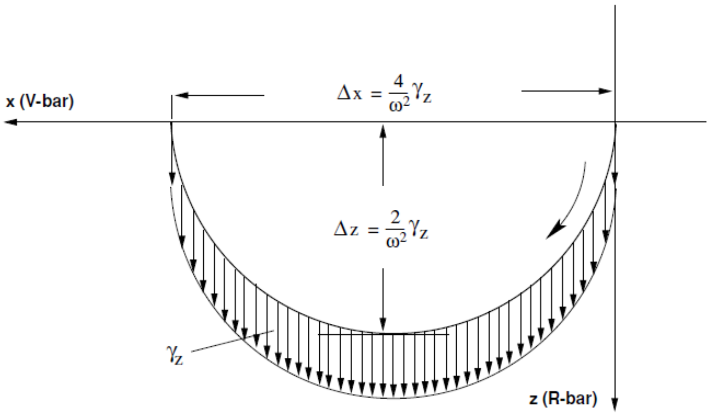

Figure 2.12: Continuous thrust counterpart of a radial boost, [9].

2.5 Final approach

The objective of the final approach phase is to achieve docking or berthing capture conditions in terms of positions and velocities and of relative attitude and angular rates. The accuracy with which these conditions are required to be achieved depends on the typology of mating that will be performed. Focusing just on position accuracy, in case of docking the requirements are about a few centimetres in lateral position and of the order of $1-2\ cm/s$ for axial and lateral linear velocity. In case of berthing, instead, position accuracy about 5 times larger than the one required for docking is still acceptable. In contrast, linear rates requirements are 5 time stricter than the aforementioned values of docking: larger values of relative velocity could make the s/c move too far away from the nominal position during the robotic arm movimentation and eventually leave the berthing box, or could cause drastic multi-body dynamics effects once the robotic arm has grabbed the grapple fixture.

For observability and safety reasons, moreover, a cone-shaped approach corridor, within which the approach trajectory must remain, is often defined and originates from the Target vehicle mating point. Such a corridor is designed so that the Target remains inside the Field of View (FoV) of the on-board sensors throughout the whole final approach. Consequently, the trajectory types used for this phase are usually closed-loop controlled straight line or quasi-straight line approaches which could take place both along V_{bar} or R_{bar} depending on the location of the docking mechanism / berthing box. Even though the final approach manoeuvres are always closed-loop ones, in the following sections open-loop straight line approaches starting from hold points will be shown in order to calculate the nominal ΔV requirements.

2.5.1 Straight line V_{bar} approach

In the simplest case of straight line V_{bar} approach the Chaser is forced to achieve a constant velocity V_x w.r.t. the Target and move from x_1 to x_2, with the velocities in the other directions kept equal to zero. The motion is started with an impulse of ΔV_{x1}, which produces the velocity in the x-direction V_x, and stopped with an impulse of the same magnitude but in the opposite direction ΔV_{x2}, as shown in Fig. 2.13.

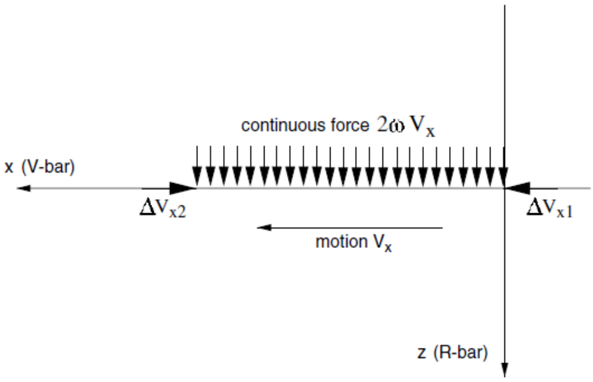

Figure 2.13: Forced straight line motion along V_{bar} starting from the origin, [9].

In order to keep the lateral velocities equal to zero a constant acceleration towards the R_{bar} direction must be applied, the value of which can be derived by Hill's equations and is

$$\gamma_z = 2\omega_{\odot} V_x \tag{2.16}$$

In such way, the equation of motion results to be a simple one dimensional motion with constant velocity $x(t) = x_1 + V_x t$, and the time required to complete the manoeuvre is $\Delta t = \frac{x_2 - x_1}{V_x} = \frac{\Delta x_{desired}}{V_x}$. The total ΔV required by the forced straight line motion is

$$|\Delta V_{total}| = |\Delta V_{x1}| + \overbrace{|2\omega_{\odot} \Delta x_{desired}|}^{|\gamma_z \Delta t|} + |\Delta V_{x2}| \tag{2.17}$$

It is clearly possible to observe that this kind of manoeuvre is way more expensive than all the impulsive V_{bar} transfers previously discussed, since the second term of ΔV_{total} alone is four times greater than the total ΔV required for a radial boost transfer of the same $\Delta x_{desired}$.
Eventually the manoeuvre could be executed following a x-velocity profile: in this case, the lateral acceleration would be time-varying, following the law $\gamma_z(t) = 2\omega_{\odot} V_x(t)$, and the ΔV_{total} would be calculated through a time integration of $\gamma_z(t)$.

2.5.2 Straight line R_{bar} approach

Similarly to the previous case, this manoeuvre is characterised, in its simplest case, by a straight line motion with constant velocity V_z which moves the Chaser from z_1 to z_2, with the velocities in the other directions kept equal to zero. The motion is started with an impulse of ΔV_{z1}, which takes the velocity in the z-direction from zero to V_z, and stopped with an impulse of the same magnitude but in the opposite direction ΔV_{z2}, as shown in Fig. 2.14.

In order to keep the lateral velocities equal to zero, this time, both a continuous x-acceleration and a linearly varying z-acceleration must be applied. These accelerations,

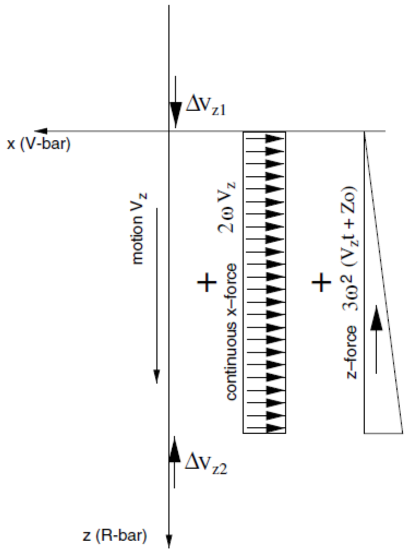

Figure 2.14: Forced straight line motion along R_{bar} starting from the origin, [9].

obtained from Hill's equations, are calculated as

$$\begin{aligned} \gamma_x &= -\,2\omega_\odot V_z \\ \gamma_z &= -\,3\omega_\odot^2 z = -3\omega_\odot^2\left(z_1 + V_z t\right) \end{aligned} \tag{2.18}$$

where $z(t) = z_1 + V_z t$ is the equation describing the Chaser motion. The time required to complete the manoeuvre is $\Delta t = \frac{z_2 - z_1}{V_z} = \frac{\Delta z_{desired}}{V_z}$ and the total ΔV required is

$$|\Delta V_{total}| = |\Delta V_{z1}| + \overbrace{\left|-2\omega_\odot \Delta z_{desired}\right|}^{|\gamma_x \Delta t|} + \overbrace{\left|-3\omega_\odot^2 \frac{z_2^2 - z_1^2}{2}\right|}^{\left|\int_{t_1}^{t_2} \gamma_z \; dt\right|} + |\Delta V_{z2}| \tag{2.19}$$

The propellant consumption characterising this manoeuvre, therefore, is even higher than the one required by a straight line V_{bar} approach since the acceleration required must include also the γ_z term which would be required to perform an hold point with $z \neq 0$. Once again, the manoeuvre could be executed following a z-velocity profile: in this case, both the lateral acceleration would be time-varying, following the law $\gamma_x(t) = -2\omega_\odot V_z(t)$ and $\gamma_z = -3\omega_\odot^2(z_1 + V_z(t)t)$, and the ΔV_{total} would be calculated through a time integration of both $\gamma_x(t)$ and $\gamma_z(t)$.

2.6 Operational and safety considerations

The choice between the previously described manoeuvres is usually strongly driven by the global strategy selected for the rendezvous. For example, straight line R_{bar} approaches are usually avoided unless the mating interface of the Target is located in a point which is difficult to reach from V_{bar}. Fly-around manoeuvres are usually adopted only in case of inspections operations or when the final approach is designed to be along an axis different from V_{bar}.

Other important factors which must be taken into account are operational and safety ones. As for operations, some missions could have the operational requirement to begin and end each rendezvous manoeuvre in an orbital period so that the satellites result to be inside the visibility cone of a particular ground station or in the same illumination conditions during the execution of both the impulses: in these cases, tangential boost transfers along V_{bar} should be preferred. Otherwise, when such operational requirements do not exist, radial boost transfers along V_{bar} could be adopted, since they required half the time to cover the same $\Delta x_{desired}$ with a slightly increased fuel consumption.
Safety considerations, anyway, often have a much heavier impact on the manoeuvre selection. The main safety aspects characterising a manoeuvre are its sensitivity to velocity changes and its *passive safety* properties. The former factor is linked to the quantity of displacement of the actual endpoint w.r.t. the nominal one caused by a difference in the first ΔV provided. As it could be derived from Sec. 2.4.1 and 2.4.2, tangential boost transfers tend to be much more sensitive to ΔV errors, showing x and z-displacements respectively $\frac{3\pi}{2}$ and 4 times greater than those of radial boosts. As for the latter aspect, a manoeuvre can be defined passively safe if its natural development is collision free at least in relation to the short-term. From Fig. 2.15 it is possible to deduce that in case of partial boosts at the beginning or at the end of the trajectory, i.e. (b) and (c), or in case of incapability to execute the second boost, i.e. (a), tangential boost transfers would naturally continue to loop towards the Target, with a large chance that at one of the following apogees the Target is hit, or that the perigee is of the same order of magnitude as the extension of the Target geometry in the z-direction and therefore the Target will be hit in any case. Thus, tangential boost transfers are characterised by bad passive safety properties and usually requires the design of Collision-Avoidance Manoeuvres (CAM), the discussion of which is further the objectives of this work. On the contrary, Fig. 2.16 shows that radial boost counterparts are characterised by an higher level of passive safety since in case of partial boost at the trajectory extremes, i.e. (b) and (c), the trajectory continues to loop near the starting or the end point of the manoeuvre respectively, while in case the second boost

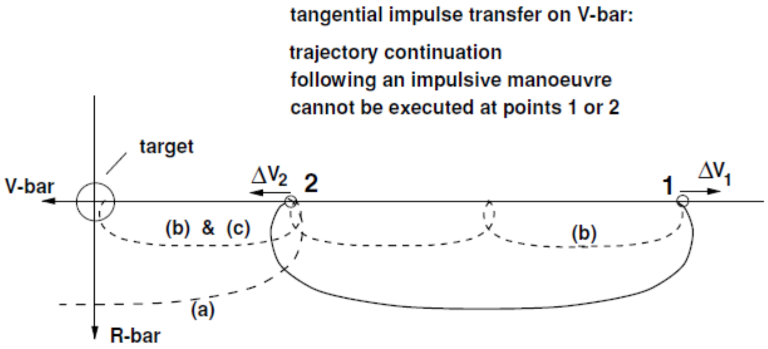

Figure 2.15: Natural evolution of tangential boost transfers, [9].

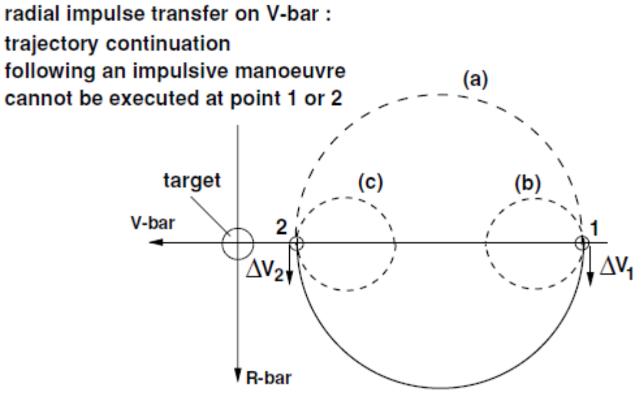

Figure 2.16: Natural evolution of radial boost transfers, [9].

should not be performed at all, the Chaser would naturally return to the starting point.

Considering all the factors above mentioned, therefore, radial boost manoeuvres are usually adopted during the closing phase and preferred to tangential ones unless in explicit contrast with some operational requirements, while V_{bar} closed-loop forced straight line motion is selected as the final approach manoeuvre every time the mating interface is conveniently reachable from the V_{bar} axis itself.

Chapter 3

The Navigation algorithm design

This chapter firstly provides a description of the State-Space representation of a physical system. Afterwards, a general explanation regarding observer-based Navigation algorithms and the Sliding-Mode technique is used to introduce the discussion and the comparison of the particular Sliding-Mode Observers evaluated and designed in the thesis work.

3.1 The State-Space representation

The *state-space representation* is the mathematical model describing a physical system as a set of input, output and state variables related by a set of first-order differential equations. State variables are variables describing the dynamic evolution of the system itself and whose evolution over time depends only on the values they assume at any given time and on the externally imposed inputs. They form the so-called the *state vector* which describes not only the actual state of the system, but also how the state is varying over time. As an example, for navigation purposes the state vector is a set of data describing where an object is in space and how it is moving, while the forces externally acting on the object are represented as input variables. Output variables, instead, usually consist of those variables which are "provided" by the system to something else, for examples the state variables actually measurable with the aid of sensors.

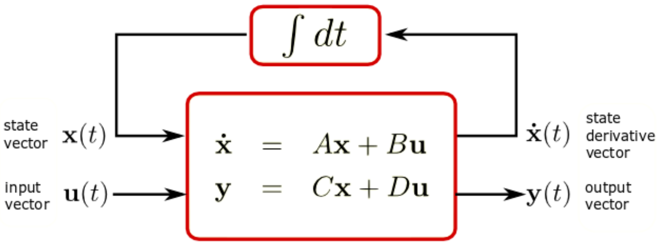

Figure 3.1: State-space representation of a physical system.

Continuous time systems described by the set of first-order differential equations can either be linear or non-linear, as well as time-invariant or time-variant. The simplest case is the one of Linear Time-Invariant (LTI) systems, which is the actual system represented in Fig. 3.1. In such systems $\mathbf{x}(t),\ \dot{\mathbf{x}}(t) \in \mathbb{R}^n$, respectively the state vector and its first derivative, $\mathbf{u}(t) \in \mathbb{R}^m$, the input vector, and $\mathbf{y}(t) \in \mathbb{R}^p$, the output vector, are the only time-dependent elements. The matrices $A \in \mathbb{R}^{n\times n},\ B \in \mathbb{R}^{n\times m},\ C \in \mathbb{R}^{p\times n},\ D \in \mathbb{R}^{p\times m}$, respectively the state, the input, the output and the feed-forward matrices, are constant elements. When these matrices vary over time, instead, the system is called Linear Time-Variant.
In non-linear systems, the matrix expression above explained is substituted by

$$\begin{aligned}\dot{\mathbf{x}}(t) &= f\left(t, \mathbf{x}(t), \mathbf{u}(t)\right) \\ \mathbf{y}(t) &= h\left(t, \mathbf{x}(t), \mathbf{u}(t)\right)\end{aligned} \tag{3.1}$$

where the first is the state equation and the latter the output equation. In this case, it is the eventual time dependency of functions f and h to determine whether the system is Non-Linear Time-Invariant or Time-Variant.

The knowledge of state variables, therefore, is fundamental to determine at any given time the present state and the future evolution of the system and be able to control its behaviour. Thus, algorithms able to calculate and provide the best estimate of the state $\mathbf{x}$ of a dynamic system starting from noisy measurements of the output $\mathbf{y}$ are required. This task is carried out by Navigation algorithms.

3.2 Kalman Filters and State Observers

In the design of systems to control the movement of vehicles, Navigation algorithms aim to provide the best estimate of the vehicle location and velocity. Two main approaches could be followed to perform such a task:

- *Filtering approach*: starting from noisy measurements of the states, the approach extracts the required information from the signal ignoring everything else. The performance of the task is measured using a loss function and the filter acts to minimise this function, i.e. achieving the optimal estimate of $\mathbf{x}$.

- *Observation approach*: starting from noisy measurements of some of the states, the approach asymptotically estimates the whole state vector $\mathbf{x}$ through a recursive correction of the state estimate with the error between the system measured and the estimated output.

Kalman Filters (KF) are the main example of the former type of navigation algorithms. This recursive algorithm is suitable for linear systems and provides the best possible estimates in the minimum-mean-square-error sense, since the loss function minimised is indeed based on the mean square error between the predicted and the measured state, [17]. Its optimal behaviour, however, is based on the assumption that both measurement noise and system uncertainties are characterised by a Gaussian distribution with known standard deviation σ, used to build respectively the covariance matrices R and Q which are fundamental to calculate the Kalman gain K_k and calculate the state estimate for the next time step. The algorithm, therefore, requires statistic knowledge of noises and uncertainties and does not provide any robustness in case this knowledge is missing. A schematic representation how a Kalman filter operate is reported in Fig. 3.2, where P_k is the covariance matrix associated to the state mean square error. An extension to non-linear systems could be provided by the Extended Kalman Filter (EKF) which, anyway, requires a linearisation of model dynamics around the present state.

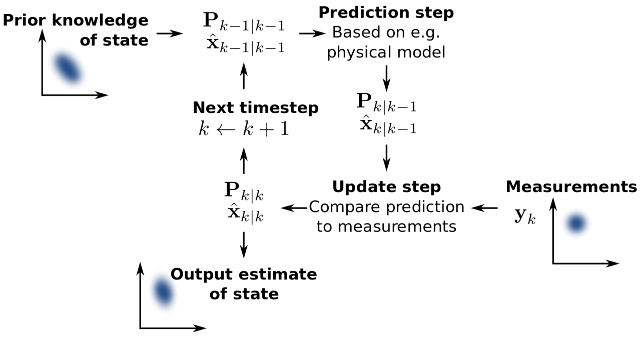

Figure 3.2: Schematic process characterising Kalman Filter, [18].

The second approach presented, the observation [19], could be applied both to linear and non-linear systems - depending on the algorithm adopted - and is capable of providing an estimate of the state variables even without any statistic knowledge of noise or uncertainties. For sake of simplicity, let us explain how a simple linear observer works considering a LTI system.

$$\begin{aligned}\dot{\mathbf{x}}(t) &= A\mathbf{x}(t) + B\mathbf{u}(t) + \mathbf{w}(t)\\ \mathbf{y}(t) &= C\mathbf{x}(t) + D\mathbf{u}(t) + \boldsymbol{\zeta}(t)\end{aligned} \tag{3.2}$$

In Eq. 3.2, the terms $\mathbf{w}(t) \in \mathbb{R}^n$ and $\boldsymbol{\zeta}(t) \in \mathbb{R}^p$ added to the classical LTI state-space representation consist respectively of the plant disturbances and the measurement noise. Since these terms are not known but assumed to be bounded, the idea is to build an observer capable of correcting the state estimates exploiting the discrepancy between the estimated and the measured output. The observer is written in the form

$$\begin{aligned}\dot{\hat{\mathbf{x}}}(t) &= A\hat{\mathbf{x}}(t) + B\mathbf{u}(t) + G\left(\hat{\mathbf{y}}(t) - \mathbf{y}(t)\right)\\ \hat{\mathbf{y}}(t) &= C\hat{\mathbf{x}}(t) + D\mathbf{u}(t)\end{aligned} \tag{3.3}$$

where $\dot{\hat{\mathbf{x}}}(t)$, $\hat{\mathbf{x}}(t)$, $\hat{\mathbf{y}}(t)$ are respectively the estimates of the state vector $\mathbf{x}(t)$, its time derivative $\dot{\mathbf{x}}(t)$ and the output $\mathbf{y}(t)$. The matrix $G \in \mathbb{R}^{n\times p}$ is the gain matrix which, designed by the user, is multiplied by the output error $\mathbf{e}_y(t) = \hat{\mathbf{y}}(t) - \mathbf{y}(t)$, forming the feedback correction term. The observer error $\mathbf{e}(t) = \hat{\mathbf{x}}(t) - \mathbf{x}(t)$ evolves following the system

$$\begin{aligned}\dot{\mathbf{e}}(t) = A\hat{\mathbf{x}}(t) + B\mathbf{u}(t) + G\left(C\hat{\mathbf{x}}(t) + D\mathbf{u}(t) - C\mathbf{x}(t) - D\mathbf{u}(t) - \boldsymbol{\zeta}(t)\right) +\\ - A\mathbf{x}(t) - B\mathbf{u}(t) - \mathbf{w}(t) = \left(A - GC\right)\mathbf{e}(t) - \mathbf{w}(t) - G\boldsymbol{\zeta}(t)\end{aligned} \tag{3.4}$$

The evolution over time of $\mathbf{e}(t)$, therefore, depends on the eigenvalues of the matrix $(A - GC)$. It is now time to check the *observability* of the system, i.e. the measure for how well internal states of a system can be inferred by knowledge of its external outputs. It is possible to state that a LTI system is observable if

$$\operatorname{rank}\begin{bmatrix} C \\ CA \\ \vdots \\ CA^{n-1} \end{bmatrix} = n \tag{3.5}$$

Under the assumption that the system is observable, it will always be possible to find a G matrix such that the observer error evolution described by the system in Eq. 3.4 is asymptotically stable, i.e. all the eigenvalues of $(A - GC)$ are characterised by strictly negative real parts. The gain matrix G should be chosen through a trade-off study, since high gain values would lead to strongly negative real part eigenvalues, which means fast error decay, but would accentuate the effect of measurement noise $\boldsymbol{\zeta}(t)$ at the same time. Lastly, if the error system is asymptotically stable, then bounded plant disturbances $\mathbf{w}(t)$ and measurement noise $\boldsymbol{\zeta}(t)$ will result in the observer error being bounded. This linear form of observer is usually referred to as Luenberger Observer in literature.

Considering the advantages deriving from the observers capability to reconstruct the state vector without requiring any knowledge on plant or measurement noises, the present work focuses on the design of observer-based navigation algorithms. However, since Luenberger -like observers could often be unable to force the output estimation error to zero and make the estimated states converge to the system state in presence of unknown signals or uncertainties, the design choice is to exploit the robust Sliding-Mode technique for observation tasks. The effectiveness of these type of observers in comparison to KFs and EKFs has already been proved in other works, [11, 12].

3.3 Sliding-Mode technique

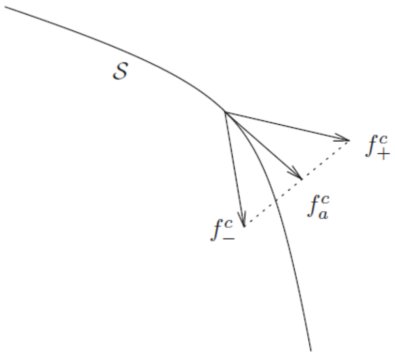

Figure 3.3: Schematic representation of the action of the Sliding-Mode technique, [20].

The founding idea at the basis of the Sliding-Mode technique is to force a certain system states to evolve following a certain *sliding surface*

$$\mathcal{S} = \{\mathbf{x} \ : \ \sigma(\mathbf{x}) = \mathbf{0}\} \tag{3.6}$$

where $\sigma(\mathbf{x})$ is called *sliding variable*. $\mathcal{S}$ represents a reduced-order motion w.r.t. the original system dynamics. In order to slide on this surface, the approach requires the adoption of a discontinuous and switching law which, with an ideally infinite switching frequency, uses different laws to redirect the states towards the sliding surface, as in Fig. 3.3.
As an example, consider the $\mathbf{x}$ vector in Eq. 3.2 to be formed by two terms $x_1,\ x_2$ with $x_2 = \dot{x}_1$ and suppose we want to exploit a first-order Sliding-Mode control algorithm to achieve the desired state vector is $\mathbf{x}_{des} = \begin{bmatrix}0, & 0\end{bmatrix}$. Suppose that the desired reduced-order motion to achieve the desired state is described by a homogeneous linear time-invariant differential equation

$$\dot{x}_1 + cx_1 = 0, \quad c > 0 \tag{3.7}$$

in which no effect of the disturbances introduced in the system by $\mathbf{w}$ is observed. In order to achieve asymptotic convergence of the states to zero even in presence of the disturbance $\mathbf{w}$ it is necessary to define the sliding variable $\sigma(x_1, x_2) = \dot{x}_1 + cx_1 = x_2 + cx_1$ and drive it to zero in finite time. The control law $u = -cx_2 - \rho\,\mathrm{sign}(\sigma)$, with ρ being a positive constant, is suitable to achieve this task and can be obtained applying the Lyapunov functions technique to the σ-dynamics, [20]. The value of ρ is obtainable through the *reachability condition* $\sigma\dot{\sigma} < 0$, again [20]. From the evolution in the state-space reported in Fig. 3.4, it is clearly possible to identify two phases, the *reaching* and the *sliding phase*.

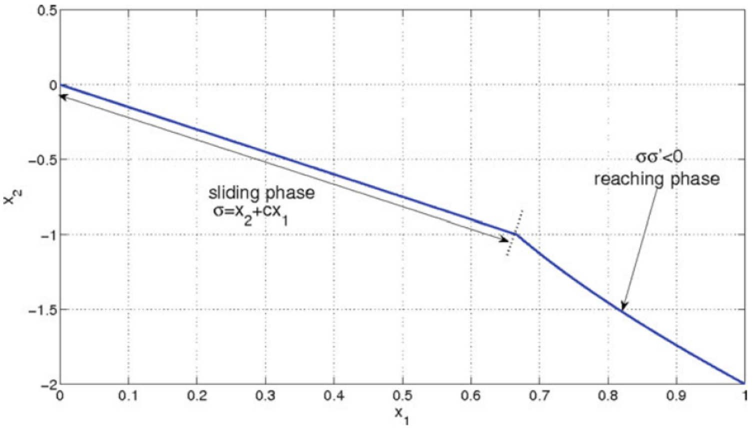

Figure 3.4: Phase portrait of the states evolution, [20].

In the first, the Sliding-Mode technique acts continuously in order to take system states towards the sliding surface $\sigma(x_1, x_2) = 0$ in finite time. Afterwards, in the sliding phase the states evolution follows the designed reduced-order dynamics until system asymptotically reaches the desired state vector, in this case $\mathbf{x}_{des} = \begin{bmatrix}0, & 0\end{bmatrix}$. The sliding motion achieved in the second phase, however, is characterised by a "zig zag" behaviour caused by the impossibility to achieve the ideal infinite switching frequency, Fig. 3.5, and this undesired phenomenon is called *chattering*. Furthermore, the chattering behaviour strongly characterises also the time evolution of the control law u which is switching at high frequency and, therefore, usually difficult to reproduce through realistic actuators.
High-order Sliding-Mode algorithms could eventually be able to achieve better performances reducing the chattering behaviour and forcing both the sliding variables and the

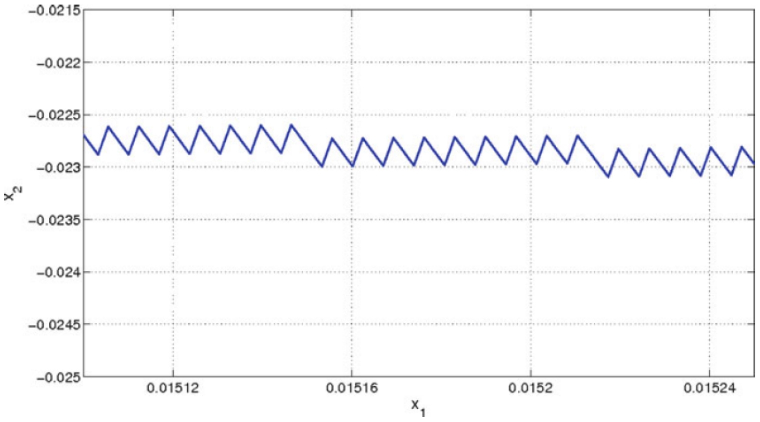

Figure 3.5: Chattering behaviour during the sliding phase, [20].

system states to zero in finite time [20].

3.4 Sliding-Mode Observers

Unlike Luenberger-type observers which use linear feedback correction terms, Sliding-Mode Observers (SMOs) exploit the sign function to provide the observer model with an highly non-linear feedback injection term. Differently from what explained in the general case of Sliding-Mode control in Sec. 3.3, in SMO:

- the sliding variable is usually chosen to be the error between the estimated and measured output $\mathbf{e}_y$ so that, when the sliding surface $\mathcal{S}$ is reached, $\mathbf{e}_y = 0$;

- the feedback injection term $\boldsymbol{\nu}$ becomes the switching law which must be designed to reach the sliding surface and correctly observe system states, similarly to how the control law $\mathbf{u}$ was designed to control system states.

This approach augments the algorithm robustness, forces the output estimation to converge to zero in *finite time* and is even able to reconstruct unknown disturbances acting on the system. The estimated states convergence to the system states, instead, depends on the order of the algorithm: it is asymptotic in case of first-order SMOs, while achieved in finite time adopting high-order SMOs. As for chattering behaviour, first-order SMOs estimates are more affected than high-order SMOs ones and low operating frequencies accentuate the criticality. However, the chattering phenomenon results to be critical only in the system state estimates and not in the discontinuous behaviour of $\boldsymbol{\nu}$, since the feedback injection term is just a computational term and does not need to be reproduced by any physical instrument. Nevertheless, the effect can be contained through an accurate parameter tuning.

In the following sections two different first-order SMOs suitable for the observation of linear systems, like Hill's equations, are described and compared.

3.4.1 First-Order classic linear SMO

Consider a nominal linear system as in Fig. 3.1 characterised by null feed-forward matrix D. Assume that the output matrix C has full row rank, i.e. each of the measured outputs is independent, and that the matrix pair (A, C) is observable, i.e. follows Eq. 3.5. Considering the coordinate transformation $\mathbf{x} \to T_c\mathbf{x}$ associated with the invertible matrix

$$T_c = \begin{bmatrix} N_c^T \\ C \end{bmatrix}$$

where $N_c \in \mathbb{R}^{n\times(n-p)}$ spans the null space of C, it is possible to apply the transformation to the triple (A, B, C) and rewrite them as

$$T_c A T_c^{-1} = \begin{bmatrix} A_{11} & A_{12} \\ A_{21} & A_{22} \end{bmatrix}, \quad T_c B = \begin{bmatrix} B_1 \\ B_2 \end{bmatrix}, \quad C T_c^{-1} = \begin{bmatrix} 0 & I_p \end{bmatrix}. \tag{3.8}$$

where $A_{11} \in \mathbb{R}^{(n-p)\times(n-p)}$ and $B_1 \in \mathbb{R}^{(n-p)\times m}$. A simple first-order linear SMO to observe the linear system presented is

$$\begin{aligned} \dot{\hat{\mathbf{x}}}(t) &= A\hat{\mathbf{x}}(t) + B\mathbf{u}(t) + G_n\boldsymbol{\nu} \\ \hat{\mathbf{y}}(t) &= C\hat{\mathbf{x}}(t) \end{aligned} \tag{3.9}$$

where $(\hat{\mathbf{x}}, \hat{\mathbf{y}})$ are the estimates of $(\mathbf{x}, \mathbf{y})$ and $\boldsymbol{\nu}$ is the discontinuous injection term defined component-wise as $\nu_i = \rho \operatorname{sign}(e_{y,i}),\ i = 1, ..., p$. Furthermore, $\mathbf{e}_y(t) = \hat{\mathbf{y}}(t) - \mathbf{y}(t)$ and $\mathbf{e}_(t) = \hat{\mathbf{x}}(t) - \mathbf{x}(t)$ are respectively the output and the state estimation errors and ρ is a positive constant. The feedback injection term, therefore, is designed to be discontinuous w.r.t. the sliding surface $\mathcal{S} = \{\mathbf{e} \in \mathbb{R}^n : C\mathbf{e} = \mathbf{e}_y = \mathbf{0}\}$ to force the trajectory of $\mathbf{e}(t)$ onto $\mathcal{S}$ in finite time and achieve $\mathbf{e}_y = \mathbf{0}$ during the sliding phase. Assuming that the linear system is already written as in Eq. 3.8, the structure of the gain matrix G_n is

$$G_n = \begin{bmatrix} L \\ -I_p \end{bmatrix} \tag{3.10}$$

where $L \in \mathbb{R}^{(n-p)\times p}$ represents the design freedom left to the user. Consequently, the observer error dynamics can be written as

$$\dot{\mathbf{e}}(t) = A\mathbf{e}(t) + G_n\boldsymbol{\nu}.$$

Considering the structure presented in Eq. 3.8 and partitioning the state estimation error as $\mathbf{e}(t) = \operatorname{col}(\mathbf{e}_1, \mathbf{e}_y)$ with $\mathbf{e}_1 \in \mathbb{R}^{n-p}$, the error dynamics can be rewritten in the form

$$\dot{\mathbf{e}}_1(t) = A_{11}\mathbf{e}_1(t) + A_{12}\mathbf{e}_y(t) + L\boldsymbol{\nu}, \tag{3.11}$$

$$\dot{\mathbf{e}}_y(t) = A_{21}\mathbf{e}_1(t) + A_{22}\mathbf{e}_y(t) - \boldsymbol{\nu}. \tag{3.12}$$

Rewriting Eq. 3.12 component-wise as

$$\dot{e}_{y,i}(t) = A_{21,i}\mathbf{e}_1(t) + A_{22,i}\mathbf{e}_y(t) - \rho \operatorname{sign}(e_{y,i}),$$

where $A_{21,i}$ and $A_{22,i}$ represent the i^{th}-rows of A_{21} and A_{22}, it is possible to formulate the reachability condition for this SMO:

$$\begin{aligned} e_{y,i}\dot{e}_{y,i} &= e_{y,i}(A_{21,i}\mathbf{e}_1 + A_{22,i}\mathbf{e}_y) - \rho|e_{y,i}| \\ &< -|e_{y,i}|\left(\rho - |A_{21,i}\mathbf{e}_1 + A_{22,i}\mathbf{e}_y|\right). \end{aligned} \tag{3.13}$$

Now choosing the scalar ρ large enough is it possible to obtain

$$\rho > |A_{21,i}\mathbf{e}_1 + A_{22,i}\mathbf{e}_y| + \eta \quad \rightarrow \quad e_{y,i}\dot{e}_{y,i} < -\eta|e_{y,i}|, \tag{3.14}$$

which is the *eta-reachability condition* and implies that $e_{y,i}$ converge to zero in finite time. Once every i^{th}-component of $\mathbf{e}_y$ has converged to zero, a sliding motion on the surface $\mathcal{S}$ takes place.

Remark 1 *It must be pointed out that this is not a global result since for any given* ρ*, there will exist observer initial conditions causing an estimate error large enough that Eq. 3.14 is not satisfied. The region in which* $\mathbf{e}_1(0)$ *and* $\mathbf{e}_y(0)$ *must lie for the sliding motion to occur is called the sliding patch associated with that particular* ρ*. To enlarge this area it is possible either to increase* ρ *either to add a linear feedback injection term to the observer, the second method being preferable to avoid excessive chattering.*

Since during the sliding motion $\mathbf{e}_y(t) = \dot{\mathbf{e}}_y(t) = 0$, the error dynamics will collapse in the form

$$\dot{\mathbf{e}}_1(t) = A_{11}\mathbf{e}_1(t) + L\boldsymbol{\nu}_{eq} \tag{3.15}$$

$$\mathbf{0} = A_{21}\mathbf{e}_1(t) - \boldsymbol{\nu}_{eq} \tag{3.16}$$

where $\boldsymbol{\nu}_{eq}$ is the so-called *equivalent output error injection term* required to maintain the sliding motion on $\mathcal{S}$. Substituting Eq. 3.16 in 3.15 it is possible to obtain

$$\dot{\mathbf{e}}_1(t) = (A_{11} + LA_{21})\,\mathbf{e}_1(t) \tag{3.17}$$

which represents the reduced-order motion of order $n-p$ characterising the sliding motion. It is clear how the choice of the matrix L is fundamental to ensure that the motion is stable and determine to eigenvalues of the matrix $(A_{11} + LA_{21})$, i.e. the speed of the asymptotic convergence of the state estimate error $\mathbf{e}(t)$ to zero.

3.4.2 First-Order robust linear SMO

This time, consider a linear system which is characterised by bounded matched uncertainties. This means that system uncertainties bounds and the matrix through which these uncertainties operate on the system are known.

$$\begin{aligned} \dot{\mathbf{x}}(t) &= A\mathbf{x}(t) + B\mathbf{u}(t) + Bf(t, \mathbf{y}, \mathbf{u}) \\ \mathbf{y}(t) &= C\mathbf{x}(t) \end{aligned} \tag{3.18}$$

where $f : \mathbb{R}_+ \times \mathbb{R}^p \times \mathbb{R}^m \rightarrow \mathbb{R}^m$ represents the lumped uncertainties or non-linearities of the system operating on the system through the matrix B. This formulation is particularly suitable for the case of unknown forces or torques acting on the system, since they are associated to the same input matrix B as the control forces/torques $\mathbf{u}$. Consider an observer of the form

$$\dot{\hat{\mathbf{x}}}(t) = A\hat{\mathbf{x}}(t) + B\mathbf{u}(t) - G_l C\mathbf{e}(t) - P^{-1}C^T F^T \boldsymbol{\nu} \tag{3.19}$$

where $\hat{\mathbf{x}}(t)$ is the estimate of the state vector $\mathbf{x}(t)$ and $\mathbf{e}(t) = \hat{\mathbf{x}}(t) - \mathbf{x}(t)$ is the state estimate error. The symmetric positive definite matrix $P \in \mathbb{R}^{n\times n}$ and the gain matrix $G_l \in \mathbb{R}^{n\times p}$ must satisfy the linear matrix inequality (LMI)

$$PA_0 + A_0^T P < 0 \tag{3.20}$$

where $A_0 = A - G_l C$, and the structural constraint

$$PB = (FC)^T \tag{3.21}$$

for some $F \in \mathbb{R}^{m\times p}$. Lastly, the discontinuous feedback injection term $\boldsymbol{\nu}$ is calculated as

$$\boldsymbol{\nu} = \rho(t, \mathbf{y}, \mathbf{u})\frac{FC\mathbf{e}(t)}{\|FC\mathbf{e}(t)\|} = \rho(t, \mathbf{y}, \mathbf{u})\,\mathrm{sign}\,(FC\mathbf{e}(t)) \tag{3.22}$$

with $\rho(t, \mathbf{y}, \mathbf{u}) \geq \|f(t, \mathbf{y}, \mathbf{u})\|$ in order to have a correction term which is greater than the uncertainties bounds.

Under all of these assumption, the Lyapunov-based method could be used to demonstrate that the quadratic form $V(\mathbf{e}) = \mathbf{e}^{\,T}P\mathbf{e}$ guarantees quadratic stability. Hence, given the formulation of the feedback injection term in Eq. 3.22, the sliding motion takes place on the surface $\mathcal{S}_F = \{\mathbf{e} \in \mathbb{R}^n : FC\mathbf{e} = 0\}$ in finite time. It must be pointed out that, when $p > m$ sliding on $\mathcal{S}_F$ is different from sliding on $C\mathbf{e}(t) = 0$.

3.4.3 Robustness against plant disturbances

The main differences between the two algorithms presented concern their robustness against unknown plant disturbances and uncertainties.

The first-order classic SMO is built considering a linear system without any type of uncertainties and, as detailed in Eq. 3.14 and Remark 1, its robustness is limited to the sliding patch associated to the selected ρ. This means that unknown plant disturbances or uncertainties will create a certain error in the state estimate that, if contained inside the sliding patch, will be followed by another phase of asymptotic convergence. In case of rapid successions of short disturbances or under long lasting uncertainties the algorithm could be unable to return to the correct estimate for long times, strongly decreasing the navigation algorithm accuracy and potentially compromising the whole GNC system effectiveness.

On the contrary, the first-order robust SMO discussed, although requiring little knowledge on the uncertainties bound and distribution on the system, is already built contemplating the presence of these unknown disturbances and is, therefore, able to estimate the whole state vector without losing accuracy.

This different response to plant disturbances is now shown with two examples where the two algorithms are used to observe the states of a Chaser satellite performing two consecutive radial boosts. In the first one it is supposed that the manoeuvres are executed exploiting a thrust of F_{max}, but the navigation algorithms are provided with just half

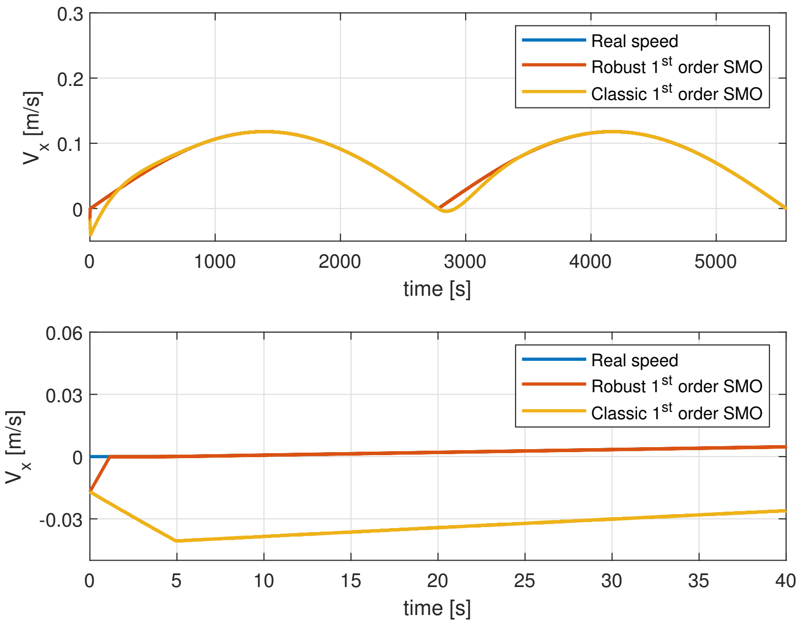

Figure 3.6: Comparison of the x-velocity estimate of the two SMOs presented: whole manoeuvre above, focus on the first 40 s below.

of the knowledge regarding the actuators. This means that, during thrusters firing, the navigation algorithms expect each component u_i of the control force to be just $\frac{F_{max}}{2}$, thus simulating a situation in which a $\frac{F_{max}}{2}$ unknown input is acting on the plant. As it can be clearly seen from Fig. 3.6, after each boost, the velocity estimates of the first-order classic SMO are affected by a certain error which returns to zero in about 1000 s. On the other hand, the first-order robust SMO velocity estimates are characterised by a continuous level of accuracy.
In the second example, instead, a 2 N-sinusoidal disturbance along the y-direction is applied to the Chaser. In this case, the classic first-order SMO algorithm is never able to correctly estimate the y-velocity since the unknown disturbance is constantly applied. On the other hand, the robust SMO estimate is not affected by this problem, as shown in Fig. 3.7.

The first-order robust SMO algorithm, therefore, is preferable and more robust against unknown plant disturbances and uncertainties, although requiring the knowledge relative to their bounds and distribution matrices.

3.4.4 Measurement noise sensitivity

As reported in Eq. 3.2, plant disturbances $\mathbf{w}(t)$ are not the only unknown terms acting on the system, but measurements noise $\boldsymbol{\zeta}(t)$ should be taken in consideration, too. These noises usually consist of high-frequency signals with zero mean value corrupting the output measurements, but their nature largely depend on the nature of the adopted sensor itself. The SMOs presented, although built without any consideration of the term $\boldsymbol{\zeta}(t)$, have a

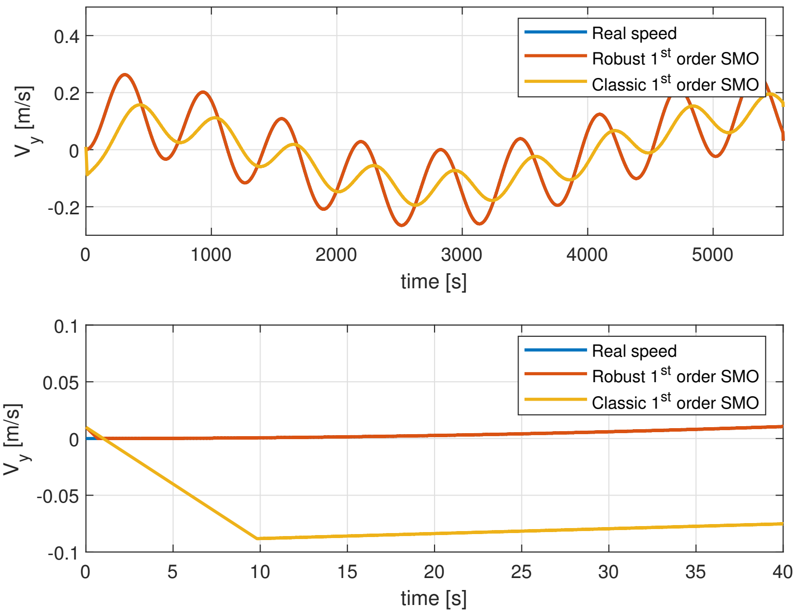

Figure 3.7: Comparison of the y-velocity estimate of the two SMOs presented: whole manoeuvre above, focus on the first 40 s below.

low level of sensitivity w.r.t. noisy output measurements due to the fact that they require a certain time to achieve convergence. This *convergence time*, in fact, makes it impossible for the algorithms to exactly follow the noisy output measurements since they vary with a frequency which is too high. As a result, the observer estimates recreate just the mean trend of the noisy measurement, i.e. reconstruct the output achieving higher levels of accuracy.

Remark 2 *In case the corruption of the output measurement caused by the sensors should be characterised by a mean value different from 0 or low-frequency terms, observer-based algorithms would reconstruct the actual output plus the noise mean value and these low-frequency trends, losing estimates accuracy. In this case, data fusion methods should be designed to "clean" the measurement noise and make its mean value as close to zero as possible.*

3.4.5 Unknown disturbances reconstruction

As mentioned previously, one of the benefits of SMOs over linear Luenberger-like observers is represented by the possibility to reconstruct unknown terms acting on the systems. Once the algorithm has reached the sliding phase, in fact, the equivalent output error injection term $\boldsymbol{\nu}_{eq}$ operates at high frequency to counter any term which would lead the system away from the sliding surface $\mathcal{S}$. Consequently, once the SMO has reached convergence and the state error is close enough to zero, matched disturbances acting on the system could be estimated filtering $\boldsymbol{\nu}_{eq}$ with a low-pass filter. This approach, although introducing a certain delay in the disturbances reconstruction due to the filter itself, is a powerful result because the term $\boldsymbol{\nu}$ was not designed with any a priori knowledge relative to $\mathbf{w}(t)$, except its bounds and distribution matrix.

To provide some examples, the first-order robust SMO is used to reconstruct the unknown plant disturbances in both the cases presented in Sec. 3.4.3 in absence of any measurement noise. Fig. 3.8 shows the reconstruction of the thrusters input unknown part, a $\frac{F_{max}}{2}$ boost, obtained filtering $\boldsymbol{\nu}_{eq,z}$ with a low-pass filter with time constant $\tau = 0.5$. Fig. 3.9, instead, presents the estimate of the 2 N-sinusoidal unknown disturbance along the y-direction, obtained filtering $\boldsymbol{\nu}_{eq,y}$ with the same low-pass filter. The reconstruction error at the beginning and the end of the boost is caused by the convergence time of $\boldsymbol{\nu}_{eq,z}$ to the unknown input signal which makes it impossible for the SMO the reconstruct the

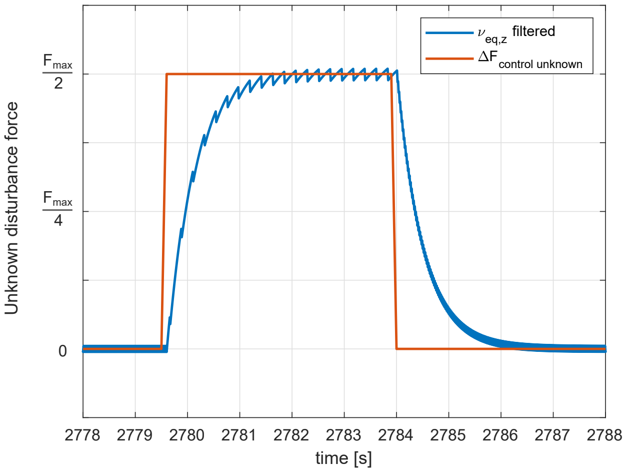

Figure 3.8: Reconstruction of the $\frac{F_{max}}{2}$ unknown part of the control input offered by the first-order robust SMO.

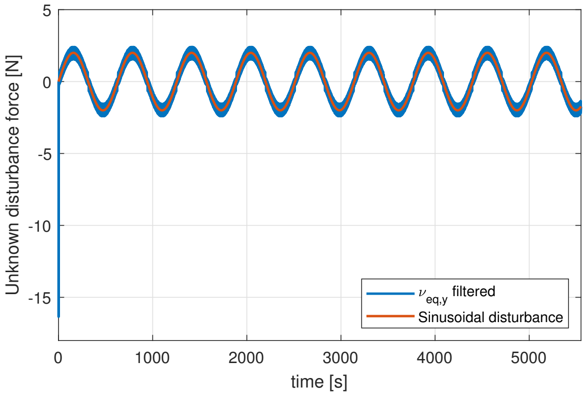

Figure 3.9: Reconstruction of the 2 N-sinusoidal y-direction disturbance offered by the first-order robust SMO.

sudden variation characterising the step. This effect, anyway, is much less evident in case of the sinusoidal disturbance, due to its smoother trend.

Unfortunately, the ability to reconstruct unknown plant disturbances results to be heavily degraded when measurements noise $\boldsymbol{\zeta}(t)$ are taken into account. In this case, the filtered trend of $\boldsymbol{\nu}_{eq}$ is strongly corrupted by noise, making it difficult to recognize unknown inputs.

Chapter 4

The Guidance algorithm design

The present chapter aims to the presentation of the Guidance algorithm designed during this thesis work. At the beginning, the reasons that led to the selection of Artificial Potential Fields (APF) method are discussed. Afterwards, both the classical and the modified version of APF are described in detailed, highlighting the advantages and the potentialities introduced through the selection of harmonic functions. Algorithm adaptations to take into account both moving obstacles and targets are reported, too. Lastly, a description of the Sliding-Mode control algorithm designed to follow the trajectory calculated by APF is provided.

4.1 Guidance algorithm choice

The main goal of Guidance algorithms is to calculate a planned trajectory for translational dynamics. Depending on its nature, Guidance algorithms could directly provide the control acceleration which must be applied to follow the desired path or could simply output the calculated trajectory which should then be reproduced using a Control algorithm. Proportional Navigation Guidance (PNG) and the optimal Zero-Effort-Miss/Zero-Effort-Velocity (ZEM/ZEV) are two major examples of the first type of algorithms. These are often adopted in missile and asteroid interception and their performances have been proved in several works, [21, 22]. Although being effective and *flyable*, i.e. with a low computational cost, these laws usually provides control accelerations profiles assuming that thrust is continuously variable. When the spacecraft is equipped with thrusters characterised by an ON/OFF functioning, however, there is no throttling ability. This means that the control acceleration profile calculated by the guidance law must be provided to another algorithm which must transform the signal into a series of ON/OFF commands for the actual thrusters. Furthermore, neither PNG nor ZEM/ZEV take in consideration the presence of obstacles around the spacecraft.

The Artificial Potential Field, on the other hand, is an analytical method and a computationally efficient algorithm to perform *online* collision-free path computation and belongs to the second family of guidance algorithms. The necessity to pair APF with control algorithms could be exploited and transformed into an advantage in case of ON/OFF thrusters,

since the task to adapt the control input to the actual thrusters functioning could be executed by the control algorithm itself. The method has already shown its effectiveness in both in robotics and aerospace applications, [14, 15, 16], and is one of the main adopted to perform *obstacle avoidance* thanks to its low computational cost.
The intuitive founding idea of the algorithm is to find a function that represents the energy of the system, which is minimal in the position of goal. An artificial potential field is, therefore, built as sum of different fields with global maximum and minimum points to represent respectively obstacles and goal points. In such way, a robot moving inside the field would be naturally attracted towards the goal point by the attractive field, and away from obstacles by the repulsive one. Particularly, the whole artificial potential field $U(\mathbf{r})$, with $\mathbf{r}$ being the position of the robot or, in this case, the Chaser, is the sum of:

- an **attractive field** $U_a(\mathbf{r})$ generally built to represent a single goal point;

- a **repuslive field** $U_r(\mathbf{r}) = \sum U_{r,i}(\mathbf{r})$ generally built to model the presence of multiple obstacles ($i = 1 \dots N_{obs}$ with N_{obs} being the number of obstacles modelled).

One the APF is built, the desired direction of motion is calculated as

$$-\nabla U(\mathbf{r}) = -\nabla \left(U_a(\mathbf{r}) + Ur(\mathbf{r}) \right),$$

in order to reach the goal point avoiding all the obstacles, as reported in the schematic Fig. 4.1.

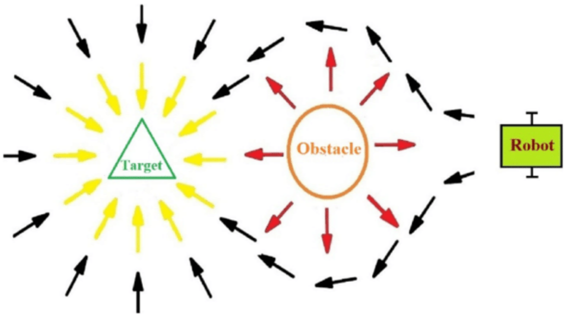

Figure 4.1: APF functioning representation, [23].

In this work, the APF has been selected as guidance algorithm due to its low computational cost and its ability to perform obstacle avoidance, a requirement which is becoming more and more important in the execution of Proximity Operations. Furthermore, the opportunity to choose the form of the different attractive and repulsive fields gives the algorithm design an extreme flexibility, even permitting online field modifications in case new obstacles should be detected by the spacecraft sensors.

4.2 Classical Artificial Potential Field algorithm

The classical APF algorithm, adopted for example in [22], is characterised by a paraboloid and a squared hyperbolic function as the attractive and repulsive fields, respectively.

$$\begin{aligned} U_a(\mathbf{r}) &= \frac{K_a}{2}\eta_a(\mathbf{r})^2, \\ U_{r,i}(\mathbf{r}) &= \frac{K_{r,i}}{2}\left(\frac{1}{\eta_{r,i}(\mathbf{r})} - \frac{1}{\eta_0}\right)^2 \end{aligned} \tag{4.1}$$

where $\eta_a(\mathbf{r}) = \|\mathbf{r}_{goal} - \mathbf{r}\|$ is the distance of the Chaser from the goal point, with $\mathbf{r}_{goal} \in \mathbb{R}^3$ the position vector of the goal expressed in the Target LVLH frame and $\mathbf{r} \in \mathbb{R}^3$ the position vector of the Chaser, obtained through Hill's equations. Moreover, $\eta_{r,i}(\mathbf{r}) = \min_{\forall \mathbf{r}_{obs,i} \in CO_i} \|\mathbf{r}_{obs,i} - \mathbf{r}\|$ is the minimum distance between the Chaser and the obstacles, with CO_i being the convex set of the i^{th}-obstacle points and $\mathbf{r}_{obs} \in \mathbb{R}^3$ being the obstacle position vector, again expressed in the Target LVLH frame. This formulation for η_{r_i} allows the user to eventually consider obstacles with a certain convex geometrical shape, instead of considering them as concentrated in their CoM. Lastly, η_0 is the maximum influence distance of the obstacles, while K_a and $K_{r,i}$ are the attractive and repulsive constants. Fig. 4.2 and 4.3 show respectively the total potential field and its gradient lines in presence of two obstacles in front of the goal point (2D case).

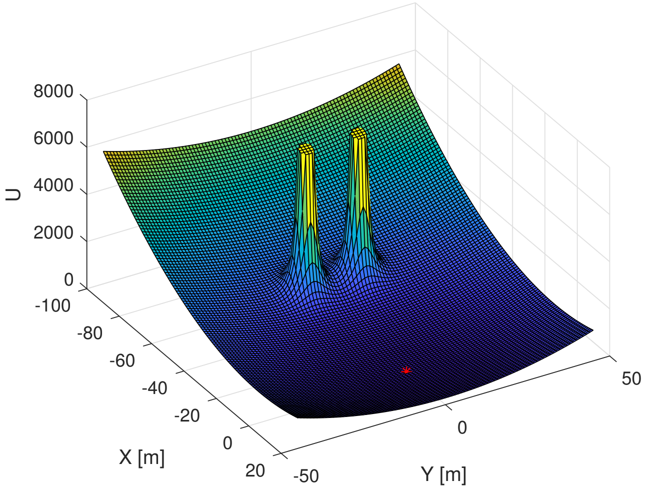

Figure 4.2: Total potential field in case of classic APF, goal point in red.

This formulation is strongly affected by *local minima* phenomena, which means that the Chaser could encounter other minima points before arriving at the goal point and arrest its motion prematurely. This is clearly visible in Fig. 4.3 where the gradient lines converge towards a single point, i.e. the minimum point, before the obstacles. Several modifications have been proposed to overcome this criticality. In [24] 2D local minima points are overcome through an iterative evaluation of the total field U in every possible direction of motion

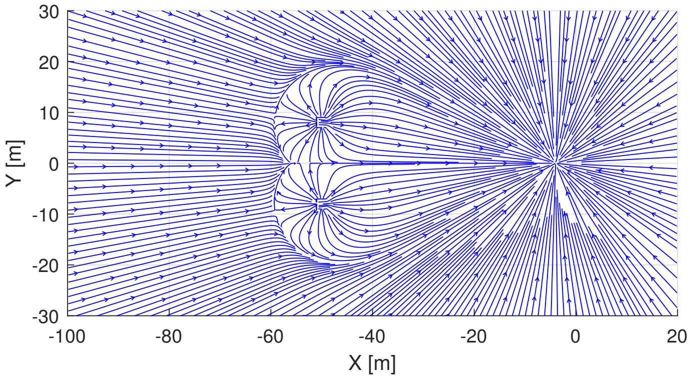

Figure 4.3: Gradient lines of classic APF, showing a minimum point in front of the obstacles.

and using adaptive repulsive gains. This approach, although being effective in robotic 2D applications, is extremely computationally heavy in case of 3D applications, preventing real-time path calculations. In [23], instead, the repulsive field of the objective is augmented through a multiplication by the attractive field. This modification makes the repulsive effect stronger at the obstacle portion which is far from the goal, enforcing the motion in the goal point direction.

4.3 Harmonic functions and local minima

In this work, instead, the selected approach is to build both the attractive and repulsive fields using harmonic functions. These are functions that satisfy the Laplace equation

$$\nabla^2 U(\mathbf{r}) = 0 \quad \forall \mathbf{r} \in \mathbb{D}, \tag{4.2}$$

where $\mathbb{D}$ is the domain of $U(\mathbf{r})$. Examples of such functions can be found in electrostatics and dynamics of incompressible fluids. As for guidance algorithms applications, the most interesting features of harmonic functions are:

- *minimum and maximum principle*: the minimum and the maximum of a non-constant harmonic function occur on the domain boundary.
- *invariance under linear transformations*: linear combinations of harmonic functions are still harmonic functions.

Consequently, regardless how many obstacles or goal points should be modelled, the resulting potential field $U(\mathbf{r})$ will always remain free of local minima. This approach has been exploited in [25, 26] for 2D robotic applications. In the former paper the attractive function is a uniform flow guiding the robot towards the desired direction, while obstacles have been modelled with the multi-panels method. The latter work exploits logarithmic functions both as attractive and repulsive fields, discussing how to tune their gain in order not to cross into the obstacles safety circles. For sake of comparison, it is possible to exploit the logarithmic function to model the presence of two obstacles in a 2D case, as done in Fig. 4.2 and 4.3. The Harmonic APF (HAPF) and its gradient lines, reported in Fig. 4.4 and 4.5, show there is no minimum point in front of the obstacles. In this case, the obstacles form a saddle point, the escape from which is always possible exploiting the second dimension (gradient lines are moving away from the point along the y-direction).

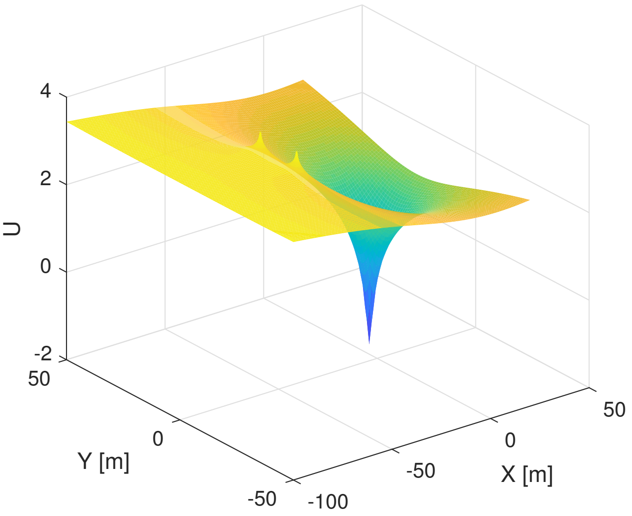

Figure 4.4: Total potential field in case of Harmonic APF.

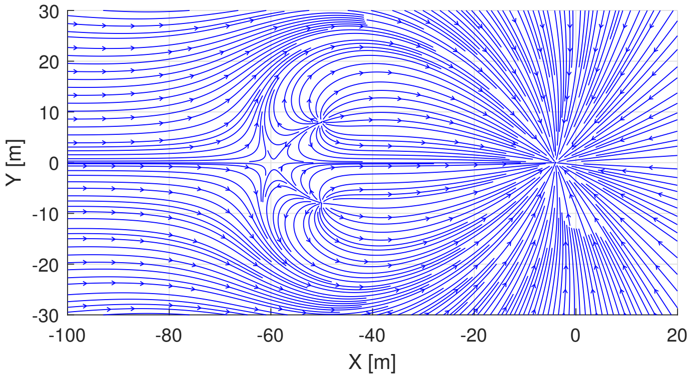

Figure 4.5: Gradient lines of Harmonic APF, showing a saddle point in front of the obstacles.

4.4 Harmonic APF 3D algorithm

As for rendezvous and proximity operations applications, the selection of 3D harmonic function would be advisable in order to maintain the motion freedom along each possible direction. Therefore, it is firstly necessary to analyse the general n-dimensional expression of the Laplace equation in polar coordinate, reported in Eq. 4.3 accordingly to [25].

$$\nabla^2 U(r) = U_{rr} + \frac{n-1}{r} U_r + angular\ terms \tag{4.3}$$

where U_{rr} and U_r are the second and first derivative of the field U w.r.t. the radial distance r, respectively. Assuming spherical symmetry, angular terms are neglected and integrating twice it is possible to obtain:

$$U(r) = \frac{c_1}{r^{n-2}} + c_2 \tag{4.4}$$

where c_1 and c_2 are constants. Observing Eq. 4.4 it is possible to deduce that the hyperbolic field is a 3D harmonic function, thus suitable for 3D applications. Therefore, the local minima-free HAPF algorithm designed is characterised by the following attractive and repulsive fields:

$$\begin{aligned} U_a(\mathbf{r}) &= -\frac{1}{\eta_a(\mathbf{r})} \\ U_{r,i}(\mathbf{r}) &= \begin{cases} q_i \left(\frac{1}{\eta_{r,i}(\mathbf{r})} - \frac{1}{\eta_0} \right) & \text{if } \eta_{r,i} \leq \eta_0 \\ 0 & \text{otherwise} \end{cases} \end{aligned} \tag{4.5}$$

where q_i is the gain of the repulsive field and determine how far from the obstacle the Chaser is allowed to fly, while all the other terms has the same meaning presented with Eq. 4.1. The gradient of the attractive and repulsive fields is calculated as in [16]:

$$\begin{aligned} \nabla_r \left(U_a(\mathbf{r}) \right) &= \frac{\nabla_r \left(\eta_a(\mathbf{r}) \right)}{\eta_a(\mathbf{r})^2} = -\frac{\mathbf{n}_{CG}}{\eta_a(\mathbf{r})^2}, \\ \nabla_r \left(U_{r,i}(\mathbf{r}) \right) &= -q_i \frac{\nabla_r \left(\eta_{r,i}(\mathbf{r}) \right)}{\eta_{r,i}(\mathbf{r})^2} = q_i \frac{\mathbf{n}_{CO,i}}{\eta_{r,i}(\mathbf{r})^2} \end{aligned} \tag{4.6}$$

where $\mathbf{n}_{CG} = \frac{\mathbf{r}_{goal} - \mathbf{r}}{\|\mathbf{r}_{goal} - \mathbf{r}\|}$ and $\mathbf{n}_{CO,i} = \frac{\mathbf{r}_{obs,i} - \mathbf{r}}{\|\mathbf{r}_{obs,i} - \mathbf{r}\|}$ are the unit vectors pointing from the Chaser towards the goal and the i^{th}-obstacle respectively.

The value of q_i is selected to place the unstable equilibrium point of the field on the i^{th}-obstacle safety sphere boundary side opposite to the goal point. In this way, the gradient lines will only cross the sphere boundary from inside to outside. This sphere is characterised by a radius $R_i = R_{s,i} + R_c$ which is the sum of the actual safety radius $R_{s,i}$ of the i^{th}-obstacle and the radius of the volumetric sphere containing the Chaser R_c. This formulation allows to take into account also the Chaser physical dimensions. The analysis is simplified as a 1D case, i.e. only variations in the magnitude of the radial distance r from the goal point are taken into account (assumption feasible for function with spherical symmetry), and the origin is placed in r_{goal}. Identifying with D_i the 1D distance between the i_{th} obstacle and the goal:

$$r_{goal} = 0, \quad r_{obs} = D_i, \quad r_{eq,i} = R_i + D_i.$$

where $r_{eq,i}$ is the point in which the unstable equilibrium point of the i^{th} obstacle is desired. Thus, q_i can be obtained setting the sum of attractive and repulsive gradients as equal to zero in $r_{eq,i}$.

$$\begin{aligned}
&-\frac{n_{CG}}{\eta_a(r_{eq,i})^2}+q_i\frac{n_{CO,i}}{\eta_{r,i}(r_{eq,i})^2}=0\\
&\frac{0-(R_i+D_i)}{(R_i+D_i)^3}=q_i\frac{D_i-(R_i+D_i)}{R_i^3}\quad\rightarrow\quad q_i=\frac{R_i^2}{(R_i+D_i)^2}
\end{aligned}\tag{4.7}$$

This method is known as the *equilibrium point placement method*, [26]. For sake of visibility, only the gradient lines of the field belonging to the X-Y plane are shown in Fig. 4.6.

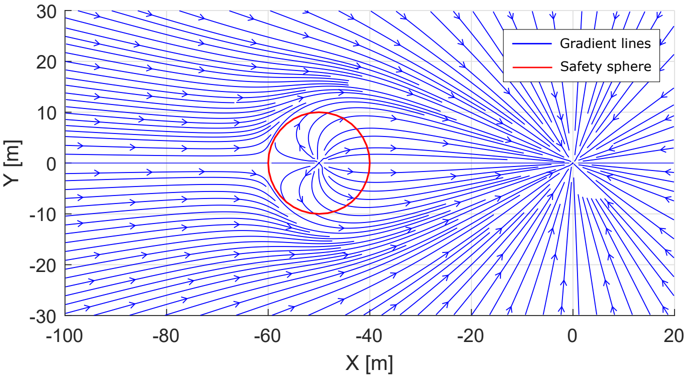

Figure 4.6: Gradient lines of Harmonic APF, showing how the obstacle safety sphere is never crossed from outside to inside.

Lastly, the desired velocity is computed as

$$\mathbf{v}_{des}=-\frac{\nabla_r\left(U(\mathbf{r})\right)}{\|\nabla_r\left(U(\mathbf{r})\right)\|}v_{mod}\tag{4.8}$$

where v_{mod} is the desired velocity modulus which should increase with the distance from the goal and becomes zero when the goal is reached.

4.4.1 Adaptation for moving obstacles

The formulation just presented takes into account both the physical dimensions of the Chaser and of multiple fixed obstacles. In case of moving obstacles, instead, the relative velocity between the Chaser and the obstacle should be considered and included in the algorithm. Starting from [15, 16], instead of a static radius, a dynamic radius is considered in the definition of the repulsive gain q_i.

$$R_{dyn,i}(\mathbf{r},\mathbf{v})=\overbrace{R_{s,i}+R_c}^{R_i}+\frac{v_{R,i}(\mathbf{r},\mathbf{v})^2}{2\varepsilon a_{max}}\tag{4.9}$$

where $\mathbf{v},\mathbf{v}_{obs,i}$ are the velocity of the Chaser and the i^{th}-obstacle respectively, $v_{R,i}(\mathbf{r},\mathbf{v})=(\mathbf{v}-\mathbf{v}_{obs,i})^T\,\mathbf{n}_{CO,i}$ is the component of the relative velocity of the Chaser w.r.t. the i^{th}-obstacle along the unit vector $\mathbf{n}_{CO,i}$, ε is a safety factor which should be chosen as close as

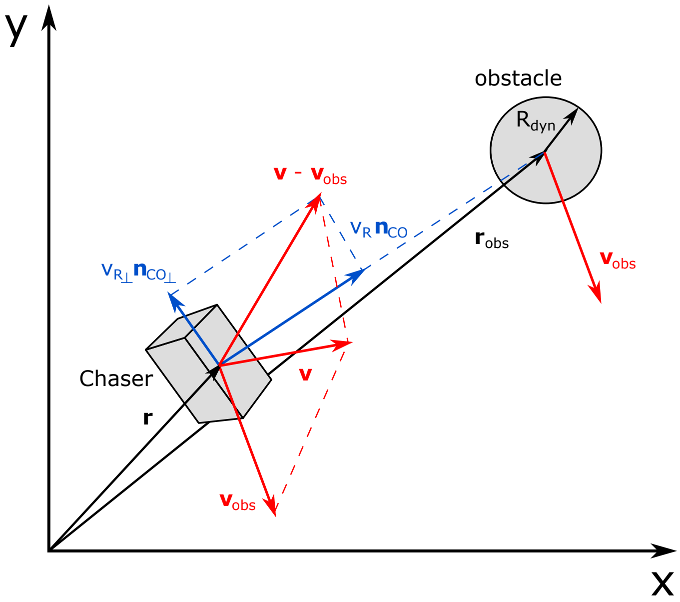

Figure 4.7: Relations among the velocity vectors.

possible to 1, and $a_{max} = \frac{F_{max}}{\sqrt{2m_c}}$ is the maximum control acceleration with F_{max} being the maximum force provided by the actuation system. It must be noted that the last term of $R_{dyn,i}$ is exactly the space required to stop the motion characterised by the velocity $v_{R,i}$ applying the constant deceleration a_{max}.

In this case, the repulsive field gradient must be calculated with respect to both position and velocity. Considering $\varepsilon = 1$, the repulsive gradient w.r.t. position is calculated as follows:

$$\nabla_r\left(U_{r,i}(\mathbf{r},\mathbf{v})\right) = -q_i(\mathbf{r},\mathbf{v})\frac{\nabla_r\left(\eta_{r,i}(\mathbf{r})\right)}{\eta_{r,i}(\mathbf{r})^2} + \nabla_r\left(q_i(\mathbf{r},\mathbf{v})\right)\left(\frac{1}{\eta_{r,i}(\mathbf{r})} - \frac{1}{\eta_0}\right) \tag{4.10}$$

The first half of the right term has already been obtained in Eq. 4.6. The term $\nabla_r\left(q_i(\mathbf{r},\mathbf{v})\right)$, instead, is calculated as:

$$\begin{aligned}\nabla_r\left(q_i(\mathbf{r},\mathbf{v})\right) &= 2\ \frac{R_{dyn,i}(\mathbf{r},\mathbf{v})}{R_{dyn,i}(\mathbf{r},\mathbf{v})+D_i}\nabla_r\left(\frac{R_{dyn,i}(\mathbf{r},\mathbf{v})}{R_{dyn,i}(\mathbf{r},\mathbf{v})+D_i}\right) = \\ &= 2\ \frac{D_i\ R_{dyn,i}(\mathbf{r},\mathbf{v})}{\left(R_{dyn,i}(\mathbf{r},\mathbf{v})+D_i\right)^3}\nabla_r\left(R_{dyn,i}(\mathbf{r},\mathbf{v})\right) = \\ &= 2\ \frac{D_i\ R_{dyn,i}(\mathbf{r},\mathbf{v})}{\left(R_{dyn,i}(\mathbf{r},\mathbf{v})+D_i\right)^3}\frac{v_{R,i}(\mathbf{r},\mathbf{v})}{a_{max}}\nabla_r\left(v_{R,i}(\mathbf{r},\mathbf{v})\right)\end{aligned} \tag{4.11}$$

Now, referring to Fig. 4.7 and considering that $v_{R,i} = \left(\mathbf{v} - \mathbf{v}_{obs,i}\right)^T \mathbf{n}_{CO,i}$, its gradient with respect to the position is [16]

$$\nabla_r\left(v_{R,i}(\mathbf{r},\mathbf{v})\right) = -\frac{v_{R_\perp,i}(\mathbf{r},\mathbf{v})\ \mathbf{n}_{CO_\perp,i}}{\eta_{r,i}(\mathbf{r})} \tag{4.12}$$

where $v_{R_\perp,i}\ \mathbf{n}_{CO_\perp,i}$ is the component of the Chaser relative velocity w.r.t. the i^{th}-obstacle perpendicular to the unit vector $\mathbf{n}_{CO_i}$.
Therefore, the total repulsive gradient w.r.t. position of the field is obtained substituting Eq. 4.11 and 4.12 in Eq. 4.10.

$$\begin{aligned}\nabla_r\left(U_{r,i}(\mathbf{r},\mathbf{v})\right) = & \overbrace{q_i(\mathbf{r},\mathbf{v})\frac{\mathbf{n}_{CO,i}}{\eta_{r,i}(\mathbf{r})^2}}^{\nabla_r(U_{r,i})_{fixed}} + \\ & \underbrace{-2\ \frac{D_i\ R_{dyn,i}(\mathbf{r},\mathbf{v})}{\left(R_{dyn,i}(\mathbf{r},\mathbf{v})+D_i\right)^3}\frac{v_{R,i}(\mathbf{r},\mathbf{v})}{a_{max}}\left(\frac{1}{\eta_{r,i}(\mathbf{r})}-\frac{1}{\eta_0}\right)\frac{v_{R_\perp,i}(\mathbf{r},\mathbf{v})\ \mathbf{n}_{CO_\perp,i}}{\eta_{r,i}(\mathbf{r})}}_{\nabla_r(U_{r,i})_{mobile}}\end{aligned} \tag{4.13}$$

The repulsive gradient w.r.t. velocity, instead, is given as follows:

$$\nabla_v\left(U_{r,i}(\mathbf{r},\mathbf{v})\right) = \nabla_v\left(q_i(\mathbf{r},\mathbf{v})\right)\left(\frac{1}{\eta_{r,i}(\mathbf{r})}-\frac{1}{\eta_0}\right) \tag{4.14}$$

Following the same step as in Eq. 4.11 it is possible to obtain

$$\nabla_v\left(q_i(\mathbf{r},\mathbf{v})\right) = 2\ \frac{D_i\ R_{dyn,i}(\mathbf{r},\mathbf{v})}{\left(R_{dyn,i}(\mathbf{r},\mathbf{v})+D_i\right)^3}\frac{v_{R,i}(\mathbf{r},\mathbf{v})}{a_{max}}\nabla_v\left(v_{R,i}(\mathbf{r},\mathbf{v})\right) \tag{4.15}$$

Once again, referring to Fig. 4.7 and considering that $v_{R,i} = \left(\mathbf{v}-\mathbf{v}_{obs,i}\right)^T\mathbf{n}_{CO,i}$, its gradient with respect to the velocity is [16]

$$\nabla_v\left(v_{R,i}(\mathbf{r},\mathbf{v})\right) = \mathbf{n}_{CO,i} \tag{4.16}$$

Therefore, the total repulsive gradient w.r.t. velocity of the field is obtained substituting Eq. 4.15 and 4.16 in Eq. 4.14.

$$\nabla_v\left(U_{r,i}(\mathbf{r},\mathbf{v})\right) = 2\ \frac{D_i\ R_{dyn,i}(\mathbf{r},\mathbf{v})}{\left(R_{dyn,i}(\mathbf{r},\mathbf{v})+D_i\right)^3}\frac{v_{R,i}(\mathbf{r},\mathbf{v})}{a_{max}}\left(\frac{1}{\eta_{r,i}(\mathbf{r})}-\frac{1}{\eta_0}\right)\mathbf{n}_{CO,i} \tag{4.17}$$

Observing the new formulation of the repulsive gradient it is possible to understand the effect that this modification causes on the repulsive force:

- $\nabla_v(U_{r,i})$ reinforces $\nabla_r(U_{r,i})_{fixed}$, augmenting the repulsive effect in the $-\mathbf{n}_{CO,i}$ direction;

- $\nabla_r(U_{r,i})_{mobile}$ add a steering effect along $\mathbf{n}_{CO_\perp,i}$ in order to circumnavigate the moving obstacle.

The effect of the gradient terms formulated in Eq. 4.13 and 4.17 is schematised in Fig. 4.8.

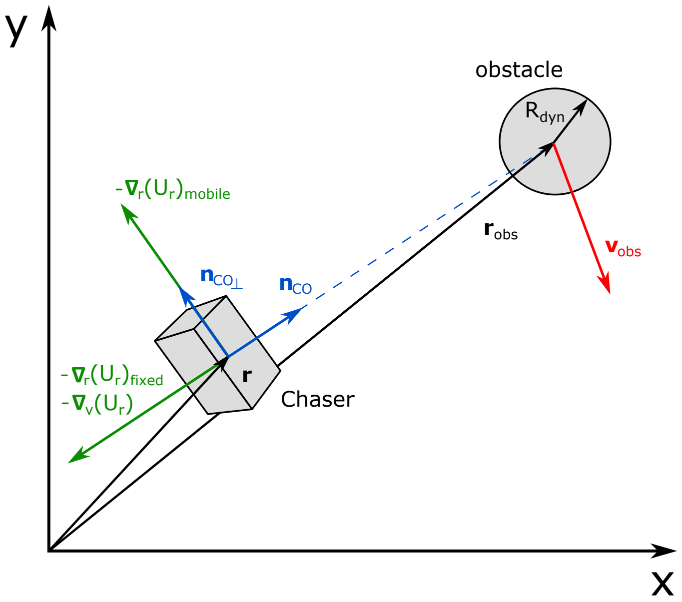

Figure 4.8: Repulsive action in case of moving obstacles.

4.4.2 Adaptation for moving targets

Similarly to the case of moving obstacles, when the target point is moving its velocity should be considered in the algorithm. In [16], for example, an attractive field $U_a(\mathbf{r}, \mathbf{v})$ is built taking into account also the relative velocity of the Chaser w.r.t. the goal. This approach modifies the attractive gradient so that the attractive force has two effects on the Chaser:

- attracts the Chaser towards the present position of the goal point, as it would happen with fixed a goal point;
- forces the Chaser to simultaneously slide in the same direction of the goal point motion, making it chase the target point while getting closer to it.

Although this approach is effective, it makes the attractive field have a dependence on the velocity. It should be desired, instead, to maintain the attractive field as similar as possible to the harmonic formulation of Sec. 4.4, i.e. a function of just the Chaser position. The approach formulated in this work, therefore, exploits the goal point velocity information $\mathbf{v}_{goal}$ only to recalculate v_{mod}, the magnitude of the desired velocity $\mathbf{v}_{des}$.

$$v_{mod}(\mathbf{r}, t) = \|\mathbf{v}_{goal}(t)\| + \Delta v_{plus}\eta_a(\mathbf{r}) \tag{4.18}$$

where Δv_{plus} is the magnitude of the relative velocity of the Chaser w.r.t. the desired goal when $\eta_a(\mathbf{r}) = \|\mathbf{r}_{goal} - \mathbf{r}\| = 1\ m$. In such way, the attractive field attracts the Chaser towards the moving goal present position, but the higher the relative distance is, the faster the spacecraft is w.r.t. the target point. Hence, the Chaser is actually able to reach the goal and, when this happens, relative velocity becomes null.

The algorithm, anyway, must be modified in case both obstacles and moving goal points are considered. Particularly, the attractive gradient modulus must be resized before summing it with the repulsive one when the distance D_i between the goal point and the i^{th}-obstacle is less than $R_{dyn,i}$. Otherwise, since the attractive field tends towards $-\infty$ in the goal point, the Chaser would be guided by the goal point inside the safety sphere of the obstacle. This can be deducted by the gradient lines of Fig. 4.9, where the goal point has been placed inside the object safety sphere. The resizing is executed taking into account only the repulsive gradient with respect to position $\nabla_r\left(U_{r,i}(\mathbf{r},\mathbf{v})\right)$. Hence, the resized attractive gradient is

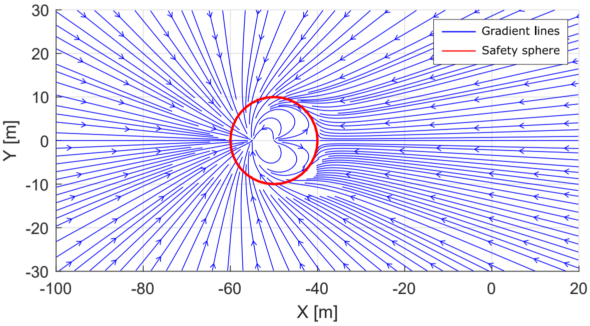

Figure 4.9: Gradient lines of HAPF when $D_i < R_{dyn,i}$.

$$\nabla_r(U_a(\mathbf{r})) = \frac{\nabla_r(U_a(\mathbf{r}))}{\|\nabla_r(U_a(\mathbf{r}))\|}\|\nabla_r(U_{r,i}(\mathbf{r},\mathbf{v}))\|. \tag{4.19}$$

In this way, the resize operation can be executed either when the obstacles should be fixed or moving.

4.5 Pairing with Sliding-Mode Control

As previously mentioned, the APF guidance algorithm output consists of just the desired velocity vector $\mathbf{v}_{des}$, which should be then reproduced selecting a control algorithm. The control choice is fundamental to determine whether or not we will be able to exactly follow the APF gradient lines, i.e. whether or not it will be granted that the obstacles safety spheres are never crossed into.

In this work, the algorithm selected is a first-order Sliding-Mode Controller (SMC), which has already shown its effectiveness in [15, 26]. The main benefits introduced by SMC are its invariance property and the ability to decouple high dimensional problems into subtasks of lower dimensionality. These properties allow true decoupling of the tasks “design of the potential field” and “tracking the gradient”, since the SMC is theoretically able to exactly track any *smooth* artificial vectors field. The sliding surface of the implemented first-order SMC is

$$\begin{aligned} \mathcal{S} = \{\mathbf{v} \ \in \mathbb{R}^3 :\ \sigma(\mathbf{v}) = \mathbf{0}\},\ \textit{where} \\ \sigma(\mathbf{v}) = \mathbf{v} - \mathbf{v}_{des}. \end{aligned} \tag{4.20}$$

The sliding motion onto the surface $\mathcal{S}$ is enforced through the control force

$$\mathbf{F}_{contr} = -F_{max}\,\mathrm{sign}(\sigma(\mathbf{v})) \tag{4.21}$$

which is, in fact, discontinuous with respect to the sliding surface. Note also that the SMC algorithm is extremely useful because it creates a discontinuous behaviour of $\mathbf{F}_{contr}$, which is suitable for thermochemical thrusters characterised by ON/OFF functioning.

Unfortunately, as can be seen from Fig. 4.6, the curvature of APF gradient lines becomes higher and higher the closer the Chaser is to the unstable equilibrium point placed in front of the obstacle. In the saddle point the curvature tends to infinity, inducing a *non-smooth* velocity direction change which can not be exactly tracked by the SMC. This criticality would easily lead to penetrate the obstacle safety sphere, breaking safety requirements. In order to cancel this risk, an approach similar to the one described in Sec. 4.4.1 is adopted even in case of fixed obstacles, [26], since $v_{R,i}$ can be defined even when $\mathbf{v}_{obs_i}$ is null. Particularly:

- the dynamic radius $R_{dyn,i}$ reported in Eq. 4.9, is used to calculate the repulsive gain q_i even in case of fixed obstacles, making it higher than it would normally be considering just the static radius R_i;
- unlike the case of moving obstacles, the repulsive gain q_i is still considered as a constant in the gradient computation, i.e. the repulsive gradient is calculated as in Eq. 4.6.

This method grants safety requirements satisfaction without driving the Chaser too far away from the nominal trajectory, i.e. containing the fuel consumption.

Chapter 5

Chaser configuration

In this chapter, the Chaser satellite considered for the rendezvous and berthing manoeuvre is presented. At the beginning, a description of its geometrical features, considering both the service module and the robotic arm, is provided. Afterwards, position actuators configuration and sensors set are presented, as well as the mathematical models used to simulate their behaviour in the analyses.

5.1 Geometrical and physical features

The baseline of the Chaser s/c consists of a square-base shaped prism, the *service module*, and a 3-links *robotic arm*. Fig. 5.1 reports the geometrical configuration of the s/c with the robotic arm both open and closed.

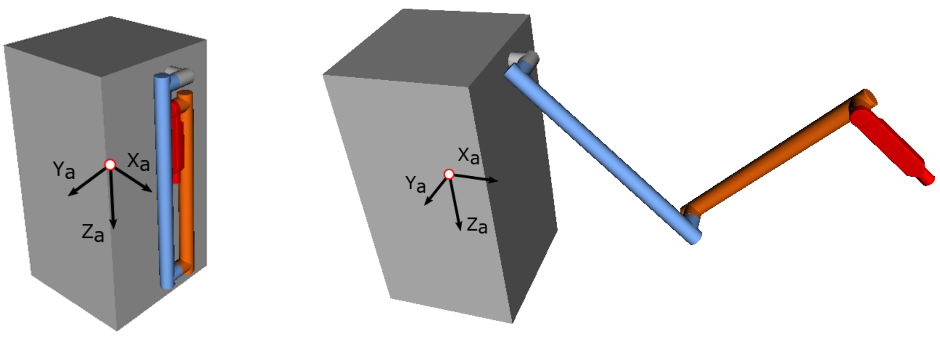

(a) Arm closed **(b)** Arm open

Figure 5.1: Chaser geometrical configuration.

Taking inspiration from similar missions, the prism dimension is supposed to be approximately 1.3 m x 1.3 m x 2.6 m, while the robotic arm, designed in [27], is attached to the lateral face identified by the $+X_a$ unit vector and positioned along its vertical symmetry axis (few centimetres below the top face). The arm is composed by three links jointed together with 2D hinges so that the arm motion is confined to the $X_a - Z_a$ plane. Starting from the one closer to the base, the links are 2 m, 1.75 m, 0.75 m long and weight 35 kg, 30 kg, 5 kg, respectively. Therefore, the total reach distance is more than 4 m, while the total mass of the arm is 70 kg. Further information related to the arm can be found in [27].

The total wet mass of the whole Chaser satellite, thus including robotic arm and fuel, is 1500 kg and, as an assumption, its CoM is considered to be fixed in the geometrical centre of the prismatic service module.

5.2 Thrusters configuration

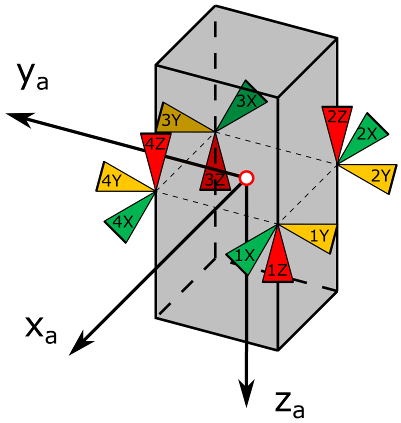

Figure 5.2: Thrusters cluster assumed for the Chaser s/c.

As for position actuators, the Chaser satellite is considered to be equipped with a typical cluster of twelve thermochemical thrusters, characterised by ON/OFF functioning. As shown in Fig. 5.2, the cluster is aligned with the body reference system F_a and the thrusters must be turned on in pair in order to achieve position control without any undesired coupling effect with rotational dynamics. Each of the thermochemical thrusters is characterised by a specific impulse of $I_{sp} = 250$ s and provides $F_{max,single} = 20$ N, which

Table 5.1: Thrusters cluster management.

Force	Thrusters	
+X	2X	3X
−X	1X	4X
+Y	1Y	2Y
−Y	3Y	4Y
+Z	2Z	4Z
−Z	1Z	3Z

means that the maximum force available in any body direction is $F_{max} = 40\ N$. Tab. 5.1 shows how to manage the cluster in order to shoot in any body direction.

The characteristic ON/OFF functioning of thermochemical thrusters is reproduced in simulation through the selection of a discontinuous control law, the first-order SMC presented in Sec. 4.5. The control force is calculated as in Eq. 4.21 with $F_{max} = 40\ N$ accordingly to the equipped thrusters. Neither shooting magnitude and direction errors nor other real effects are considered, since the thesis focuses more on the implementation of sensors simulation models.

5.3 Position sensors set

The Chaser s/c is assumed to be equipped with two different position sensors, an optical camera and an accelerometer.

The optical camera is mounted on the lateral face of the service module where the robotic arm is attached so that, when the body frame F_a is aligned with the LVLH frame F_{LVLH}, the camera is pointing towards the Target. Its output is considered to be the relative position of the Target w.r.t. the camera expressed in the camera geometrical reference system F_{cam}.

The accelerometer, instead, is part of the Inertial Measurement Unit (IMU) and is able to provide acceleration, velocity and position measurements w.r.t. an inertial reference frame. Due to the vicinity of the Chaser to the Target, however, the LVLH frame can be considered *quasi-inertial*. Hence, the accelerometer is supposed to provide directly relative measurements of the aforementioned quantities in the IMU geometrical reference frame F_{IMU}.

5.3.1 Camera simulation model

As previously stated, the optical camera is able to directly measure the relative position of the Target w.r.t. the camera mounted on the Chaser. Fig. 5.3 shows the camera reference system, supposed to be aligned with the Chaser attitude system F_a but translated in the camera lens. In this figure, $\mathbf{r}_{t<cam>}$, $\mathbf{r}_{cam<c>}$, $\mathbf{r}_{t<c>}$ are respectively the position of the Target w.r.t. the camera and the positions of the camera and the Target w.r.t. the Chaser.

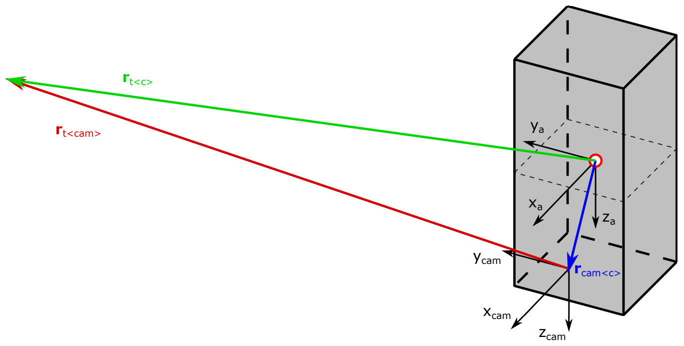

Figure 5.3: Camera reference system.

In order to recreate the camera output, the following simulation model has been adopted.

- **Calculation of $\mathbf{r}^{(cam)}_{t<cam>}$**. Initially, the position of the Target w.r.t. the Chaser expressed in LVLH frame $\mathbf{r}^{(LVLH)}_{t<c>}$ is computed as $-\mathbf{r}^{(LVLH)}_{c<t>}$, i.e. as the opposite vector to the Chaser position w.r.t. the Target obtained through Hill's equation. Then, this vector is transformed into the Chaser attitude frame using L_{a_LVLH}, the rotation matrix already presented in Eq. 2.3. Finally, the vector is translated into the camera reference system F_{cam} without the need of any further rotation.

$$\begin{aligned}
\mathbf{r}^{(LVLH)}_{t<c>} &= -\mathbf{r}^{(LVLH)}_{c<t>} \\
\mathbf{r}^{(a)}_{t<c>} &= L_{a\_LVLH}\mathbf{r}^{(LVLH)}_{t<c>} \\
\mathbf{r}^{(cam)}_{t<cam>} &= \mathbf{r}^{(cam)}_{t<c>} - \mathbf{r}^{(cam)}_{cam<c>} = \mathbf{r}^{(a)}_{t<c>} - \mathbf{r}^{(a)}_{cam<c>}
\end{aligned} \tag{5.1}$$

- **Noise addition**. The actual quantity measured by the camera, $\mathbf{r}^{(cam)}_{t<cam>}$, is corrupted adding 100 Hz band-limited white noise to the signal. The amplitude of the noise has been selected as 1% of the range from the Target, resulting in a conservatory approximation accordingly to Fig. 5.4.

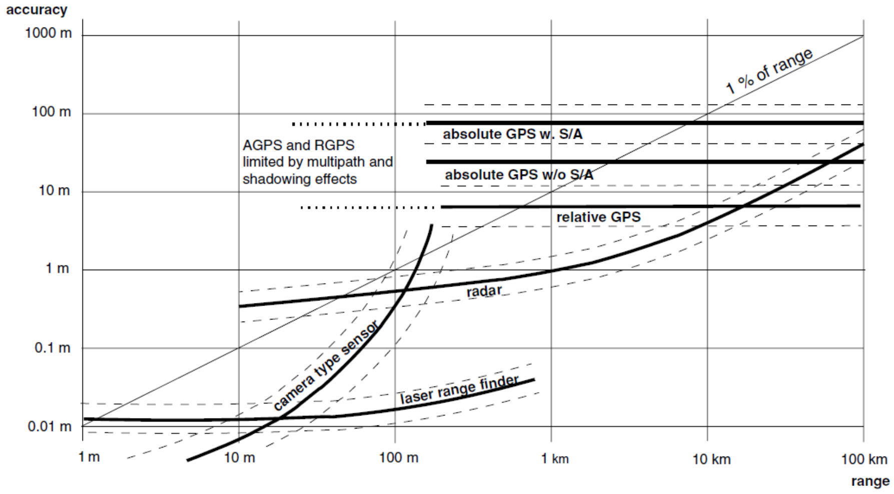

Figure 5.4: Typical accuracy of rendezvous position sensors, [9].

- **Low pass filtering**. In order to slightly reduce measurement noise before providing the Navigation algorithm with the camera output, the measured position is filtered using a low pass filter with time constant $\tau = 0.05\ s$.
- **Transformation into LVLH frame**. Since the position measurements will be used as input for the Navigation algorithm, built using Hill's equation, the signal must be transformed back into $\mathbf{r}^{(LVLH)}_{c<t>}$, inversely following the steps of Eq. 5.1.

The camera simulation block runs at 10 Hz, except for the noise generation block which, as previously stated, is characterised by a frequency of 100 Hz.

5.3.2 Accelerometer simulation model

The accelerometer is able to measure the acceleration acting on the Chaser w.r.t. an inertial reference frame. Approximating F_{LVLH} as a quasi-inertial reference system, this measurement can be directly considered as the relative acceleration of the Chaser w.r.t. the Target. The components of the acceleration are measured in F_{IMU} which, although not aligned to F_a, is supposed to be centred in the Chaser CoM.

In order to recreate the accelerometer output, the following simulation steps have been followed.

- **Calculation of $\mathbf{a}_{c<t>}^{(IMU)}$**. The acceleration derived from Hill's equations $\mathbf{a}_{c<t>}^{(LVLH)}$ is firstly transformed into the Chaser attitude reference frame F_a using the rotation matrix L_{a_LVLH} already used for the camera. Afterwards, the vector is further transported into the F_{IMU} geometrical reference system with the matrix L_{IMU_a} built using the IMU rotation angles w.r.t. the attitude reference frame ϕ_{IMU}, θ_{IMU}, ψ_{IMU}.

$$\mathbf{a}_{c<t>}^{(IMU)} = L_{IMU\_a}\mathbf{a}_{c<t>}^{(a)} = L_{IMU\_a}\ L_{a\_LVLH}\mathbf{a}_{c<t>}^{(LVLH)} \tag{5.2}$$

- **Noise addition**. The acceleration measured by the sensor is corrupted adding a 100 Hz band-limited white noise with amplitude of 3 $mg \simeq 0.03\ m/s^2$ (with $g = 9.81\ m/s^2$). The amplitude of the noise has been selected following the example of commercial components datasheets (bias minor than 4 mg).

- **Low pass filtering**. In order to slightly reduce measurement noise before providing the Navigation algorithm with the accelerometer outputs, the measured acceleration is filtered using a low pass filter with time constant $\tau = 0.02\ s$.

- **Double integration**. The corrupted acceleration signal is integrated twice to obtain the estimate of both the relative velocity and position, respectively $\mathbf{v}_{c<t>}^{(IMU)}, \mathbf{r}_{c<t>}^{(IMU)}$. The position initial condition is taken from the camera output, while the velocity initial condition is set to zero. None of the integrator is reset over time, hence the velocity and position estimates obtained are characterised by a drift motion.

- **Transformation into LVLH frame**. Once again, since the accelerometer measurements will be used as input for the Navigation algorithm, the output signals must be transformed back into $\mathbf{a}_{c<t>}^{(LVLH)}, \mathbf{v}_{c<t>}^{(LVLH)}, \mathbf{r}_{c<t>}^{(LVLH)}$, inversely following the steps of Eq. 5.2.

The accelerometer simulation block runs at 100 Hz.

Chapter 6

Simulation results

In this final chapter the simulation results will be presented. At first, the simulated scenarios are presented and discussed. Afterwards, the simulator is analysed, focusing on each component of the simulator itself and applying the algorithms presented in Chap. 3 and 4 to the actual system. Finally, the results obtained through different simulations are reported, focusing particularly on the effect that the obstacle avoidance strategy has on the geometrical path followed by the Chaser and the propellant consumption.

6.1 Simulated scenarios

As already stated, the simulated scenario consists of the closing and final approach phases of a rendezvous and berthing manoeuvre executed by the Chaser s/c presented in Chap. 5. The mass of the Chaser has been considered as constant, under the assumption that the propellant mass consumed m_p will be negligible in comparison to the total mass of the Chaser m_c. The Target of the manoeuvre is orbiting on a circular 400 km-height orbit. The manoeuvre is executed exploiting the GNC system designed in the previous chapters, i.e. by the combination of Sliding-Mode Observer, Artificial Potential Field and Sliding-Mode Control.

The whole manoeuvre is studied in the Target $LVLH$ frame using Hill's equations presented in Chap. 2 and the Chaser attitude reference frame F_a is considered to be constantly aligned with F_{LVLH}. The closing phase, starting from about -500 m and ending at -100 m on V_{bar}, consists of two consecutive radial boosts, preferred over other kind of manoeuvres for the safety aspects discussed in Sec. 2.6. The final approach consists of a straight line towards the Target starting from about -100 m on V_{bar} and ending 4 m behind the Target. The velocity during this approach should be decreased gradually in order to achieve the final position without any residual velocity. Finally, the capacity of the Chaser to maintain the desired final position while moving the robotic arm is analysed, too. Only disturbance forces produced by the robotic arm are taken into account, since the focus of the thesis is on position control, and the Chaser attitude frame F_a remains aligned with the LVLH frame F_{LVLH}.

Starting from this nominal manoeuvre, three different scenarios have been simulated, varying the number and the characteristics of the obstacles encountered:

1. No obstacles are considered during the closing phase, while, in the final approach, four fixed obstacles are located at $x = -50\ m$ and $y = \pm 7.5\ m$, two of them placed at $z = 10\ m$, the others at $z = -5\ m$. These obstacles are characterised by an ellipsoidal shape (physical semi-axes $a_x = 5\ m,\ b_y = 2.5\ m,\ c_z = 2.5\ m$) and by a safety radius $R_s = 5\ m$. Note that this group of obstacles is selected since it would cause a local minimum point in case of classic APF algorithm.

2. The Chaser encounters two obstacles during the closing phase, the first one moving with constant speed near the end of the first radial boost and the second fixed in the middle of the second manoeuvre. These obstacles have the same physical shape of the ones described in the previous scenario but are characterised by $R_s = 10\ m$. The final approach, instead, remains equal to the previous scenario. The aim of this scenario is to demonstrate the ability of the GNC system to handle moving obstacles.

3. The obstacles encountered by the Chaser are exactly the same as the ones characterising the second scenario. The only difference consists of the safety radius characterising the obstacles met during the closing phase, set to $R_s = 20\ m$. This third scenario allows to deduce the impact that the obstacle avoidance strategy cause on the propellant consumption.

Fig. 6.1 reports the schematic concept of the rendezvous manoeuvre described. The nominal trajectory is drawn using a continuous line, while the dashed line identifies the trajectory modified by the presence of obstacles.

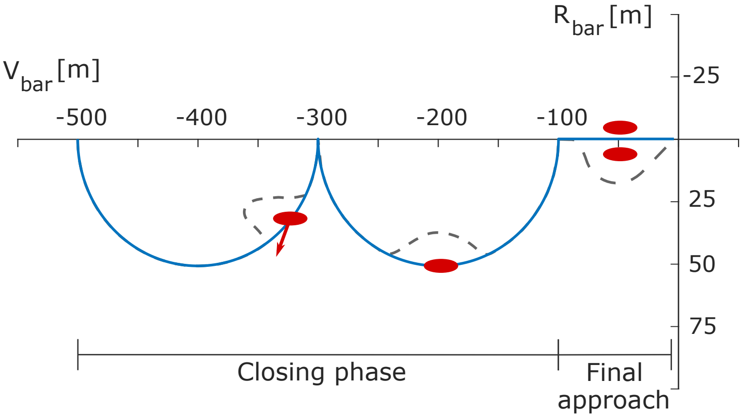

Figure 6.1: Schematic representation of simulated scenarios with obstacles in red.

Finally, Tab. 6.1 and 6.2 summarise the information provided in this section. Note that the initial and final conditions of the manoeuvres reported in the second table characterise the nominal rendezvous manoeuvre, i.e. the manoeuvre that the GNC system will try to recreate.

Table 6.1: Chaser, Target and obstacles features.

Parameter	**Symbol**	**Value**
Mass of the Chaser (constant)	m_c	$1500\ kg$
Orbit height of the Target	h_T	$400\ km$
Starting position of obstacle 1	$r_{obs1,0}$	$[-300;\ 100;\ 100]\ m$
Velocity of obstacle 1	$v_{obs1,0}$	$[-0.02;\ -0.05;\ -0.03]\ m/s$
Position of obstacle 2 (fixed)	r_{obs2}	$[-200;\ 0;\ 53]\ m$
Position of obstacle 3 (fixed)	r_{obs3}	$[-50;\ 7.5;\ -5]\ m$
Position of obstacle 4 (fixed)	r_{obs4}	$[-50;\ 7.5;\ 10]\ m$
Position of obstacle 5 (fixed)	r_{obs5}	$[-50;\ -7.5;\ -5]\ m$
Position of obstacle 6 (fixed)	r_{obs6}	$[-50;\ -7.5;\ 10]\ m$
Safety radius of obstacles 1,2 (scenario 2)	$R_{s,1/2}$	$10\ m$
Safety radius of obstacles 1,2 (scenario 3)	$R_{s,1/2}$	$20\ m$
Safety radius of obstacles 3,4,5,6	$R_{s,3/4/5/6}$	$5\ m$
Physical dimension of obstacles (semi-axes)	a_x, b_y, c_z	$[5;\ 2.5;\ 2.5]\ m$

Table 6.2: Rendezvous manoeuvres nominal features.

Manoeuvre	**Initial nominal conditions**	**Final nominal conditions**
Radial boost 1	$r_{RB1,0} = [-500; 0; 0]\ m$ $v_{RB1,0} = [0; 0; 0]\ m/s$	$r_{RB1,f} = [-300; 0; 0]\ m$ $v_{RB1,f} = [0; 0; 0]\ m/s$
Radial boost 2	$r_{RB2,0} = [-300; 0; 0]\ m$ $v_{RB2,0} = [0; 0; 0]\ m/s$	$r_{RB2,f} = [-100; 0; 0]\ m$ $v_{RB2,f} = [0; 0; 0]\ m/s$
Final approach straight line	$r_{FA,0} = [-100; 0; 0]\ m$ $v_{FA,0} = [0.5; 0; 0]\ m/s$	$r_{FA,f} = [-4; 0; 0]\ m$ $v_{FA,f} = [0; 0; 0]\ m/s$

6.2 Simulator

The simulator designed in this thesis work is a 3-Degree of Freedom (DoF) simulator which recreates only the translational dynamics of the Chaser since, as mentioned before, the Chaser attitude frame F_a is considered to be constantly aligned with the LVLH frame F_{LVLH}. The simulator is built in the MATLAB&Simulink environment and composed following the scheme reported in Fig. 6.2. Each block of the figure will be deeply discussed in the following sections except for the "Robotic arm disturbances" block which, when the Chaser reaches the final position desired, will simply act as the source of the perturbation forces introduced by the movimentation of the robotic arms (sampled with a frequency of $100\ Hz$). These forces are directly provided by [27] and are not calculated in this thesis work.

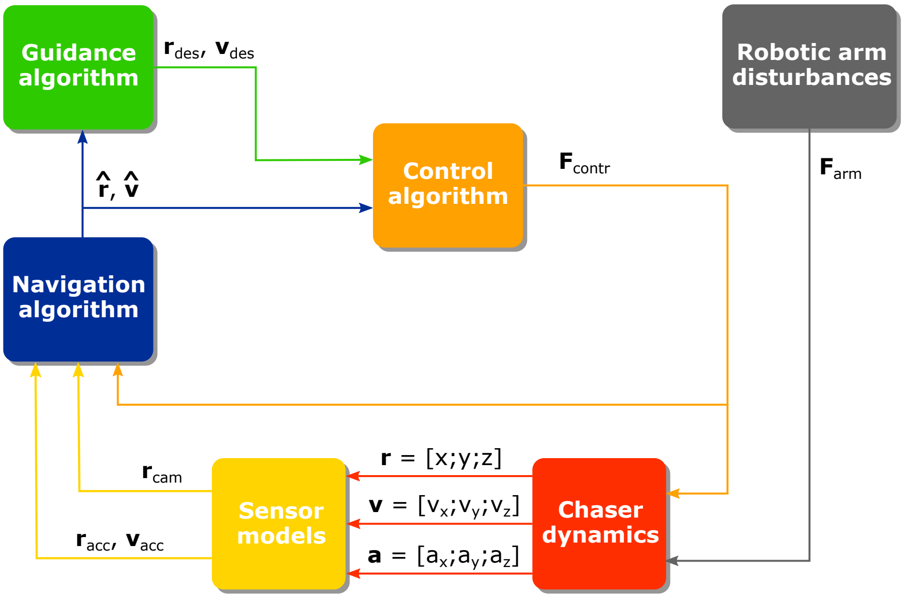

Figure 6.2: Schematic representation of the block composing the orbital.

The solver adopted for the simulation is *ode4 (Runge-Kutta)*, a fixed-time step integrator solver, and the time step is set at 0.01 s.

6.2.1 Chaser dynamics block

The "Chaser dynamics" block models the translational dynamics of the Chaser using Hill's equation (Eq. 2.4) and assuming a constant mass. In order to simulate eventual errors caused by previous manoeuvres, the initial conditions of the Chaser are set as different from the nominal starting condition of the first radial boost expressed in Tab. 6.2. Particularly:

$$\mathbf{r}(0) = [-520;\ 20;\ 10]\ \ m, \quad \mathbf{v}(0) = \left[\frac{3}{2}\,\omega_{\odot} z;\ 0;\ 0\right]\ \ m/s \tag{6.1}$$

The plant dynamics input is represented by the both the control and perturbation forces acting on the Chaser, while the output of the block consists of the Chaser position, velocity and acceleration w.r.t. the Target expressed in F_{LVLH}.

The update frequency of the block is 100 Hz.

6.2.2 Sensors models block

The "Sensors models" block contains the models of both the camera and the accelerometer described in Sec. 5.3. Starting from the exact value of the Chaser position, velocity and acceleration w.r.t. the Target, it provides the measurements of relative position and velocity corrupted by the instrument noise and, in case of the accelerometer, the drift. All these measurements are already expressed in F_{LVLH}.

As mentioned in Sec. 5.3, the camera model runs at 10 Hz, while the accelerometer at 100 Hz.

6.2.3 Navigation algorithm block

The “Navigation algorithm” block contains both the SMOs presented in Sec. 3.4.1 and 3.4.2 for comparison sake, even though only the robust version will be actually used to provide Guidance and Control algorithms with the state vector estimate. Both the algorithms are characterised by an update frequency of 100 Hz.

The classic SMO block inputs consist of the relative position measurement coming from the optical camera $\mathbf{r}_{cam}$ and half the information relative to the control force vector $\frac{1}{2}\mathbf{F}_{contr}$. Similarly to the case of example provided in Sec. 3.4.3, this will allow to understand the ability of the algorithm to provide state estimates even in case of partial knowledge of system dynamics, simulating the action of a 20 N-unknown input. Note that the robotic arm perturbation force $\mathbf{F}_{arm}$ is considered as an unknown input, too. The parameters ρ and L of the algorithm are selected as:

$$\rho = 2, \qquad L = \begin{bmatrix} -0.0050 & 0 & 0.0025 \\ 0 & -0.0050 & 0 \\ -0.0025 & 0 & -0.0050 \end{bmatrix} \tag{6.2}$$

The output of the block consists of the Chaser position and velocity estimates $\hat{\mathbf{r}}_{classic}$, $\hat{\mathbf{v}}_{classic}$, used only for comparison sake.

As for the robust SMO, its inputs consist not only of the signals used as input for the classic SMO, but also of the measurement of relative position and velocity provided by the accelerometer $\mathbf{r}_{acc}$, $\mathbf{v}_{acc}$. As in the previous case, half of the control forces vector and the entire robotic arm perturbation forces vector are considered as unknown inputs acting on the Chaser. The parameters characterising the algorithm will be discussed in the following paragraph related to the data fusion method adopted to use both camera and accelerometer measurements. The output of the block consists of the Chaser position and velocity estimates $\hat{\mathbf{r}}$, $\hat{\mathbf{v}}$ and represents also the output of the entire “Navigation algorithm” block.

Both the SMOs are initialised with the nominal initial conditions of the first radial boost:

$$\hat{\mathbf{r}}(0) = [-500;\ 0;\ 0]\ \ m, \quad \hat{\mathbf{v}}(0) = [0;\ 0;\ 0]\ \ m/s \tag{6.3}$$

Data fusion

As previously stated, in the case of robust SMO, both the measurements provided by the optical camera and by the accelerometer are necessary. This is caused by the particular form that characterises the matrix B in the case of Hill’s Equation. For sake of simplicity, let us consider just the y-motion, which is decoupled from the other directions dynamics. In this case, the state vector is composed by y and $\dot{y}$, while the input matrix is $B_Y = \left[0;\ \frac{1}{m_c}\right]$ $(n = 2,\ m = 1)$. Suppose to possess just the relative position measurement, i.e. $C_Y = [1\ 0]$ and $p = 1$. It is possible to apply the structural constraint of the algorithm expressed in Eq. 3.21 and try to find the symmetric positive definite matrix P and the $m \times p$ matrix F.

$$PB_Y = (FC_Y)^T \quad \rightarrow \quad \begin{bmatrix} P_{11} & P_{12} \\ P_{12} & P_{22} \end{bmatrix} \begin{bmatrix} 0 \\ \frac{1}{m_c} \end{bmatrix} = \begin{bmatrix} 1 \\ 0 \end{bmatrix} F \tag{6.4}$$

In order to satisfy the structural constraint, the matrix P should have the following structure

$$P = \begin{bmatrix} P_{11} & Fm_c \\ Fm_c & 0 \end{bmatrix}$$

where, P_{11} and F can be freely chosen. A matrix with this structure, however, will never be positive definite. Hence it is impossible to satisfy the structural constraint unless possessing also the velocity information as input, i.e. $C_Y = \text{eye}(2)$ and $p = 2$.

Analogously, considering all three dimensions, it is necessary to have $C = \text{eye}(6)$. The position noisy measurement is provided by the optical camera, but the velocity measured by the accelerometer is both noisy and drifted. To eliminate the drift, the robust SMO position estimate is exploited to perform the data fusion process showed in Fig. 6.3. The estimate of the position drift is obtained subracting $\hat{\mathbf{r}}$ from $\mathbf{r}_{acc}$, then it's derivative is calculated over a time span of 20 s to achieve higher accuracy in the estimate of $\mathbf{v}_{drift}$. Lastly, the estimate of the velocity drift is subtracted from the drifted $\mathbf{v}_{acc}$ to provide the algorithm with the corrected velocity measurement. The system observed by the robust first-order SMO is, therefore, characterised by $p = n = 6$, $m = 3$ and the algorithm parameters are selected as:

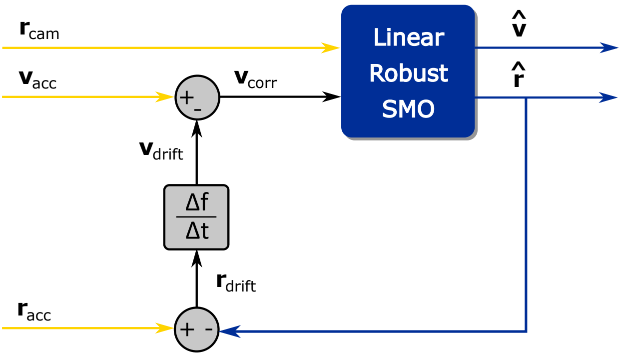

Figure 6.3: Data fusion method adopted to eliminate the drift in accelerometer measurements.

$$\begin{aligned} \rho &= 22, \quad G_l = \text{diag}([0.5,\ 0.5,\ 0.5,\ 0.005,\ 0.005,\ 0.005]), \\ F &= [0_{3\times3}\ \ 0.5\,\text{eye}(3)]\,, \quad P = \text{diag}([5,\ 5,\ 5,\ 0.5m_c,\ 0.5m_c,\ 0.5m_c]) \end{aligned} \tag{6.5}$$

which satisfy all the conditions expressed in 3.4.2.

6.2.4 Guidance and Control block

The “Guidance algorithm” and the "Control algorithm" blocks are executed at 10 Hz and, since the algorithms used slightly vary from the closing to the final approach phase, contain an *if* block which select the correct algorithm to use depending on the rendezvous manoeuvre phase. The shift from one phase to the other happens when the Chaser reaches $x = -101\ m$, one metre before the end of the nominal closing phase, in order to contemplate a small eventual error in the manoeuvre execution.

Guidance strategies for closing phase

During the closing phase, the algorithm adopted is the harmonic APF with adaptations for both moving obstacles and moving goal points described in Sec. 4.4.1 and 4.4.2, paired with the SMC as in Sec. 4.5 ($F_{max} = 40\ N$ accordingly to the onboard thrusters cluster). In this phase, in fact, the goal point must move in order to recreate the closing manoeuvres and its position and velocity evolution over time coincide with the *a priori* computed dynamic evolution of the nominal radial boosts. The manoeuvre reproduction with an APF method, anyway, permits to maintain an high level of safety and perform obstacle avoidance. The parameters of the HAPF algorithm are calculated as:

- a_{max}: computed using the Chaser mass $m_c = 1500\ kg$ and the modulus of the thrust provided by thrusters $F_{max} = 40\ N$;
- q_i: computed, instant by instant, calculating the current distance between the goal point and the i^{th}-obstacle physical point closer to the Chaser, D_i, and the current value of the dynamic radius, $R_{dyn,i}$ ($R_{s,i} = 10 - 20\ m$ depending on the scenario, $R_c = 2\ m$ to include the physical dimensions of the Chaser and $\varepsilon = 1$);
- η_0: supposed equal to 100 m;
- v_{mod}: calculated as in Eq. 4.18 with $\Delta v_{plus} = 0.005\ m/s$.

In order to reduce the propellant consumption, furthermore, the SMC is active only when the delta between the modulus of the desired velocity v_{mod} and the estimate of the actual velocity modulus $\hat{v}$ is greater than 0.03 m/s.

For sake of comparison, anyway, the radial boosts have been firstly reproduced without the use of APF methods. In this case, there is no Guidance algorithm actually working and the desired position and velocity provided to the Control block are directly taken from the *a priori* computed trajectory characterising the closing radial boosts. The Sliding-Mode Control algorithm adopted in this case is slightly different from the one used previously, since the sliding variable σ is defined component-wise as

$$\sigma_i(\hat{r}_i, \hat{v}_i) = (\hat{v}_i - v_{des,i}) + 0.03(\hat{r}_i - r_{des,i}), \qquad i = 1,2,3 \tag{6.6}$$

accordingly to the general case of SMC presented in Sec. 3.3. The control force is calculated as usual as $\mathbf{F}_{contr} = -F_{max}\,\mathrm{sign}\,(\sigma(\hat{\mathbf{r}}, \hat{\mathbf{v}}))$, with $F_{max} = 40\ N$. As in the previous case, the action of the controller is set to be discontinuous in order to save propellant. In this case, however, the SMC is activated component-wise:

- First RB: the control forces acting in the $V_{bar} - R_{bar}$ plane, $F_{contr,X-Z}$, and the one acting in the H_{bar} direction, $F_{contr,Y}$, are shut down respectively when $\|[\hat{x}; \hat{z}] - [x_{des}; z_{des}]\| \leq \Delta s_{X-Z}$ and $|\hat{y} - y_{des}| \leq \Delta s_Y$. Δs_{X-Z} is the safety corridor width in the $V_{bar} - R_{bar}$ plane and starts as 30 m at $t = 0\ s$, then decreases with a parabolic trend to 0 m in 600 s, while afterwards is set to 2 m. Analogously, Δs_Y is the safety corridor width in the H_{bar} direction and starts as 20 m at $t = 0\ s$, then is decreased with a parabolic trend to 0 m in 600 s, while afterwards is set as 10 m;
- Second RB: the control forces acting in the $V_{bar} - R_{bar}$ plane, $F_{contr,X-Z}$, are forced to zero when $\|[\hat{x}; \hat{z}] - [x_{des}; z_{des}]\| \leq 1\ m$. Analogously, the control force acting in the H_{bar} direction, $F_{contr,Y}$, is shut down when $|\hat{y} - y_{des}| \leq 10\ m$.

Obviously this kind of approach is suitable just for the first scenario described in Sec. 6.1, which does not consider any obstacle during the closing phase.

Guidance strategies for final approach

In the final approach, the algorithm used is the harmonic APF algorithm presented in the previous paragraph, but this time the goal point of the field is considered to be fixed. Particularly, the goal point is located at the nominal end of the final approach, i.e. $\mathbf{r}_{goal} = [-4; 0; 0]\ m$. In such way, in absence of obstacles, the Chaser would reach the final desired position performing a forced straight line. The parameters of the algorithm are selected and computed as in the previous paragraph, even though the safety radius of the obstacles is considered to be $R_{s,i} = 5\ m$, while the desired velocity modulus is calculated as

$$v_{mod}(\hat{x}) = \frac{0.5}{x_{goal} - 100} |x_{goal} - \hat{x}|. \tag{6.7}$$

This cause the relative velocity of the Chaser to be $0.5\ m/s$ at $x = -100\ m$ and then decrease linearly until the goal is reached with zero relative velocity.

The Guidance algorithm is once again paired with the SMC described in Sec. 4.5 ($F_{max} = 40\ N$), forced to act discontinuously in order to save propellant. Since the algorithm will be used both for the final approach and the final position station-keeping, the criteria for the control shut down depend on the Chaser position along the V_{bar} axis.

- if $x \leq -4.2\ m$ the SMC is deactivated when $\|\hat{\mathbf{v}} - \mathbf{v}_{des}\| \leq 0.005\ m/s$;
- if $x > -4.2\ m$ the SMC is activated component wise so that the control forces acting in the $V_{bar} - R_{bar}$ plane, $F_{contr,X-Z}$, are forced to zero when $\|[\hat{v}_x; \hat{v}_z] - [v_{des,x}; v_{des,z}]\| \leq 0.003\ m/s$. Analogously, the control force acting in the H_{bar} direction, $F_{contr,Y}$, is shut down when $|\hat{v}_y - v_{des,y}| \leq 0.003\ m/s$.

These criteria permit to achieve higher level of accuracy in the final position station-keeping while maintaining the fuel consumption restrained.

6.3 Simulation results

In the present section, simulation results regarding the first two scenarios presented in Sec. 6.1 are reported. The results relative to the third scenario are reported in Appendix A, due to their similarity to the results of the second scenario. The results are divided in the phases characterising the manoeuvres:

- **Closing phase**: from $t = 0\ s$ to around $t = 2T = 5536\ s$, with T being the Target orbital period and from around $x = -500\ m$ to around $x = -100\ m$;
- **Final approach**: from around $t = 2T = 5536\ s$ to $t = 7000\ s$ and from around $x = -100\ m$ to $x = -4\ m$;
- **Final position station-keeping**: from $t = 7000\ s$ to $t = 7100\ s$.

6.3.1 Closing phase

Scenario 1

In the first scenario, the Chaser performs the radial boosts characterising the closing phase in absence of obstacles. The manoeuvre is firstly executed using only the discontinuous action of SMC, as described in Sec. 6.2.4. Fig. 6.4 reports the Chaser position evolution in the $V_{bar} - R_{bar}$ and $V_{bar} - H_{bar}$ planes, as well as the position estimates provided by both the SMOs. It can be clearly seen how both the observers are able to correctly track the Chaser trajectory, even though starting from the initial position estimate $\hat{\mathbf{r}}(0) = [-500; 0; 0]\ m$. However, the robust SMO, the algorithm actually used for navigation purposes, is less afflicted by the chattering phenomenon. In particular, the robust SMO position accuracy

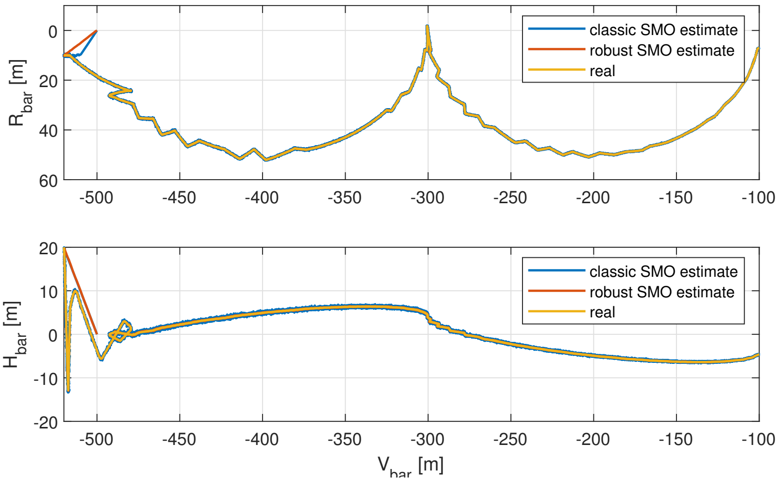

Figure 6.4: Scenario 1, SMC: real and estimated trajectory of the Chaser s/c in the $V_{bar} - R_{bar}$ and $V_{bar} - H_{bar}$ planes.

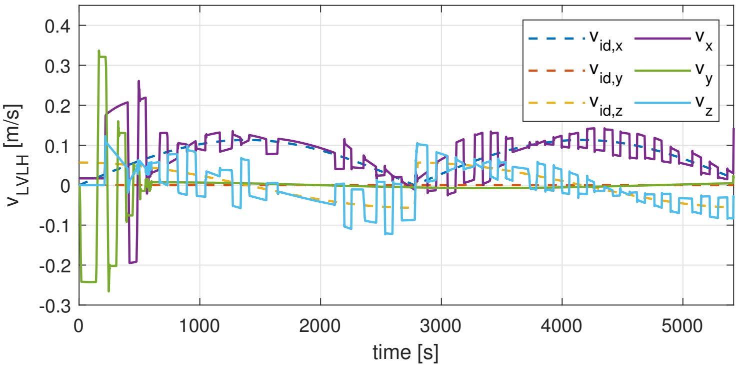

Figure 6.5: Scenario 1, SMC: velocity components of the Chaser s/c in the V_{bar}, H_{bar}, R_{bar} directions.

is $2 \cdot 10^{-1}$ m at $x = -500$ m and, thanks to the increase of accuracy characterising the optical camera measurements, becomes $4 \cdot 10^{-2}$ m at $x = -100$ m. The classic SMO position accuracy is roughly ten times bigger, going from 2 m to $4 * 10^{-1}$ m. Furthermore, the discontinuous control approach adopted creates a *zig zag* trend in the manoeuvre execution, especially in the $V_{bar} - R_{bar}$ plane. As for the H_{bar} direction, no control effort is required roughly after $x = -480$ m since the y-displacement remains minor than 10 m. The discontinuous control approach also causes a *step* trend in the Chaser velocity, as shown in Fig. 6.5, where the actual velocity components are compared to the ideal velocity characterising the radial boosts. Accordingly to Fig. 6.4, no v_y step is noticeable after about 600 s, i.e. absence of control effort in the H_{bar} direction. Fig. 6.6, instead, reports the estimate of v_x provided by both the SMOs. It is clear how, while the classic SMO estimate loses accuracy every time the control system is in action, the robust SMO is able to constantly track the velocity even with half knowledge of the control input as explained in Sec. 6.2.3. The robust SMO error peak noticeable at the start of the simulation is caused by the fact that the data fusion method described in Fig. 6.3 provides the corrected velocity input to the algorithm from $t = 20$ s on. The robust SMO velocity accuracy increases from $2 \cdot 10^{-2}$ m/s at $x = -500$ m to $7 \cdot 10^{-3}$ m/s when $x = -100$ m.

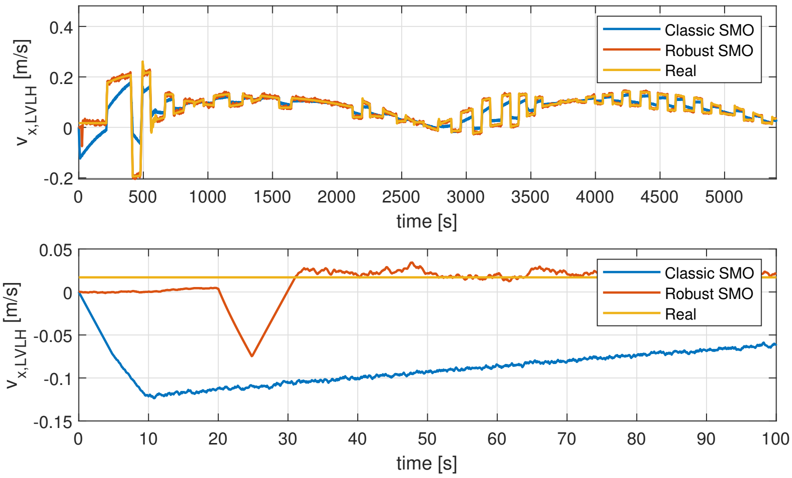

Figure 6.6: Scenario 1, SMC: estimates of the x-component of the Chaser velocity.

The fuel consumption characterising this approach is $m_p = 13.467$ kg.

Afterwards, the same scenario is executed using the combination of HAPF and SMC described in Sec. 6.2.4. Observing the Chaser trajectory in the $V_{bar} - R_{bar}$ and $V_{bar} - H_{bar}$ planes reported in Fig. 6.7 and the velocity evolution over time shown in Fig. 6.8, it can be noted that the results obtained are smoother and more similar to the ideal profiles characterising radial boost manoeuvres. This is caused by the fact that the deactivation of the SMC, this time, is determined by the difference between the desired velocity computed by the HAPF and the actual one, resulting in a more accurate trajectory correction method. Fig. 6.9 shows the x-velocity estimation provided by both the SMOs when the manoeuvre is performed with the combination of HAPF and SMC. Once again it is possible to notice the robust SMO error peak which characterises the first seconds of simulation. This time,

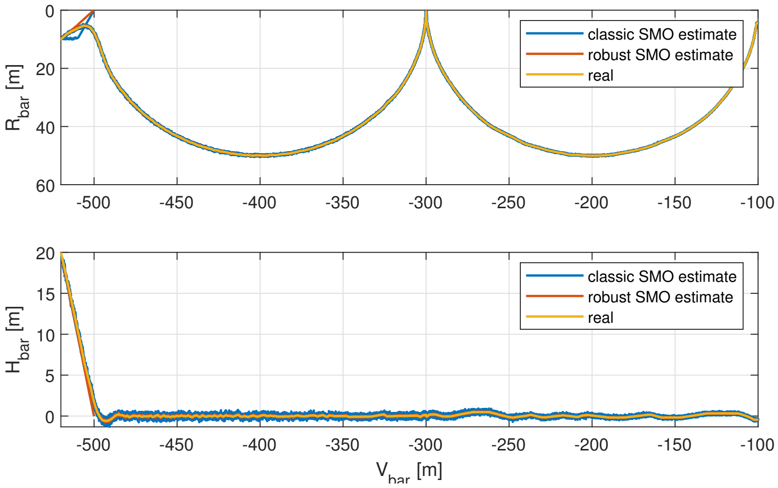

Figure 6.7: Scenario 1, HAPF+SMC: real and estimated trajectory of the Chaser s/c in the $V_{bar} - R_{bar}$ and $V_{bar} - H_{bar}$ planes.

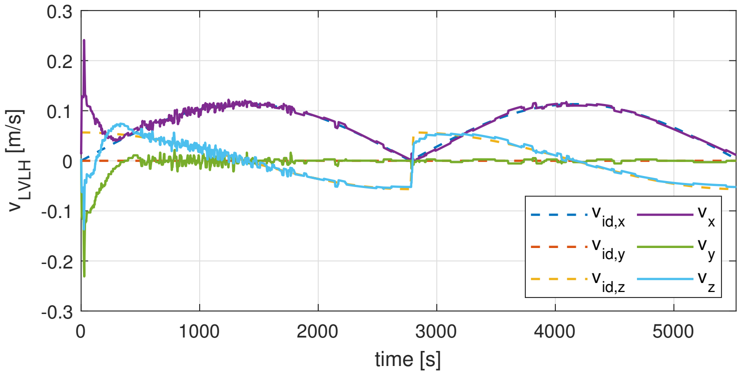

Figure 6.8: Scenario 1, HAPF+SMC: velocity components of the Chaser s/c in the V_{bar}, H_{bar}, R_{bar} directions.

however, the error actually causes a peak in the real v_x, too. This is caused by the erroneous action of HAPF and SMC, temporarily provided with an inaccurate velocity estimate. The loss of accuracy characterising the classic SMO estimates due to the action of the control system, instead, results to be less noticeable in correspondence of slight trajectory corrections, while becomes clearly visible when manoeuvring from the first to the second radial boost. The level of accuracy achieved by the robust SMO are analogous to the ones presented in the previous case.

Even though this approach permits to achieve smoother and more precise results, the fuel consumption estimated is just $m_p = 3.893\ kg$. Propellant saving is actually a consequence of the higher level of accuracy that characterise the combination of HAPF and SMC. In fact, since both the ideal position and velocity are achieved with great precision, the Chaser naturally tends to follow the ideal radial boosts trajectory and requires less pronounced

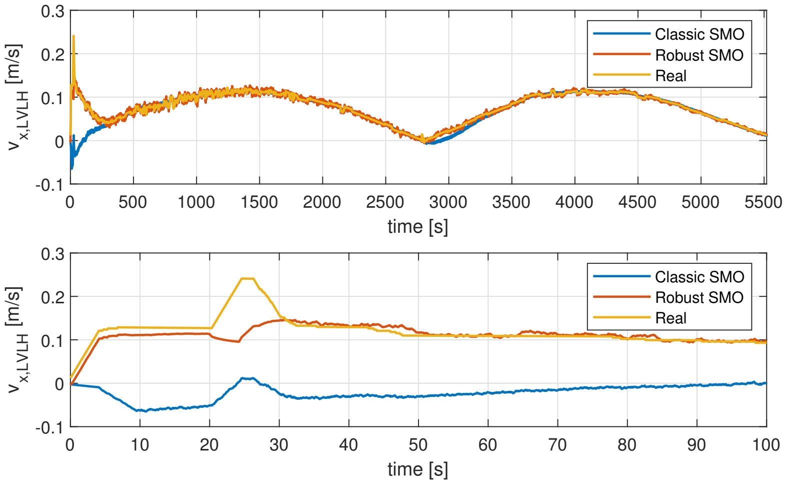

Figure 6.9: Scenario 1, HAPF+SMC: estimates of the x-component of the Chaser velocity.

trajectory corrections.

Scenario 2

In the second scenario, the presence of both mobile and fixed obstacles during the closing phase requires the adoption of obstacle avoidance techniques. Therefore, the approach selected is the combination of HAPF and SMC. Analogously to previous cases, Fig. 6.10 and Fig. 6.11 reports the evolution of the real and estimated Chaser position in the $V_{bar} - R_{bar}$ and $V_{bar} - H_{bar}$ planes and its velocity components profile. In Fig. 6.10, the

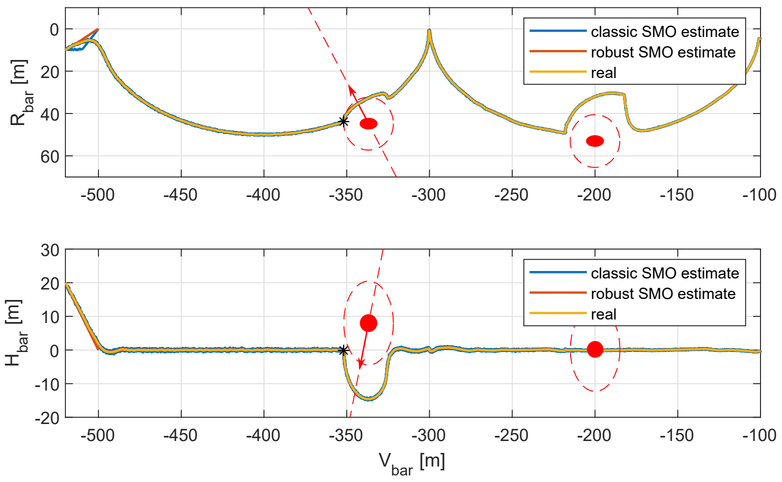

Figure 6.10: Scenario 2, HAPF+SMC: real and estimated trajectory of the Chaser s/c in the $V_{bar} - R_{bar}$ and $V_{bar} - H_{bar}$ planes.

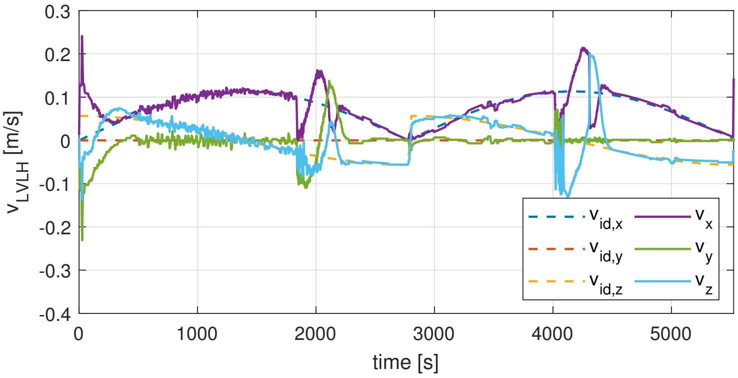

Figure 6.11: Scenario 2, HAPF+SMC: velocity components of the Chaser s/c in the V_{bar}, H_{bar}, R_{bar} directions.

mobile obstacle at the end of the first radial boost and its safety ellipsoid (dashed, $R_s = 10\ m$) represent the obstacle position when the Chaser begins the avoidance manoeuvre (black asterisk). The red dashed line and the red arrow, instead, identify the object motion. It is possible to notice that, since the mobile obstacle is characterised by $v_{obs,y} \neq 0$, the avoidance manoeuvre performed by the Chaser affects its trajectory and velocity both in the $V_{bar} - R_{bar}$ and $V_{bar} - H_{bar}$ planes. The fixed obstacle encountered in the middle of the second radial boost, instead, is avoided manoeuvring just in the $V_{bar} - R_{bar}$ plane, due to the fact that both its centre and the moving goal point of the algorithm are contained in the $V_{bar} - R_{bar}$ plane itself. Although in these 2D graphs it could seem that the obstacle safety ellipsoids are sometimes crossed into, the Chaser actually satisfies the safety requirements,

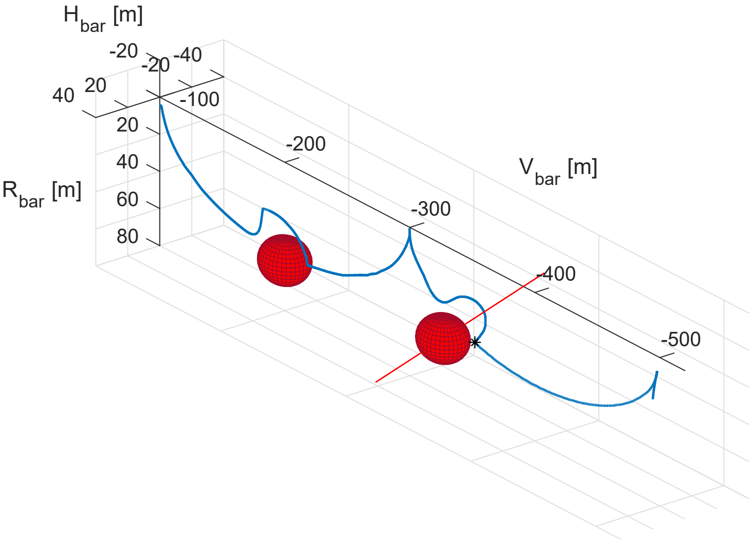

Figure 6.12: Scenario 2, HAPF+SMC: 3D representation of the avoidance manoeuvres with obstacles safety ellipsoids in red.

as clearly visible in the 3D representation of the manoeuvre depicted in Fig. 6.12. As for Navigation performances, the classic SMO is once again not able to accurately estimate the velocity vector under the effect of unknown inputs, losing accuracy especially during the avoidance manoeuvres. Position and velocity accuracy achieved by the robust SMOs, instead, is analogous to the ones obtained in the previous scenario.
The total propellant consumption estimated is $m_p = 14.242\ kg$, which is comparable to the fuel mass consumed in the first case presented in the present section.

6.3.2 Final approach

Since the obstacles configuration characterising the final approach does not differ from one case to the other, only the simulation results of the second scenario will be discussed. All other scenario simulations are characterised by analogous results. In this phase, the Guidance and Control algorithms consist of the combination of HAPF with fixed goal and discontinuous SMC described in Sec. 6.2.4. This approach would lead to a forced straight-line motion towards the Target in absence of obstacles.

Fig. 6.13 reports the real and the estimated trajectory of the Chaser in the $V_{bar} - R_{bar}$ and $V_{bar} - H_{bar}$ planes. The four fixed obstacles characterising the phase are depicted in red and contoured by their dashed safety ellipsoids ($R_s = 5\ s$). The Chaser starts roughly 100 m behind the Target and, due to the symmetrical configuration of the obstacles w.r.t. the $V_{bar} - R_{bar}$ plane, the avoidance manoeuvre is executed mainly inside the plane itself. The position estimates provided by the SMOs are more precise than in the closing phase, thanks to the reduction of the noise corrupting the position measured by optical camera. Robust SMO position estimates are characterised by an accuracy of $8 \cdot 10^{-2}\ m$ at $x = -100\ m$ which increase to $1 \cdot 10^{-2}\ m$ at $x = -4\ m$. Analogously to the previous case, the classic SMO position outputs are roughly ten times less precise. Fig. 6.14, instead, shows the velocity components evolution over time. It can be clearly seen that v_x is immediately

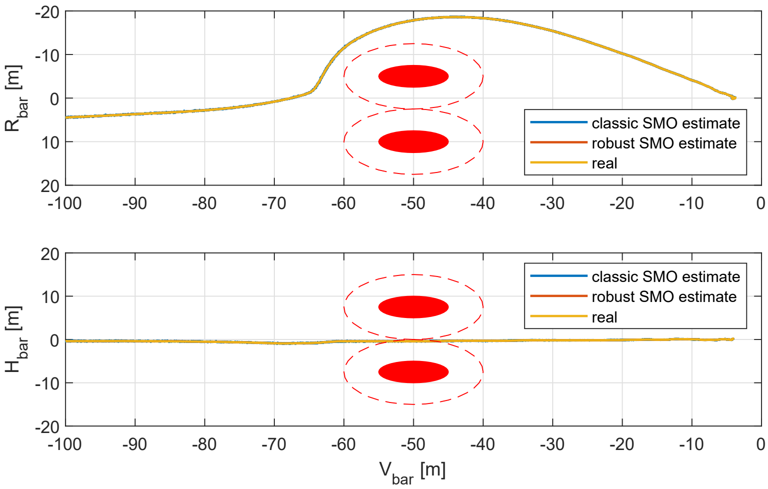

Figure 6.13: Real and estimated trajectory of the Chaser s/c in the $V_{bar} - R_{bar}$ and $V_{bar} - H_{bar}$ planes during the final approach.

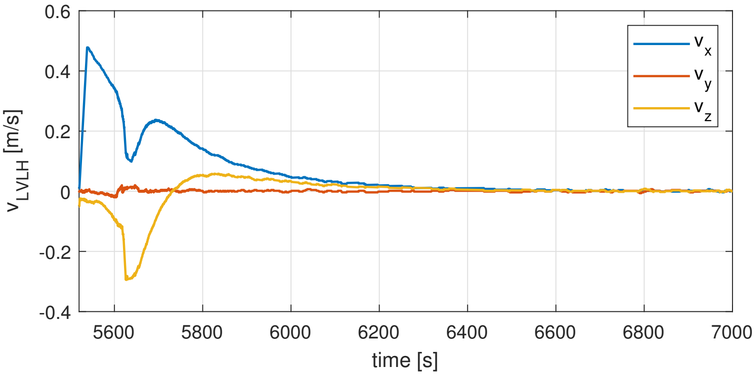

Figure 6.14: Velocity components of the Chaser s/c in the V_{bar}, H_{bar}, R_{bar} directions during the final approach.

modified by the algorithm in order to acquire the value of 0.5 m/s at $x = -100\ m$ and then decreases gradually as the Chaser gets nearer to the goal point $\mathbf{r}_{goal} = [-4; 0; 0]$. When the group of obstacles is encountered, both v_x and v_z variations can be noted, while v_y is kept close to zero. Lastly, Fig. 6.15 reports the x-velocity estimates provided by the SMOs. As expected, the classic SMO is not able to correctly track the velocity under unknown inputs, especially during the avoidance manoeuvre execution. The robust SMO, instead, is characterised by a constant accuracy of $7 \cdot 10^{-3}\ m/s$ throughout the whole approach.

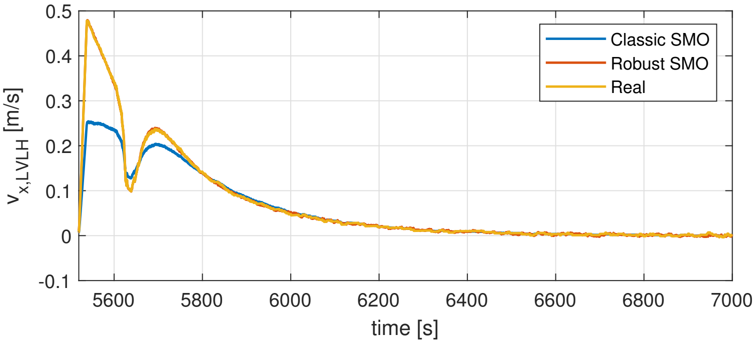

Figure 6.15: Estimates of the x-component of the Chaser velocity during the final approach.

The propellant consumption estimated for this approach manoeuvre is $m_p = 3.344\ kg$.

Lastly, Fig. 6.16 reports the gradient lines of the HAPF characterising the final approach with the obstacles safety ellipsoids depicted in red. It can be noted that the Chaser could have followed different trajectories to overcome the group of obstacles without encountering the local minima problem. The algorithm, therefore, would be able to overcome the local minima criticality even in case of different initial conditions and the fuel consumption would remain comparable to the one characterising the specific manoeuvre showed in the present section.

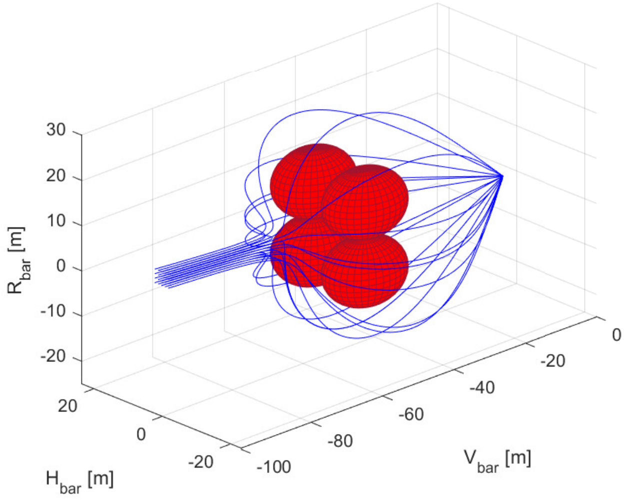

Figure 6.16: Gradient lines of the HAPF characterising the final approach.

6.3.3 Final position station-keeping

In the final position station-keeping, the Chaser must maintain the desired final position while moving the robotic arm to reach the Target. The disturbance forces created by the movimentation of the robotic arm are computed in [27] and reported in Fig. 6.17. Note that these forces are entirely contained inside the $V_{bar} - R_{bar}$ plane, since the robotic arm

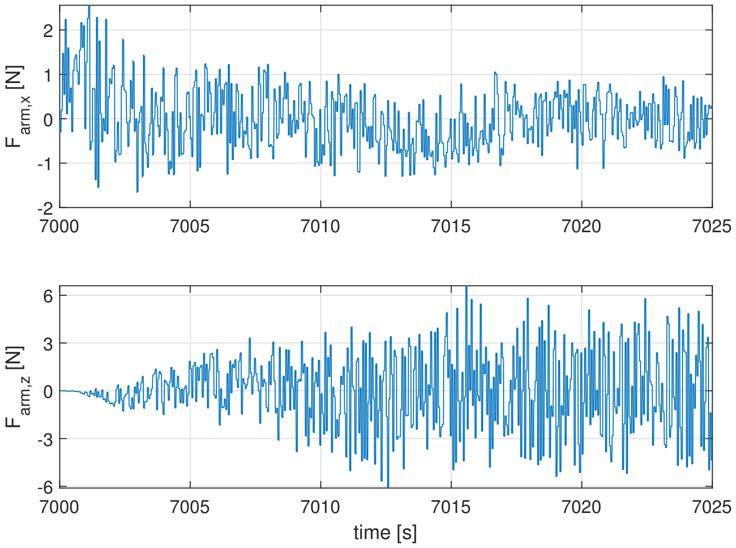

Figure 6.17: Disturbance forces created by the movimentation of the robotic arm in the $V_{bar} - R_{bar}$ plane.

is not manoeuvred in the H_{bar} direction, and last only 25 s. The guidance and control approach is, once again, the combination of HAPF and SMC formulated in Sec. 6.2.4.

Fig. 6.18 and 6.19 depict the relative position and velocity of the Chaser w.r.t. the Target, as well as the state estimates provided by the robust SMO. As for Navigation

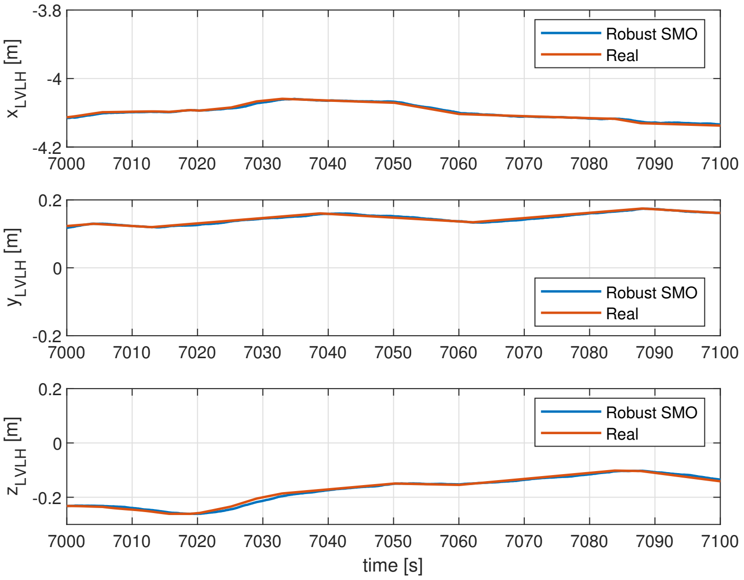

Figure 6.18: Position evolution during the final station-keeping.

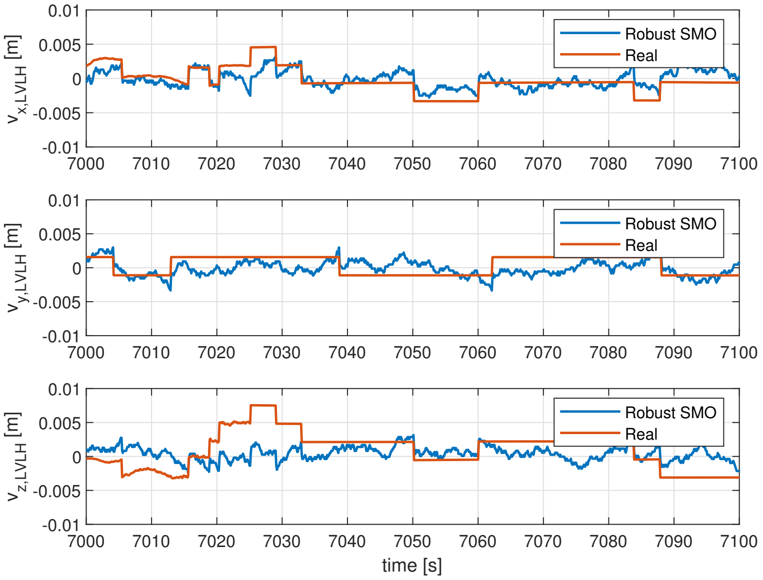

Figure 6.19: Residual velocity during the final station-keeping.

performances, while the position is tracked with precision, the velocity estimates result to be less precise. This is caused by the fact that the real velocity is of the same order of magnitude that characterise the robust SMO velocity accuracy. However, the GNC system is still able to maintain the position with an error of the order of 10^{-1} m and achieve residual velocity of the order of 10^{-3} m/s. The approach selected requires just few grams of propellant to maintain the position (in the specific case reported $m_p = 0.044$ kg).

6.3.4 Fuel consumption considerations

Tab. 6.3 summarises the fuel consumption estimates computed for the closing phase of each approach and scenario considered.

Table 6.3: Closing phase propellant consumption summary.

Scenario	**Closing phase**			
	Algorithm	Fixed obstacles	Mobile obstacles	Fuel consumption
1	SMC	//	//	13.467 kg
1	HAPF+SMC	//	//	3.893 kg
2	HAPF+SMC	one in the second RB ($R_{s,i} = 10$ m)	one in the first RB ($R_{s,i} = 10$ m)	14.242 kg
3	HAPF+SMC	one in the second RB ($R_{s,i} = 20$ m)	one in the first RB ($R_{s,i} = 20$ m)	24.904 kg

It is possible to notice that, even in absence of obstacles, the approach consisting of the HAPF and SMC combination is preferable to the use of the single Sliding-Mode Controller since it results not only in smoother trajectories, but also in lower fuel consumption. As previously explained, propellant saving is a direct consequence of the higher level of precision with which the HAPF+SMC approach achieves both the position and velocity

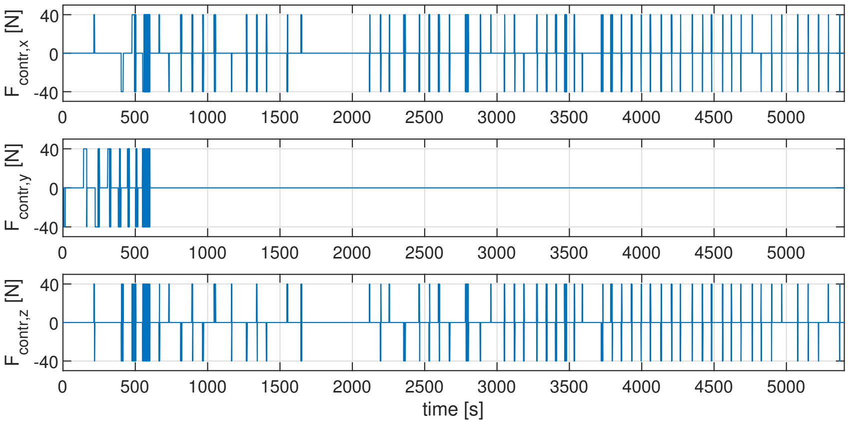

Figure 6.20: Scenario 1, SMC: control forces applied during the closing phase.

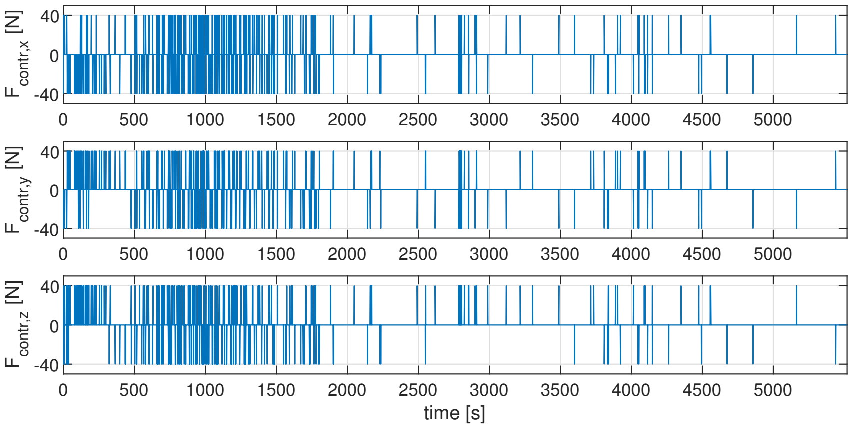

Figure 6.21: Scenario 1, HAPF+SMC: control forces applied during the closing phase.

characterising the ideal radial boost. This is noticeable also in Fig. 6.20 and 6.21, in which the control forces of the two different approach applied to the first scenario are reported. The HAPF+SMC approach is characterised by slight and brief corrections the frequency of which strongly decreases as the trajectory is acquired, roughly after the first half of the first radial boost. The SMC approach, instead, is characterised by stronger and longer corrections which remains frequent throughout the entire closing phase.

The advantage characterising the combination of HAPF and SMC is clearly noticeable in the second scenario, where the algorithm must face the presence of both moving and fixed obstacles. Even though two avoidance manoeuvres are performed during the execution of the radial boosts, in fact, the fuel consumption estimate is comparable to the one computed for the SMC approach in scenario 1. If compared to the case of HAPF+SMC applied to scenario 1, instead, an increase in fuel consumption is obviously observed. As clearly visible from Fig. 6.22, the consumption rise is caused by the increase of control effort required

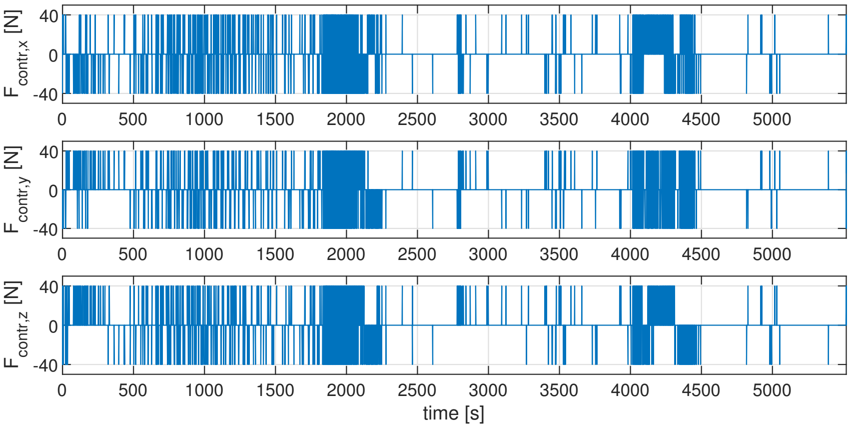

Figure 6.22: Scenario 2, HAPF+SMC: control forces applied during the closing phase.

roughly at $t = 1700\ s$ and $t = 4000\ s$ to avoid the obstacles.

Lastly, in scenario 3, an important rise of fuel consumption is encountered during the closing phase. The increase is caused by the augmentation of the obstacles safety radius $R_{s,i}$, which results in the Chaser performing wider avoidance manoeuvres and requiring higher quantities of propellant. Even in this scenario, however, the total fuel consumption characterising the entire rendezvous and berthing manoeuvre would be minor than 30 kg, i.e. minor than 2% of the Chaser initial mass, as shown in Tab. 6.4.

Table 6.4: Total fuel consumption estimated for the most expensive scenario.

Scenario	**Closing phase**	**Final approach**	**Station-keeping**	**Total fuel consumption**
3	$\approx 25\ kg$	$\approx 3 - 4\ kg$	$< 0.1\ kg$	$< 30\ kg$ ($< 2\%$)

Hence, supposing that the Chaser mass is constant throughout the whole manoeuvre can be considered correct with good approximation.

Chapter 7

Conclusions

The aim of this thesis work was the evaluation and design of Navigation and Guidance algorithms for Rendezvous and Proximity Operations (RPOs), particularly for the closing and final approach phases of a rendezvous and berthing mission. Simulations have been carried out in MATLAB&Simulink environment and, as an example, Fig. 7.1 reports the whole manoeuvre executed by the designed GNC system in the second scenario simulated. Obstacles safety ellipsoids are depicted in red, while the mobile obstacle moving along the red line is reported in the time instant when the Chaser starts performing the avoidance manoeuvre (instant Chaser position represented by the black asterisk).

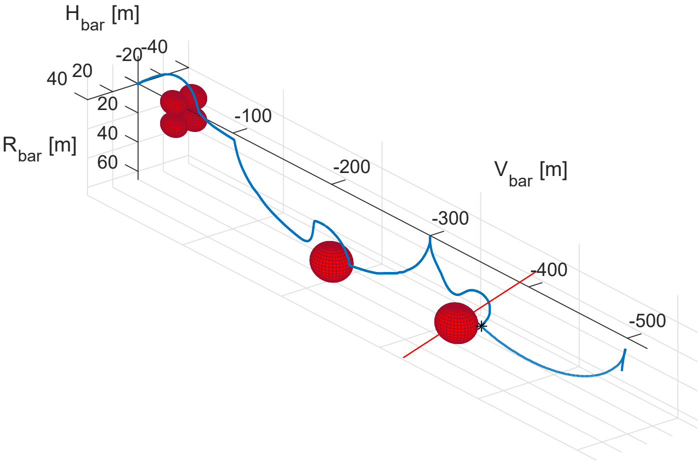

Figure 7.1: Scenario 2: rendezvous manoeuvre executed with the combination of SMO, HAPF and SMC.

Systems dynamics have been modelled through Hill's equations and the Chaser relative acceleration, velocity and position signals w.r.t. the Target have been properly corrupted by the noise characterising the onboard position sensors, an optical camera and an accelerometer. Furthermore, in simulations, not only control forces, but also disturbance forces generated by the movimentation of the robotic arm during the final position station-keeping have been considered as Hill's equations inputs.

The Navigation algorithm designed is a robust first-order Sliding-Mode Observer which, in contrast to Kalman filters, does not require any statistics knowledge of measurement noise. Thanks to its robustness, the designed algorithm has shown better performances than the classic SMO counterpart, being able to correctly track both the Chaser relative position and velocity even when bounded unknown forces are acting on the system. Convergence in finite time, achieved thanks to the Sliding-Mode technique, is also another interesting feature of the algorithm. Lastly, the *data fusion* method designed to correct the accelerometer drift exploiting the position measurement provided by the optical camera and the position estimate formulated by the SMO has proven to be effective. The robust first-order SMO estimate accuracy achieved in the last metres of the approach is $10^{-2}\ m$ on relative position and $7 \cdot 10^{-3}\ m/s$ on relative velocity.

The Guidance and Control approach designed, instead, consists in the combination of Harmonic Artificial Potential Fields (HAPF) and Sliding-Mode Control (SMC). The adoption of harmonic functions has cancelled the local minima problem affecting the classic APF while maintaining the algorithm intuitive and suitable for *online* collision-free path planning. Pre-designed manoeuvres have been safely reproduced thanks to the inclusion of mobile goal points, and both moving and fixed obstacles safety ellipsoids have never been crossed into, even considering the geometrical shape of the Chaser itself. For sake of comparison, an alternative approach consisting of the use of the only SMC has also been adopted to reproduce the rendezvous closing phase. This approach, anyway, has shown worse performances than the combination of HAPF and SMC, which is characterised by smoother results, obstacle avoidance capabilities, online path computation and lower propellant consumption. An increase in fuel consumption estimate has been observed when the safety radius of the obstacles is augmented and the Chaser is forced to manoeuvre far away from the nominal trajectory. The level of station-keeping accuracy obtained with the HAPF+SMC approach during the movimentation of the robotic arm are $3 \cdot 10^{-1}\ m$ on position and $\approx 6 - 7 \cdot 10^{-3}\ m/s$ on velocity.

The accuracy of relative position and velocity control obtained in the final station-keeping, however, is at the limits of berthing operations requirements. This limitation is caused by the estimate accuracy achieved by the designed SMO and data fusion method. Hence, in future works, it would be advisable to deepen the research on sensors models and data fusion methods exploiting SMOs in order to achieve higher accuracy in both the states estimate and control. Furthermore, in the present work, the ellipsoidal shape of the obstacles has been reproduced considering the obstacles as ellipsoidal sets of points. This approach requires an iterative evaluation to identify the point of the obstacle which is closer to the Chaser before computing the repulsive potential field. In order to avoid this iterative approach, which increases the computational cost of the algorithm, future works could deepen the research on diffeomorphic mappings and sphere to ellipsoid transformations. These methods could permit to consider just the centre of mass (CoM) of each obstacle and use the *equilibrium point placement method* to directly create an ellipsoidal zone around the obstacle CoM which is never crossed into by the gradient lines of the artificial potential field.

Appendix A

Simulations results of scenario no. 3

In the present appendix, simulation results relative to scenario 3 are reported. The only difference which is noticeable with respect to the second scenario results is that, since the obstacles safety radius $R_{s,i}$ is increased to 20 m, the avoidance manoeuvres are consequently wider. This means that greater position and velocity modifications, as well as an higher control effort and thus fuel consumption, are observed in obstacles proximity. Fuel consumption estimate for the only closing phase is $m_p = 24.904\ kg$.

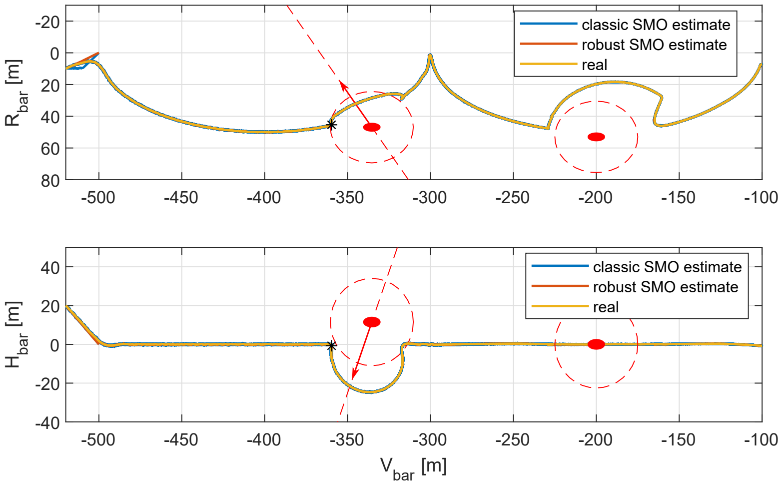

Figure A.1: Scenario 3, HAPF+SMC: real and estimated trajectory of the Chaser s/c in the $V_{bar} - R_{bar}$ and $V_{bar} - H_{bar}$ planes.

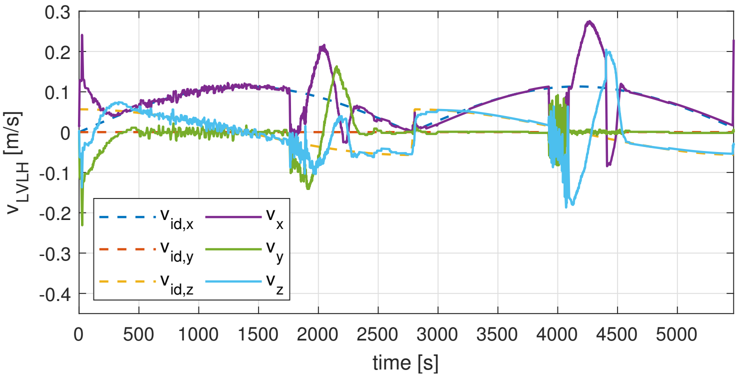

Figure A.2: Scenario 3, HAPF+SMC: velocity components of the Chaser s/c in the V_{bar}, H_{bar}, R_{bar} directions.

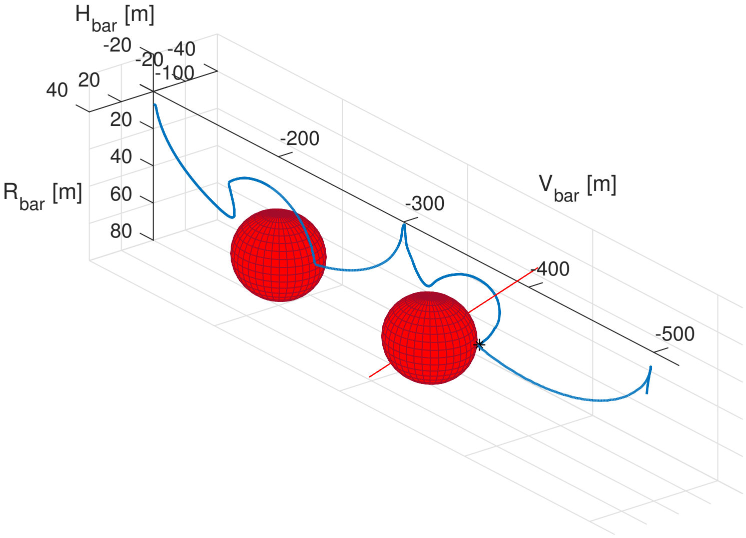

Figure A.3: Scenario 3, HAPF+SMC: 3D representation of the avoidance manoeuvres with obstacles safety ellipsoids in red.

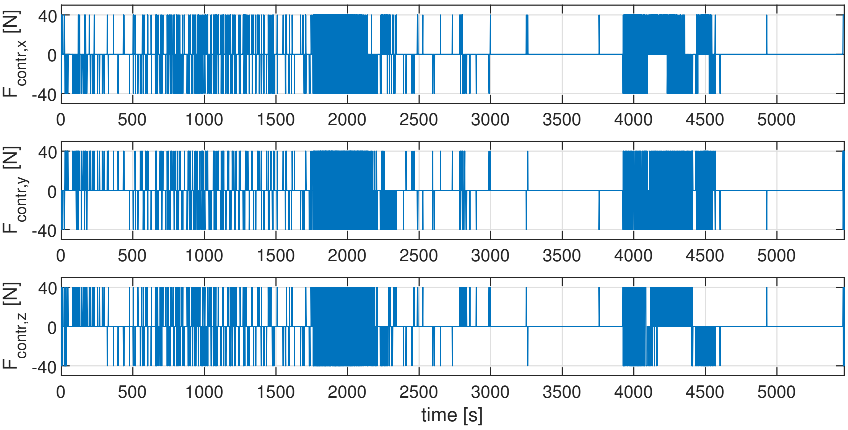

Figure A.4: Scenario 3, HAPF+SMC: control forces applied during the closing phase.

Bibliography

[1] "About - hubble servicing missions," NASA, 2021. [Online]. Available: https://www.nasa.gov/mission_pages/hubble/servicing/index.html

[2] "Darpa cancels formation-flying satellite demo," 2013. [Online]. Available: https://spacenews.com/35375darpa-cancels-formation-flying-satellite-demo/

[3] "Companies demonstrate groundbreaking satellite life-extension service," Northrop Grumman, 2020. [Online]. Available: https://www.northropgrumman.com/space/space-logistics-services/

[4] Deimos Elecnor Group, ClearSpace, 2020. [Online]. Available: https://elecnor-deimos.com/clearspace/

[5] "Space environment statistics," ESA, 2021. [Online]. Available: https://sdup.esoc.esa.int/discosweb/statistics

[6] "Destruction junction—what's your function?" NASA, 2017. [Online]. Available: https://www.nasa.gov/feature/destruction-junction-what-s-your-function/

[7] "Gemini's first docking turns to wild ride in orbit," NASA, 2016. [Online]. Available: https://www.nasa.gov/feature/geminis-first-docking-turns-to-wild-ride-in-orbit

[8] E. Capello, "Dispense del corso di dinamica e controllo di veicoli spaziali," A.A. 2019-2020, at Politecnico di Torino.

[9] W. Fehse, *Automated Rendezvous and Docking of Spacecraft*, ser. Cambridge Aerospace Series. Cambridge University Press, 2003.

[10] Y. Luo, J. Zhang, and G. Tang, "Survey of orbital dynamics and control of space rendezvous," *Chinese Journal of Aeronautics*, vol. 27, p. 1–11, feb 2014.

[11] Y. Zhang, Z. Zhao, T. Lu, L. Yuan, W. Xu, and J. Zhu, "A comparative study of luenberger observer, sliding mode observer and extended kalman filter for sensorless vector control of induction motor drives," in *2009 IEEE Energy Conversion Congress and Exposition*, 2009, pp. 2466–2473.

[12] F. Chen and M. Dunnigan, "Comparative study of a sliding-mode observer and kalman filters for full state estimation in an induction machine," *IEE Proceedings - Electric Power Applications*, vol. 149, no. 1, pp. 53–64, jan 2002.

[13] I. Schkolnikov, Y. Shtessel, P. Zarchan, and D. Lianos, "Sliding mode observers versus kalman filter in the homing loop," in *AIAA/BMDO Technology Conference Proceedings*, jul 2001, p. 8.

[14] A. Ferrara and M. Rubagotti, "Second-order sliding-mode control of a mobile robot based on a harmonic potential field," *Control Theory & Applications, IET*, vol. 2, pp. 807 – 818, oct 2008.

[15] M. Mancini, N. Bloise, E. Capello, and E. Punta, "Sliding mode control techniques

and artificial potential field for dynamic collision avoidance in rendezvous maneuvers," *IEEE Control Systems Letters*, vol. 4, no. 2, pp. 313–318, 2020.

[16] S. Ge and Y. Cui, "Dynamic motion planning for mobile robots using potential field method," *Autonomous Robots*, vol. 13, pp. 207–222, nov 2002.

[17] T. Lacey, "Chapter 11. tutorial: The kalman filter." [Online]. Available: http://web.mit.edu/kirtley/kirtley/binlustuff/literature/control/Kalman%20filter.pdf

[18] M. Daher, "Thesis manuscript," Ph.D. dissertation, Université de Lille, dec 2017.

[19] A. Oppenheim and V. George, *Signals, Systems and Inference.* Pearson, 2015, ch. 6.

[20] Y. Shtessel, C. Edwards, L. Fridman, and A. Levant, *Sliding Mode Control and Observation*, 1st ed., ser. Control Engineering. Birkhäuser Basel, 2015.

[21] M. Hawkins, Y. Guo, and B. Wie, "Spacecraft guidance algorithms for asteroid intercept and rendezvous missions," *International Journal of Aeronautical and Space Sciences*, vol. 13, pp. 154–169, jun 2012.

[22] E. Capello, F. Dabbene, G. Guglieri, and E. Punta, ""flyable" guidance and control algorithms for orbital rendezvous maneuver," *SICE Journal of Control, Measurement, and System Integration*, vol. 11, pp. 14–24, jan 2018.

[23] S. M. Hosseini Rostami, A. Kumar, J. Wang, and X. Liu, "Obstacle avoidance of mobile robots using modified artificial potential field algorithm," *EURASIP Journal on Wireless Communications and Networking*, vol. 2019, mar 2019.

[24] L. Zhou and W. Li, "Adaptive artificial potential field approach for obstacle avoidance path planning," in *2014 Seventh International Symposium on Computational Intelligence and Design*, vol. 2, 2014, pp. 429–432.

[25] J. Kim and P. K. Khosla, "Real-time obstacle avoidance using harmonic potential functions," *IEEE Transactions on Robotics and Automation*, vol. 8, no. 3, pp. 338–349, 1992.

[26] J. Guldner and V. I. Utkin, "Sliding mode control for gradient tracking and robot navigation using artificial potential fields," *IEEE Transactions on Robotics and Automation*, vol. 11, no. 2, pp. 247–254, 1995.

[27] L. Di Ianni, "Control system design with reinforcement learning algorithm for a space manipulator," Master's thesis, Politecnico di Torino, apr 2021.